Terahertz metasurfaces for wideband polarisation control

by

Wendy Suk Ling Lee

B Eng (Electrical and Computer Systems Engineering, Honours),
Monash University, Malaysia, 2014

Thesis submitted for the degree of

Doctor of Philosophy

in

School of Electrical & Electronic Engineering
Faculty of Engineering, Computer & Mathematical Sciences
The University of Adelaide

2018

Supervisors:

Prof. Christophe Fumeaux, School of Electrical & Electronic Engineering

Dr. Withawat Withayachumnankul, School of Electrical & Electronic Engineering

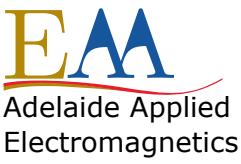

THE UNIVERSITY *of* ADELAIDE

Contents

Abstract

The thesis covers four separated research topics under the umbrella of terahertz metasurfaces comprising of dielectric and metallic resonators. These research topics have stemmed from recent breakthroughs with first dielectric metasurfaces realised only in early 2015. Metallic- and dielectric-resonator metasurfaces have been designed with potential application in the terahertz electromagnetic spectrum, including sensing, imaging and communications. To date, four devices have been successfully designed which were fabricated by our collaborators in RMIT, Melbourne. Due to the advancement of these devices in the micro-scale, we required state-of-the-art fabrication facility in Melbourne.

The thesis layout will be divided into seven chapters. Chapter 1 will present the motivation and overview of the thesis, highlighting my original contributions. Next, Chapter 2 will consist of the background knowledge used for the investigations carried out in this thesis. In particular, conventional methods used to demonstrate polarisation control through birefringence will be detailed, together with their drawbacks. An alternative solution provided by the concept of "metasurfaces", which is capable of creating designable birefringence is then proposed which builds the backbone for all my research.

Chapters 3 through 6 will detail the five terahertz metasurface designs and experiments carried out throughout my candidature. Specifically, Chapter 3 will detail a metasurface design consisting of metallic resonators functioning as a broadband terahertz circular-polarisation beam splitter. To the best of my knowledge, this is the first realisation and experimental demonstration of a structure with this functionality in the terahertz range. The findings of this work have been published in a highly ranked journal, *Advanced Optical Materials*. Here, we employ metallic resonators as engineered birefringent materials to effectively deflect circularly polarised terahertz waves into opposing directions.

In Chapters 4-6, the metasurface designs consist of dielectric resonators. Chapter 4 highlights the work, Terahertz near-field imaging of dielectric resonators. This work was designed in Adelaide and then measured in the University of Freiburg. The findings of this work has also been published in a high ranked journal, *Optics Express*. In this Chapter we examine the two fundamental resonances in dielectric resonators, namely

the electric and magnetic dipole resonance in the near-field. The measured electric fields show the existence of these modes, which are essential towards highly efficient metasurface designs.

The next 2 designs making up Chapters 5 and 6 are "Broadband highly efficient quarter- and half-wave mirrors at terahertz frequencies". The work has been completed, and has been accepted for publication in *Optics Express*. Chapter 5 details dielectric-resonator metasurfaces as quarter-wave mirrors of broadband and highly efficient capabilities.

In Chapter 6, a dielectric-resonator metasurface was fabricated and experimentally validated. Furthermore, metallic- and dielectric-resonator metasurfaces as half-wave mirrors are compared and contrasted. The two metasurface designs which will be presented are functional around the similar operational frequency range. The performance of both metasurfaces is discussed.

Lastly, Chapter 7 will conclude the thesis and present an outlook of terahertz metasurfaces. Ultimately, this work aims to provide sufficient knowledge towards generating even more highly efficient terahertz metasurfaces for future integration with terahertz photonic devices.

Originality Declaration

I certify that this work contains no material which has been accepted for the award of any other degree or diploma in my name, in any university or other tertiary institution and, to the best of my knowledge and belief, contains no material previously published or written by another person, except where due reference has been made in the text. In addition, I certify that no part of this work will, in the future, be used in a submission in my name, for any other degree or diploma in any university or other tertiary institution without the prior approval of the University of Adelaide and where applicable, any partner institution responsible for the joint-award of this degree.

I give consent to this copy of the thesis, when deposited in the University Library, being available for loan, photocopying, and dissemination through the library digital thesis collection, subject to the provisions of the Copyright Act 1968.

I also give permission for the digital version of my thesis to be made available on the web, via the University's digital research repository, the Library Search and also through web search engines, unless permission has been granted by the University to restrict access for a period of time.

Signed

Date

Acknowledgments

First and foremost, I would like to give thanks to God, for giving me the strength, knowledge and ability to embark on and this doctoral journey. Without any of His blessings none of this would have been possible.

I would like to express my deepest gratitude to my supervisors Prof. Christophe Fumeaux and Dr. Withawat Withayachumnankul. Prof. Christophe Fumeaux took me on as a Ph.D candidate even though I have little knowledge of applied electromagnetics back in 2014. Nevertheless, he patiently guided me through my research even when I stumbled on basic concepts. His vast knowledge of antennas and extensive experience proved invaluable in my research. Our weekly meetings were where ideas were inspired and transpired. These meetings motivated me to be more rigorous and thorough in my research. Apart from that, Prof. Fumeaux would painstakingly review my manuscripts and give me critical comments to better my writing. A smiley face hidden behind all the yellow smears is always reassuring that I have improved.

Dr. Withawat Withayachumnankul is my co-supervisor and an outstanding scholar. His extensive knowledge in everything terahertz related and his generosity in sharing that knowledge was vital to my growth as a researcher. Aside from that, his "open door" policy allowed me to ask questions and have discussions at any time. He would often advise me to be more critical in my work, and always encouraged me to go back to the fundamentals whenever I fall short of understanding concepts. Through endless discussions in long meetings, his constructive comments have been a great motivation towards completion of this thesis. I will always remember the times he told me to "take it easy" when times were rough. These little things are what kept me going at times, and I greatly appreciate that.

I would also like to take this opportunity to express my gratitude to the researchers Functional Materials and Microsystems Research and Micro Nano Research Facility of RMIT University. All metasurface designs presented in this thesis were manufactured by them. Thank you Assoc. Prof. Sharath Sriram, Assoc. Prof. Madhu Bhaskaran, Ms. Shruti Nirantar, Mr. Rajour Tanyi Ako and Ms. Mei Xian Low for providing me with these remarkable samples.

During my candidature I received extensive support from past and present members of the Applied Electromagnetics Group at the University of Adelaide, Dr. Ali Karami Horestani, Dr Zahra Shaterian, Dr. Tiaoming Niu, Dr. Fengxue Liu, Dr. Cheng Zhao, Dr. Nicholas Lawrence, Dr. Amir Ebrahimi, Dr. Shengjian (Jammy) Chen, Dr. Nghia Nguyen Trong, Dr. Chengjun Zou, Sree Pinapati, Nailah Zainarry, Andrew Udina, Xiaojing Lv, Xiaolong You, Jack Gao, Jin Huang, Ken Paramayudha and Ali Malakooti. I truly enjoyed our group meetings and comprehensive discussions. I would also like to thank Dr. Daniel Headland for providing insight and suggestions which aided my research. In addition, I also acknowledge the staff of the school, IT officers, workshop colleagues for all their assistance throughout my candidature, namely Assoc. Prof. Wen Soong, Prof. Cheng-Chew Lim, Mr. Henry Ho, Ms. Franca Guest, Mr. Danny Di Giacomo, Mr. David Bowler, Mr. Mark Innes and Ms. Jodie Schluter. I am eternally grateful for the friends that I have made at this university, who in one way or another supported me throughout this journey, Dr. Hong Gunn Chew, Mr. Vichet Duk, Mr. Peng Wang, Ms. Yik Ling Lim, Mrs. Akram Najafzadeh, Mr. Xin Yuan.

I am also thankful for the financial assistance given by the School of Electrical and Electronic Engineering, which allowed me to attend international conferences to present my work and to learn from the great minds of the field. I would also like to acknowledge my father for providing the finances to complete this program and The University of Adelaide for providing me with the Completion Scholarship. A special note of appreciation goes to the anonymous donor who provided the funds for my travels to Freiburg, Germany to conduct the near-field imaging experiment.

I was warmly welcomed into the Adelaide Metro Church of Christ by Andy and Jude Ezis, who never failed to ask me how I was, week after week. I thank God for allowing me to be integrated into this loving church. Thank you everyone from Adelaide Metro Church of Christ, for your hospitality. I would like to specifically mention my best friend in church, Ann Wu, who tirelessly invited me out to meals despite my hectic research life. Thank you for your patience and friendship, I really appreciate it.

To my cyber-family, I appreciate all of you for providing the much-needed stress relief through endless nights of adventures and adrenalin pumping battles in cyberspace. Though there are many people to thank, here are some special mentions — Vincent Yu, Derek Caske, Andrew Jones, Bradley Nash, Damian Worsnop, Yirun Wong, Vanessa Ng, Michael Hong, Lewis Omond. A greater appreciation goes to Dr. Wei Zhuo, who took the time to discuss my research and gave me helpful advice.

To my best friend, Natasha Tan, I appreciate the time and effort that you took to help me get through the ups and downs of life. I sincerely thank you for your patience and understanding, and I will treasure our friendship forever.

Last but not least, my heartfelt gratitude goes to my mother, whose love and encouragement supported me in all my pursuits. Her undying love nurtured me to who I am today, and she is indeed the best mother anyone can ask for. Thank you for everything that you have given me, without which I will not be where I am today.

Thesis Conventions

The following conventions have been adopted in this Thesis:

Typesetting

This document was compiled using LaTeX2e. Texmaker 5.0.2 was used as text editor interfaced to LaTeX2e. Inkscape 0.92.2 was used to produce schematic diagrams and other drawings.

Spelling

Australian English spelling conventions have been used, as defined in the Macquarie English Dictionary (A. Delbridge (Ed.), Macquarie Library, North Ryde, NSW, Australia, 2001).

Referencing

The Harvard style is used for referencing and citation in this thesis.

System of Units

The units comply with the international system of units recommended in an Australian Standard: AS ISO 1000-1998 (Standards Australia Committee ME/71, Quantities, Units and Conversions 1998).

Publications

Journals

LEE-W. S. L., AKO-R. T., LOW-M. X., BHASKARAN-M., SRIRAM-S., FUMEAUX-C., AND WITHAYACHUMNANKUL-W. (2018). Dielectric-resonator metasurfaces for broadband terahertz quarter- and half-wave mirrors, *Optics Express*, **26**(11), *Accepted for Publication*.

LEE-W. S. L., NIRANTAR-S., HEADLAND-D., BHASKARAN-M., SRIRAM-S., FUMEAUX-C., AND WITHAYACHUMNANKUL-W. (2018). Broadband terahertz circular-polarization beam splitters, *Advanced Optical Materials*, **6**(3), art. no. 1870010.

LEE-W. S. L., KALTENECKER-K., NIRANTAR-S., WITHAYACHUMNANKUL W., WALTHER-M., BHASKARAN-M., FISCHER-B. M., SRIRAM-S. AND FUMEAUX-C. (2016). Terahertz near-field imaging of dielectric resonators, *Optics Express*, **25**(4), pp. 3756-3764.

Conferences

LEE-W. S. L., BHASKARAN-M., SRIRAM-S., FUMEAUX-C. AND WITHAYACHUMNANKUL-W. (2018). Metallic and dielectric resonators in broadband half-wave mirrors for terahertz frequencies, *3rd Australian Microwave Symposium*, Brisbane, Australia.

LEE-W. S. L., KALTENECKER-K., NIRANTAR-S., WITHAYACHUMNANKUL W., WALTHER-M., BHASKARAN-M., FISCHER-B. M., SRIRAM-S. AND FUMEAUX-C. (2016). Near-field imaging of magnetic resonance in terahertz dielectric resonator antennas, *41st International Conference on Infrared, Millimeter, and Terahertz Waves*, Copenhagen, Denmark.

List of Figures

Chapter 1

Introduction

THE terahertz region is located between the microwave and infrared ranges of the electromagnetic spectrum. This region is under-utilised despite having potential for a myriad of applications in imaging, sensing and communications. Efficient polarisation control at terahertz frequencies would diversify the capabilities of these applications. Conventional methods used for terahertz polarisation conversion have several limitations. This introductory chapter starts with a brief definition of the terahertz range accompanied with relevant background knowledge on terahertz technologies and more specifically components related to polarisation control. An alternative approach to polarisation conversion is then discussed, which provides the motivation behind this research. Lastly, the structure of this thesis is included in this Chapter.

1.1 Terahertz technology

Terahertz radiation refers to electromagnetic waves in the frequency range from 0.1 to 10 THz, as shown in Fig. 1.1. From a broad view, the terahertz range is in between the microwave and infrared ranges of the electromagnetic spectrum, with some overlap on the lower (microwave) and higher (infrared) frequency sides. At the lower end of the frequency range, there is some overlap with the millimetre-wave (MMW) range between 30 GHz and 300 GHz. The terahertz region also covers the whole range of the sub-millimetre wave (sub-MMW) region, from 300 GHz to 3 THz (Wiltse, 1984). At the higher frequency range, the terahertz region overlaps with the far infrared region, whose range is defined as 3 to 20 THz (Vatansever and Hamblin, 2012).

The terahertz region is well-known for being one of the underutilised portions of the electromagnetic spectrum. The reason behind its underutilisation can be attributed to the lack of development of technologies for generating and detecting terahertz waves. Thus, the terahertz range is often referred to as the "terahertz gap". The development of sources that can excite terahertz radiation has become a prominent topic of research. Currently, photoconductive antennas (Matsuura *et al.*, 1997; Dreyhaupt *et al.*, 2005), organic crystals (Brunner *et al.*, 2008) and non-organic crystals (Zhang *et al.*, 1992) together with ultrafast lasers are used to generate broadband terahertz radiation. These technologies allow the progress of terahertz time-domain spectroscopy (THz-TDS) which can effectively generate and detect terahertz radiation. The advancement of

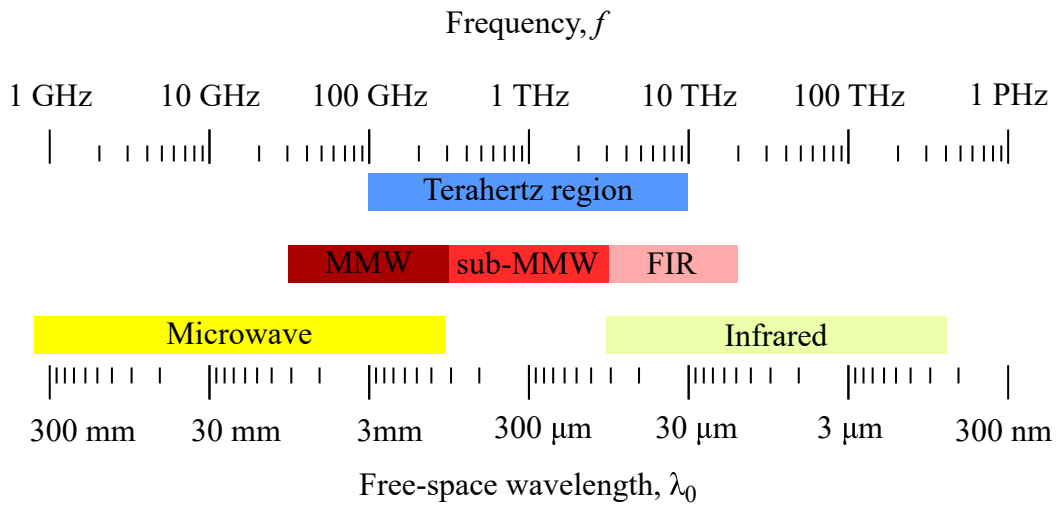

Figure 1.1. Electromagnetic spectrum. The terahertz frequency regime within the electromagnetic spectrum is shown here with its overlap with the microwave and infrared regions.

spectroscopy techniques are essential towards practical applications in the terahertz region.

One of the main uses of terahertz spectroscopy is material characterisation (Naftaly and Miles, 2007; Ferguson and Zhang, 2002). This is because many substances exhibit molecular resonance at terahertz frequencies. Furthermore, the absorption coefficient and the refractive index of materials can be directly linked to the amplitude and phase respectively of the transmitted terahertz electric field as both parts of the complex refractive index are obtainable by THz-TDS. This is because transmitted terahertz electric field is measured coherently, giving a direct measurement of amplitude and phase. A previously known technique to categorise materials is known as far-infrared Fourier transform spectroscopy (FTS). However, calculations to determine the refractive index from data obtained from FTS can be inaccurate (Naftaly and Miles, 2007). Apart from that, terahertz radiation has been shown to be capable of imaging samples that are opaque at visible and near-infrared frequencies (Moriwaki *et al.*, 2017; Kanda *et al.*, 2017; Suzuki *et al.*, 2016a). Terahertz waves are non-ionising as they have low photon energies. This aforementioned property is non-damaging to body tissue, which makes terahertz waves suitable for medical imaging. Consequently, terahertz radiation has been utilised to characterise materials in many areas including chemistry (Balakrishnan *et al.*, 2009; Fischer *et al.*, 2005a), medicine (Reid *et al.*, 2013; Fischer *et al.*, 2005b) and biology (George and Markelz, 2012; Walther *et al.*, 2002).

Presently, there is an increasing demand for wireless systems as they are integrated into our everyday lives. Spectral resources for wireless communications are limited as the main carrier frequency for wireless links at millimetre waves is around 60 GHz which provides data rates around 1.5 Gbps (Nagatsuma *et al.*, 2013). Thus, researchers have focused on the terahertz gap, as high carrier frequencies would lead to ultrafast data rates (Kleine-Ostmann and Nagatsuma, 2011). Furthermore, terahertz devices for wireless communications can also support broadband communication networks (Bird *et al.*, 2008; Jacob *et al.*, 2009; Koenig *et al.*, 2013; Kleine-Ostmann and Nagatsuma, 2011). However, a wide range of optical components, which include filters and modulators, are required to control the terahertz carrier for practical applications.

One of the challenges for applications at terahertz frequencies is efficiency. Terahertz waves suffer from strong attenuation as they propagate through the atmosphere due to high water-vapour absorption. Based on a study by Withayachumnankul *et al.* (2008), it is shown that, as the terahertz pulse travels through a water-vapour filled atmosphere,

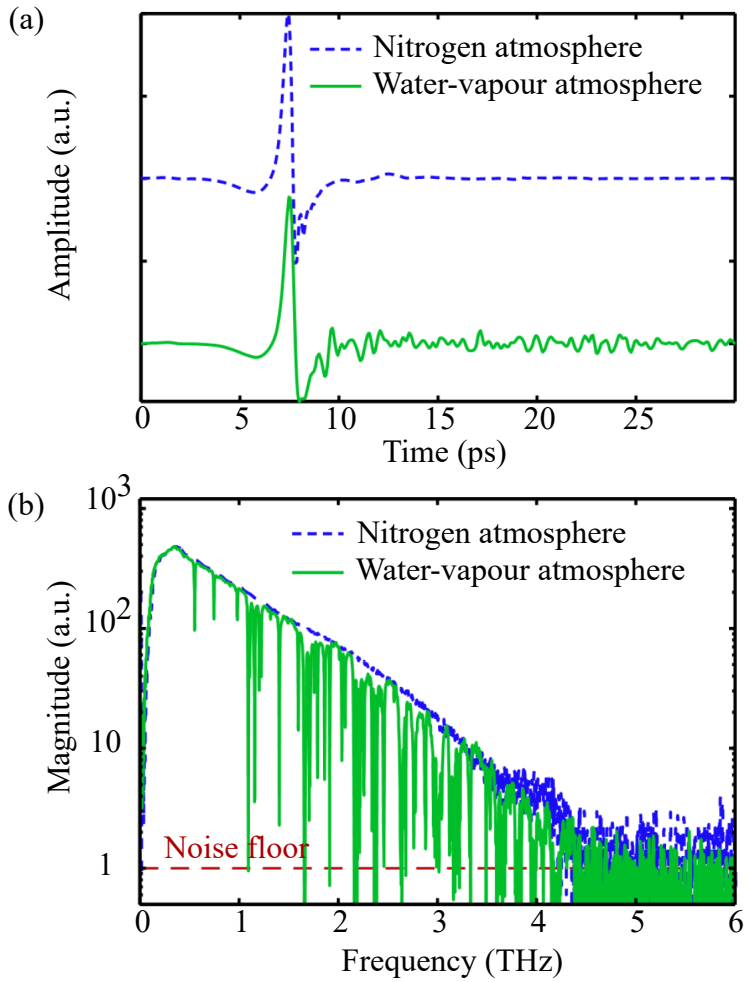

Figure 1.2. Terahertz pulse and the corresponding spectra in different atmospheres. (a) Terahertz pulses recorded in a dry, nitrogen atmosphere as indicated by the blue dashed line and water-vapour atmosphere as indicated by a solid green line. The spectra of these terahertz pulses are shown in (b). Adopted from Withayachumnankul *et al.* (2008).

it undergoes strong fluctuation as shown in Fig. 1.2(a). This fluctuation can be attributed to the energy that is re-radiated by the rotational transitions of water molecules. With the corresponding spectra shown in Fig. 1.2(b), it is observed that the water-vapour absorption limits terahertz radiation to some spectral windows. As such, for devices in communications, the limitation in transmission distance makes terahertz radiation more suitable for indoor applications.

Polarisation control is also essential for applications at terahertz frequencies. For material characterisation, molecules such as DNA are chiral and responds differently to left- or right-handed circularly polarised waves (Ferguson and Zhang, 2002). From a wireless communications point of view, the ability to increase channel capacity through

polarisation-division multiplexing would beneficial. Thus, it is crucial to generate highly efficient terahertz waves of different polarisations. For instance, circularly polarised waves are favourable in communications. This can only be achieved through efficient polarisation conversion.

1.2 Motivation

Conventional methods to achieve polarisation conversion rely on bulky optical components such as waveplates. The waveplates that are commercially available are usually made of crystalline dielectric material. Figure 1.3 shows some examples of waveplates that are commercially available for use at terahertz frequencies. Polarisation conversion is achieved through exploiting the strong anisotropy of these materials. More specifically, as the terahertz wave propagates through such a material, the orthogonal electric field components will experience different refractive indices, depending on their alignment to the optical axis of the material. Consequently, this leads to a distinctive phase delay experienced by each orthogonal field component.

The thickness of the dielectric material depends on the required phase difference for a particular application. The amount of relative phase, Φ, that is imparted onto the two orthogonal electric field components can be calculated by the equation:

$$\Phi = \frac{2\pi\Delta nT}{\lambda_0}, \tag{1.1}$$

(a) (b)

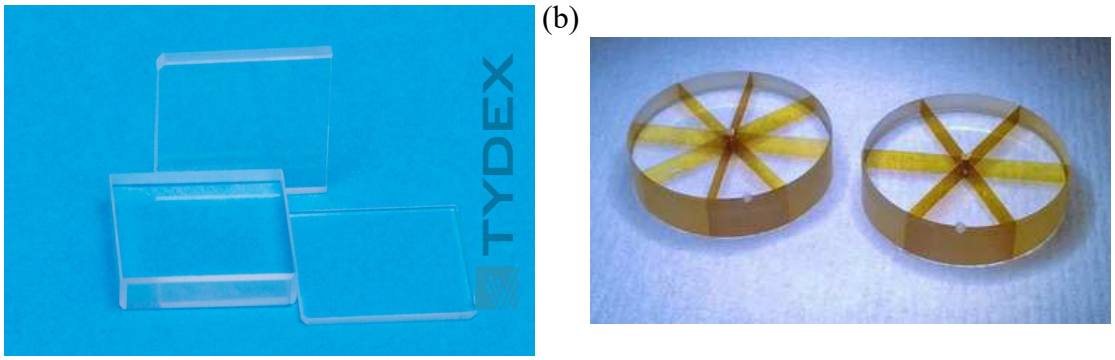

Figure 1.3. Terahertz waveplates. Commercially available terahertz wave plates shown in (a) which are functional at discrete wavelengths. Segmented half-wave plates (b) that converts linearly polarised waves into radially or azimuthally polarised waves. These wave plates in (a) and (b) can be manufactured from Tydex.

where Δn is the difference in refractive index experienced by each orthogonal component, T is the thickness of the dielectric material and λ_0 is the free-space wavelength. In order to increase this phase difference between the field components, the material thickness has to be increased, as shown by Eq. 1.1.

There are several limitations to the use of natural materials (crystalline or not) in wave plates. As shown in Eq. 1.1, the required phase imparted onto the two orthogonal electric field components can be satisfied at discrete wavelengths. This leads to discrete operational frequencies in crystalline wave plates. Besides that, crystalline dielectric materials are of high cost. Furthermore, most of these crystalline materials are bulky. Based on Eq. 1.1, the thickness of a quarter-wave plate made of quartz operating at 1 THz would be at least 8 mm. This is approximately 2600 times the operating wavelength.

Apart from crystalline materials, there are a few naturally available materials that exhibit birefringence at terahertz frequencies. Some examples are paper (Scherger *et al.*, 2011) and wood (Reid and Fedosejevs, 2006). As an illustration, a quarter-wave plate constructed from paper is shown in Fig. 1.4. Additionally, these natural materials also exhibit weak birefringence. Furthermore, paper and wood are less reliable and controllable than crystalline dielectric materials.

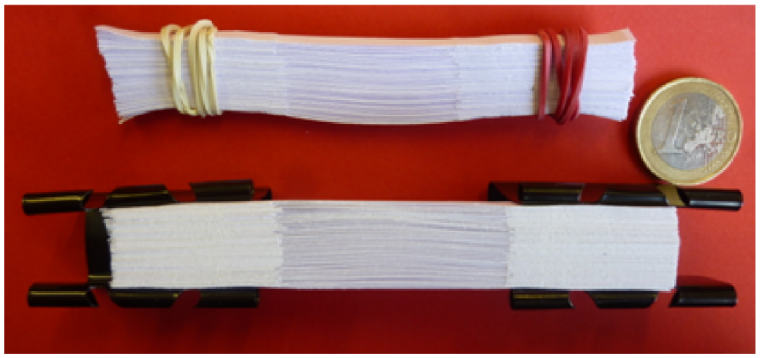

Figure 1.4. Paper terahertz quarter-wave plate. Photograph of the birefringent quarter-wave plate fabricated from paper. Adopted from Scherger *et al.* (2011)

The challenge that presents itself is—how can one design a material that exhibits strong, designable birefringence that overcomes most, if not all limitations set by natural materials? One of the alternatives towards providing designed birefringence at terahertz frequencies is to utilise two-dimensional metamaterials. Metamaterials are essentially specially engineered materials to exhibit a property not commonly found in nature. Their two-dimensional variant, metasurfaces, control the electromagnetic waves in a unique manner, which opens doors for advanced applications. This feature is in contrast to metamaterials, which rely on modifying the constitutive parameters of a material. Initially, metasurfaces were utilised as a prototype to demonstrate complicated three-dimensional metamaterials. However, three-dimensional metamaterials entail very challenging issues such as fabrication complexity. Metasurfaces on the other hand, are planar and can be easily fabricated with existing standard lithography techniques. Sub-wavelength resonators that altogether yield controllable amplitude and phase responses make up these metasurfaces. For birefringent metasurfaces, the resonator geometry is tailored to exhibit a different phase response for each orthogonal polarisation of terahertz waves. For birefringent metasurfaces, the resonator geometry is tailored to exhibit a different phase response for each orthogonal polarisation of terahertz waves. With these features, metasurfaces provide a new perspective towards controlling properties of electromagnetic waves, including phase, amplitude and polarisation. It is worth mentioning that metasurfaces cannot wholly replace devices that would benefit from three-dimensional metamaterials.

Most metasurfaces consist of metallic resonators. An image of a fabricated terahertz metallic-metasurface is shown in Fig. 1.5(a). This metasurface operates in reflection, and consists of metallic patches that shape the outgoing wave by inducing local phase shifts to the incident wave. As such, the resonators can collectively scatter the incident wave into a particular direction as shown in Fig. 1.5(b). As metasurfaces are mostly planar, this overcomes the bulk size of conventional optical components. However, this particular design is only functional at a single wavelength. For practical applications, it is eminently desirable that metasurfaces have a large bandwidth and high efficiency. To overcome this limitation in bandwidth, metasurfaces with metallic resonators have progressed to multilayer structures, where dielectric spacers accompanied with resonating elements are combined to form additional layers. Thus, the broadband capabilities of metasurfaces would overcome the discrete operational frequencies set by conventional optics. Metallic-resonator metasurfaces however, suffer from Ohmic loss with increasing frequencies, which reduces overall efficiency.

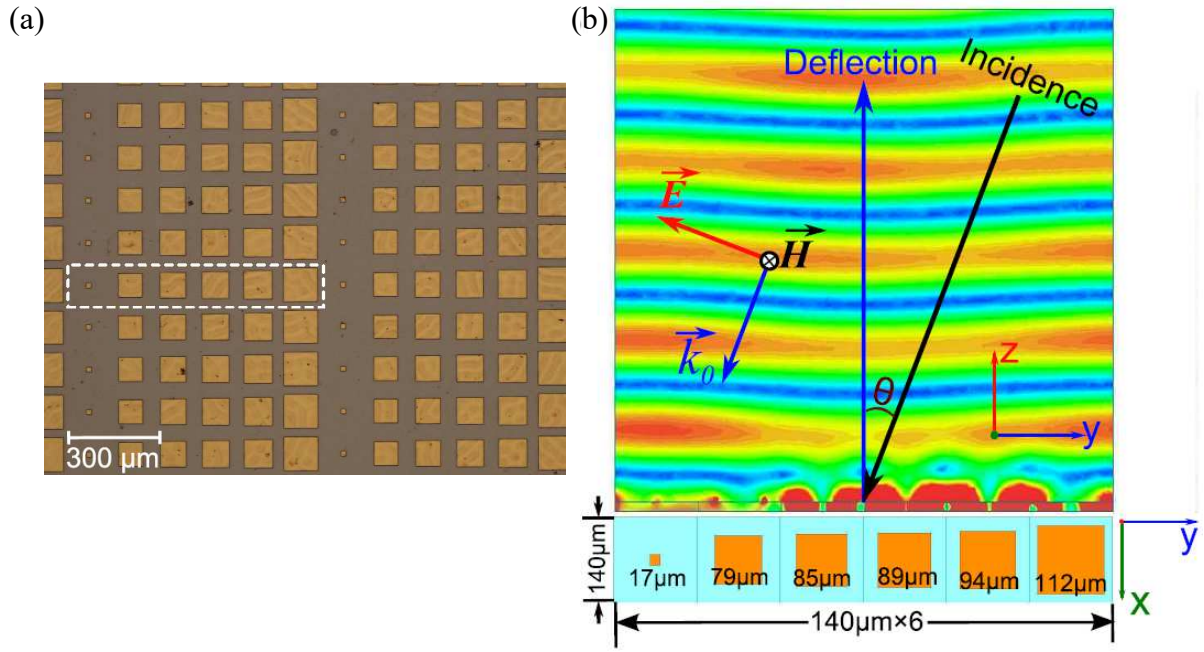

Figure 1.5. Metallic-resonator based metasurface. (a) Scanning electron micrograph of the metallic-resonator metasurface. One subarray is highlighted in white. (b) Simulated scattered field plots for each resonator in the subarray as indicated. Adopted from Niu *et al.* (2013).

One of the methods to boost efficiencies with increasing frequencies is to utilise low-loss dielectric resonators. As dielectric resonators operate via oscillations of displacement current, this alleviates the Ohmic loss that metallic resonators suffer from. One of the earlier terahertz dielectric resonators was realised by Headland *et al.* (2015a). This work provided two key factors that are fundamental to the work in this thesis. Firstly, an unconventional microfabrication procedure was developed to bond a relatively thick, single piece of intrinsic silicon onto a metal film. With this method, experimental realisations of dielectric-resonator metasurfaces was made possible. Figure 1.6(a) shows the unconventional approach in fabrication used to realise a terahertz dielectric-resonator array, with a layered view of the completed structure shown in Fig. 1.6(b). It is noteworthy that a table-top laminator was used to bond the high-resistivity silicon to the SU-8 and gold-coated substrate as shown in step (iv) of Fig. 1.6(b). Secondly, the fabricated design of Headland *et al.* (2015a) exhibits a magnetic dipole resonance within a single layer, which addresses the issue posed by single layer metallic-resonator metasurfaces. With the presence of the magnetic dipole resonance in a single-layered, highly efficient planar metasurfaces with larger phase coverage can be created.

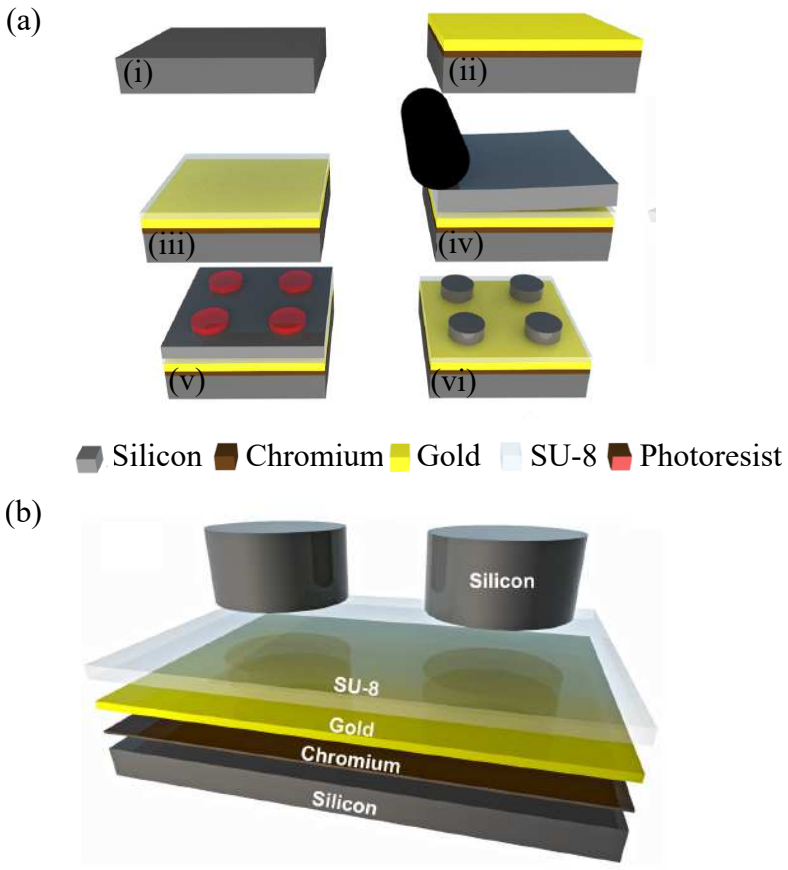

Figure 1.6. Fabrication of the terahertz dielectric resonator. (a) The fabrication process steps of the terahertz dielectric-resonator metasurface as indicated by (i-vi). The complete layered structure is shown in (b). Adopted from Headland *et al.* (2015a).

In a nutshell, metasurfaces for polarisation control that are to be integrated into practical applications in the terahertz regime require several features. It is essential that metasurfaces are highly efficient. This feature is crucial as transmitted and received signals degrade in the atmosphere, so any further reduction in power has to be avoided if possible. Moreover, polarisation conversion has to be effective for ideal functionality. Apart from that, integration into terahertz photonic devices requires metasurfaces to be planar. Lastly, polarisation control should be maintained over a large bandwidth, which is key for many applications. Ultimately, metasurfaces opens new perspectives towards engineering highly efficient polarisation control terahertz devices with various applications in imaging, sensing and communications. Thus, these research areas should be thoroughly explored.

1.3 Thesis outline

This thesis is divided into four parts, each containing about one to three chapters leading to seven chapters in total. The thesis structure is shown in Fig. 1.7.

Part 1: Background The first two chapters present the motivation and the relevant background knowledge for this thesis. Chapter 1 has explained the motivation behind designing metasurfaces for polarisation control in the terahertz range. Chapter 2 then details a thorough literature review of previous metasurface designs in the field with a discussion on advantages and drawbacks. Additionally, background knowledge regarding the concept of wavefront control is briefly discussed in this chapter. Specifically, a wide range of metasurfaces used for polarisation control is highlighted, with an emphasis on their performance and limitations.

Part II - Metallic resonators This part shows the functionalities of a half-wave mirror. Through calculated rotations of metallic resonators, the outgoing wave can be tailored accordingly. In Chapter 3, a metasurface that can effectively reflect incident circularly polarised waves into opposing directions, depending on their handedness is discussed.

Part III - Dielectric resonators This part aims to showcase terahertz metasurfaces consisting of dielectric resonators. Chapter 4 investigates a dielectric-resonator array via a near-field microscope to examine the fundamental resonances required for highly efficient metasurface designs. Next, Chapter 5 details a unique resonator geometry that is used to convert linearly polarised waves into circularly polarised waves. Lastly, Chapter 6 shows a dielectric-resonator metasurfaces as a highly efficient broadband half-wave mirror.

1.4 Summary of original contribution

This thesis involves several original contributions in the field of terahertz metasurfaces as declared in this section. These contributions provide superior alternatives compared to existing methods.

Chapter 3 presents a broadband terahertz circular-polarisation beam splitter. Based on Jones matrices, it can be shown that by gradually rotating elements with a half-wave

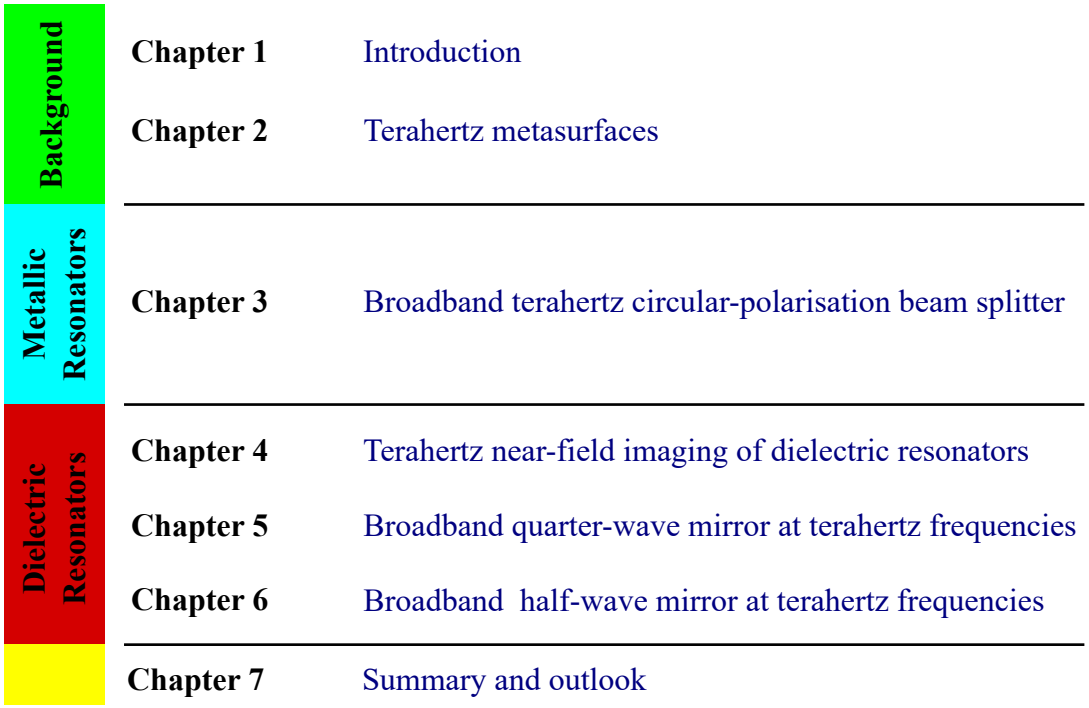

Figure 1.7. Thesis outline. The chapters are divided into 4 major parts as background, metallic resonators, dielectric resonators and conclusion.

response, a ramp phase shift can be imparted on the reflected circularly polarised wave. Mathematically, right- and left-handed circularly polarised waves experience different phase signs, which allow the metasurface to scatter them into different directions. To the best of our knowledge, there has been no handedness-distinguishing beam splitter at terahertz frequencies. This design would be an asset in terahertz communications, particularly for wireless-channel multiplexing. The conceptualisation, design, simulation and experiment were completed at the University of Adelaide. The structure itself was fabricated by our collaborators at the Functional Materials and Microsystem Research and Micro Nano Research Facility (FMM) at RMIT University, Melbourne. The content of this Chapter is published in Lee *et al.* (2018b).

Chapter 4 presents a study into the near-fields of the fundamental resonances required to realise highly efficient dielectric-resonator metasurfaces. As resonant electric fields in dielectric resonators are mostly confined within the dielectric resonator, these fields are not readily accessible with the near-field probe. As such, we aim to observe unique electromagnetic interactions between neighbouring dielectric resonators with a near-field microscope. This dielectric-resonator metasurface was fabricated by our collaborators at the FMM. Design and simulation were performed at the University of Adelaide. The

sample was characterised at the University of Freiburg (during a research visit of the author of this thesis) using their near-field terahertz microscope. The array itself is designed to exhibit the two fundamental resonances, namely electric dipole and magnetic dipole resonances at separated frequencies. Studying the near-fields of dielectric resonators provides the fundamental knowledge towards dielectric-resonator based metasurface design. The content of this Chapter has been published in Lee *et al.* (2017).

Subsequently, Chapter 5 presents a unique wideband quarter-wave mirror consisting of dielectric resonators. This design shows that metasurfaces can overcome the limitations of natural materials at the terahertz frequencies to create strong, engineered birefringence needed for polarisation conversion. By utilising multiple magnetic dipole resonances to support the required phase shift across a large bandwidth, a highly efficient, broadband quarter-wave mirror is realised. Similar to previous structures, this quarter-wave mirror was also fabricated at the FMM, but the design, analysis and experimental validation was performed at the University of Adelaide. To the best of our knowledge, this is the first experimentally validated quarter-wave mirror at terahertz frequencies. The content in this Chapter has been submitted for publication.

Chapter 6 details metasurface designs of half-wave mirrors. To the best of our knowledge, dielectric resonators have not been utilised as half-wave mirrors at terahertz frequencies. A rotationally asymmetric dielectric-resonator design was utilised to provide the required phase shift for half-wave mirrors. This design supports multiple magnetic dipole resonances which allows the required phase difference to be preserved across a broad bandwidth. As with previous designs, this dielectric-resonator metasurface was fabricated at the FMM, and experimentally demonstrated at the University of Adelaide. Next, a performance comparison between metallic- and dielectric-resonator based metasurfaces is detailed. Both metasurfaces are shown to utilise three unique resonances for bandwidth enhancement. The operational mechanism of these structures are discussed and contrasted in this Chapter. The content in the first part of this Chapter has been submitted for publication, while the resonator comparison has been published in a conference (Lee *et al.*, 2018a).

These unique approaches to metasurface designs particularly for polarisation conversion aim to support the development of terahertz technology. Furthermore, these devices are integral towards creating highly efficient, broadband devices in the terahertz region with future applications in many areas such as terahertz communications.

Chapter 2

Terahertz metasurfaces

IN this chapter, the concept of metasurfaces is introduced with emphasis on the aspects relevant to this thesis. Firstly, a general overview of metasurfaces for wavefront engineering is presented. The latter sections in this Chapter review polarisation conversion in metasurfaces, with hints at possible solutions, and indications on addressing their limitations. Lastly, metallic- and dielectric-resonator based metasurfaces are discussed, highlighting their similarities and differences in view of application in the terahertz regime.

2.1 Introduction

Manipulation of electromagnetic waves is typically achieved using conventional optical components such as lenses, beam splitters and prisms. These optical devices are operated based on principles such as refraction and reflection of electromagnetic waves, as well as phase accumulation by wave propagation through materials of a given refractive index. Specifically, as a wave propagates through a medium, the electric field components experience a phase delay according to the local refractive index. Thus, the phase and amplitude of electromagnetic waves can be specifically engineered to control the electromagnetic waves in a desired manner. This results in functionalities such as beam steering, beam focusing, and beam forming.

To achieve polarisation conversion, an optical component has to provide a different response for each orthogonal electric field component, transversal to the propagation direction. This is generally realised by devices commonly known as wave plates. Their operation mechanism is such that as an electromagnetic wave propagates through the wave plate, the orthogonal field components experience different refractive indices and thus undergo different phase delays. The difference in refractive indices is intrinsic to the medium. Such a material is said to be birefringent. To obtain a desired phase difference between the output orthogonal field components, the wave plate thickness has to be adjusted. A larger phase difference does therefore require a larger thickness. Applications in sensing, imaging and communication can benefit from such functionalities. For example, terahertz polarisation-dependent spectroscopy and imaging applications require terahertz wave plates to effectively characterise samples. Nevertheless, conventional wave plates suffer from narrow-band operation, absorption and reflection losses, lack of available materials, device bulkiness and heaviness, which can hinder practical applications. As there is an increasing demand for miniaturised, integrated electromagnetic systems, there is a need to replace bulky optical components with low-profile light-weight devices having corresponding functionalities.

The aim of this chapter is to provide sufficient background information for the latter chapters of this thesis. Section 2.2 will introduce “metasurfaces”, which include transmitarrays and reflectarrays, while highlighting their importance in wavefront engineering. Next, Section 2.3 will briefly discuss the conventional method of polarisation control, which is based on birefringence. The challenges of this conventional approach to provide enhanced birefringence is also detailed in Section 2.3. A potential solution using metasurfaces to address these challenges is discussed in Section 2.3. Here, metasurfaces

that are specifically designed for polarisation control are discussed. The drawbacks of conventional methods are contrasted with those of metasurfaces to give the reader a better understanding behind the motivation of the work in this thesis. In Section 2.4, two generic types of subwavelength resonators constituting metasurfaces, namely, metallic and dielectric resonators, are compared to highlight their similarities and differences in metasurface design. Lastly, a summary is presented in Section 2.5.

2.2 Metasurfaces

One alternative towards providing desired birefringence at specified frequencies is to utilise metasurfaces. This term broadly refers to two-dimensional metamaterials (Zheludev and Kivshar, 2012), and as such includes planar structures consisting of miniaturised metallic or dielectric resonators arranged in subwavelength periodicity. Owing to their capabilities to mould incident waves in unprecedented ways, metasurfaces have attracted a great interest in the scientific community. Carefully designed resonating elements that constitute a metasurface interact with the incident wave by inducing a phase discontinuity that allows shaping the outgoing wavefront. To achieve such a function, either metal or dielectric resonators are required to induce abrupt phase shifts tunable at least within a 2π phase range through resonances — either electric, magnetic or a combination of both modalities. Furthermore, metasurfaces are typically ultrathin, which minimises undesired losses arising from wave propagation in bulk volume. As these metasurfaces are mostly planar, they can be readily manufactured using existing lithography techniques.

In principle, the phase shifts introduced by the resonating elements on the metasurface can collectively alter the route of propagation of the incoming electromagnetic waves. This is achieved by introducing a spatial phase variation on the metasurface. Figure 2.1 shows a conceptual illustration of a linear gradient metasurface at the boundary between two mediums, region 1 and region 2. The resonators are arranged with a subwavelength unit cell size of a which have a fixed phase difference of $\Delta\phi = \phi_1 - \phi_0$ between adjacent resonators. As the spacing between the unit cells is constant, the additional wavevector that is imparted to the incident wave is $\Delta\phi/a$. Thus, the angle of the reflected wave θ_r can be determined by the following relation,

$$k_1 \sin\theta_i + \frac{\Delta\phi}{a} = k_1 \sin\theta_r \tag{2.1}$$

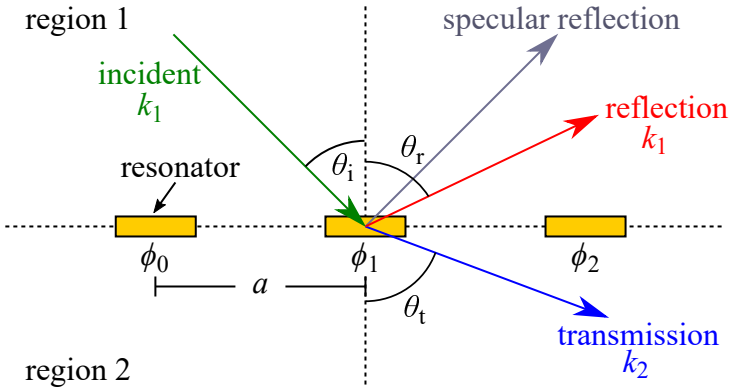

Figure 2.1. Mechanism of a gradient metasurface. Illustration depicting the generalised law of reflection and refraction. The incident wave impinges onto the metasurface at angle θ_i. The reflected wave and transmitted wave are at angles θ_r and θ_t respectively. Wavenumbers of their respective regions are indicated by k_1 and k_2. Adopted from (Al-Naib and Withayachumnankul, 2017).

and the angle of the transmitted wave, θ_t can be determined by the following relation,

$$k_1 \sin\theta_i + \frac{\Delta\phi}{a} = k_2 \sin\theta_t. \tag{2.2}$$

In Eqs. 2.1 and 2.2, θ_i denotes the angle of incidence, while k_1 and k_2 are wavenumbers in their respective regions. From Eqs. 2.1 and 2.2, the outgoing reflected and transmitted beams can be steered into a predetermined direction via a phase gradient that is introduced by the resonating elements on the metasurface. Through thoughtful arrangement of these resonating elements on metasurfaces, a variety of phase gradients can be designed which tailor the outgoing electromagnetic wave. Some examples include beam splitting (Niu *et al.*, 2014; Cheng *et al.*, 2014; Lee *et al.*, 2018b; Wei *et al.*, 2017; Khorasaninejad *et al.*, 2015), beam focusing (West *et al.*, 2014; Liu *et al.*, 2016; Paul *et al.*, 2010; Arbabi *et al.*, 2015), beam steering (Zou *et al.*, 2013; Niu *et al.*, 2013; Staude *et al.*, 2013; Ma *et al.*, 2016) and generation of vortex beams (Chong *et al.*, 2015; Yuan *et al.*, 2017; Yue *et al.*, 2016).

The mechanism behind wavefront control of metasurfaces is in principle the same as that known in reflectarrays (Huang and Encinar, 2008) and transmitarrays (Ryan *et al.*, 2010), which are well established concepts at microwave frequencies. Metasurfaces that operate in transmission are known as transmitarrays while those that operate in reflection are known as reflectarrays. Transmitarrays are more susceptible to unavoidable reflection loss and in order to mitigate this, transmitarrays are often in multilayer form, which adds complexity to fabrication. Reflectarrays on the other hand, are not as susceptible to loss the way transmitarrays are since transmitted components are suppressed by

a ground plane. Ultimately, the choice between transmitarray and reflectarray depends on the desired functionality. The next sections detail some examples of transmitarrays and reflectarrays with a focus on terahertz implementations.

2.2.1 Transmitarrays

In the terahertz region, planar transmitarrays are often used to design lenses. Arrays of complementary V-shaped antennas used as metallic resonating elements have been demonstrated to function as a cylindrical lens, spherical lens and phase holograms (Hu *et al.*, 2013, 2014). In addition, C-shaped resonators in transmitarrays have also been demonstrated as a lens (Wang *et al.*, 2015b) and broadband beam deflectors (Zhang *et al.*, 2013). Micrographs of the transmitarray made up of V-shaped resonators and C-shaped resonators are shown Fig. 2.2(a) and (b) respectively. These C- and V-shaped resonators are chosen as unit cell elements owing to their anisotropy that yields a required 2π phase variation. With this geometry, the excited resonant modes can occur in both the co- and cross-polarised electric fields components. Current vectors excited by co-polarised incident fields will then generate cross-polarised outgoing fields. As such, the energy that is transferred from the incident beam with the same polarisation is minimised, and the energy transferred to its orthogonal polarisation is maximised. Despite these advantages in design, the measured efficiency of these focusing lenses is still relatively low. It is noteworthy that although anisotropic resonators are employed in transmitarrays, they are not intended to operate as wave plates but rather to provide a necessary phase range for wavefront engineering.

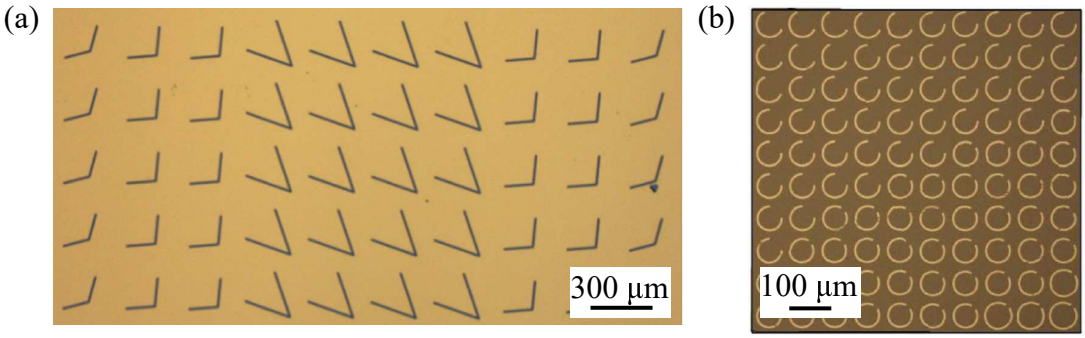

Figure 2.2. Optical micrograph of V- and C-shaped antennas. A section of the array comprising of (a) complementary V-shaped resonating elements, after Hu *et al.* (2014) and (b) C-shaped resonating elements, after Wang *et al.* (2015b).

A full 2π phase range is required with high transmission amplitudes to realise an effective lens. A typical solution to increase efficiency in transmitarrays is to utilise multilayer structures. This multilayer concept adds extra degrees of freedom in metasurface design, which is always essential.

Grady *et al.* (2013) have also demonstrated that by using additional non-resonant layers, beam deflection can be achieved. An illustration of this unit cell design is shown in Fig. 2.3(a). Eight anisotropic resonators with various geometries and dimensions were used to create a linear phase gradient that steered the beam into a specified direction. Two metal gratings which are orthogonal to each other were used to minimise backward co-polarised component and to maximise forward cross-polarised component. This work has been validated with a peak efficiency of 61% at 1.4 THz. With this trilayer design, a broadband terahertz flat lens has also been demonstrated (Chang *et al.*, 2017). This structure has been validated with a 68% overall efficiency at 0.4 THz.

Yang *et al.* (2014) have developed a highly efficient gradient metasurface lens that consists of multiple layers to achieve higher efficiency. This metal-dielectric-metal structure is capable of manipulating the spatial variation of the incident wave and focuses the wave to a desired spot according to the wavelength. The unit cell of this transmitarray includes two resonating element layers. The first layer consists of a square hole and the second layer consists of a square patch of a given width, w. By varying the geometry of the square patch, namely its width, w, the outgoing phase change can be tailored to requirement, provided the unit cell periodicity remains constant. An illustration of the unit cell design is shown in Fig. 2.3(b) and the resultant transmitarray is shown in Fig. 2.3(c). This work has been demonstrated with an average efficiency around 70% at 0.84 THz.

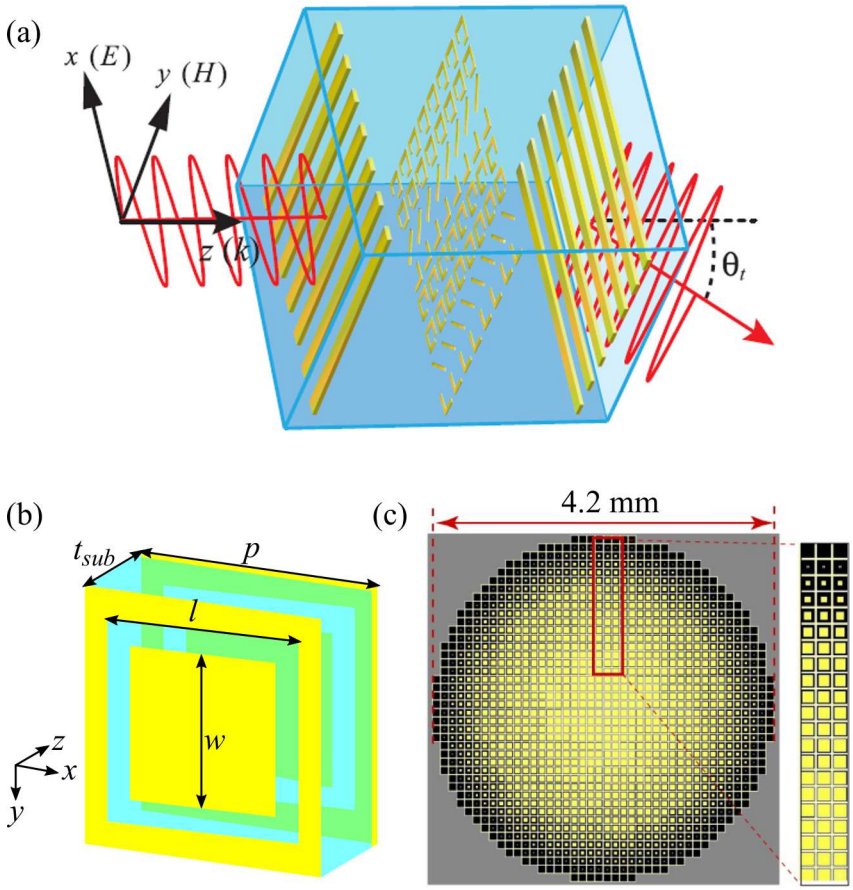

Figure 2.3. Multilayered transmitarrays. (a) Unit cell design of a beamforming metasurface, after Grady *et al.* (2013). (b) Unit cell design of a multilayered transmitarray. The dimensions are as follow: $p = 100$ µm, $t_{\text{sub}} = 50$ µm, $l = 90$ µm, and varying widths, w which change from 0 to 80 µm. (c) Top view of the terahertz metasurface lens, after Yang *et al.* (2014).

2.2.2 Reflectarrays

Metasurfaces that operate in reflection mode are known as reflectarrays. Reflectarrays typically consist of 3 layers. The top layer is made up of resonant metallic elements in a periodic arrangement. The middle layer is a dielectric spacer and the bottom layer is a metallic ground plane. Through variation of the dimensions of the metallic resonating element, the local reflection phase response can be varied. A requirement for effective outgoing wavefront control is a phase coverage of near 2π radians. Inspired by their microwave (Bayraktar *et al.*, 2012) and millimeter-wave (Nayeri *et al.*, 2014; Hu *et al.*, 2008; Pozar *et al.*, 1997) implementations, terahertz reflectarrays are essentially a combination of phased arrays and reflector antennas (Huang and Encinar, 2008).

The earliest demonstration of terahertz reflectarrays was by Niu *et al.* (2013) and showed a device that worked as an isotropic deflector. Figure 2.4(a) shows the intended beam deflecting operation of the metasurface. The terahertz wave is incident at 45° on the metasurface, and is then deflected away from the specular reflection. A square patch was employed as the resonating element with a gradual increase in size across the subarray as shown in Fig. 2.4(a). This progressive increment in size is related to the reflection phase response, as shown in Fig. 2.4(b). From Fig. 2.4(b), it is observed that as the width of the patch increases, the reflection phase shift becomes more negative. This width increment encompasses the near 2π phase coverage required to effectively deflect the incident beam.

For normal incidence, the incident angle θ_i is 0°. As such, Eq. 2.1 is simplified to

$$\frac{\Delta\phi}{a} = k_1 \sin\theta_r, \tag{2.3}$$

where the wavenumber, k_1 can be expressed as $\frac{2\pi}{\lambda_0}$ where λ_0 is the operational wavelength. Hence, the deflection angle of the outgoing wave can be calculated by using the following equation, (Niu *et al.*, 2013; Headland *et al.*, 2017)

$$\theta_r = \arcsin\frac{\Delta\phi\lambda_0}{2\pi a}, \tag{2.4}$$

where a is the unit cell size and $\Delta\phi$ is the phase difference between two neighbouring unit cells. The progressive phase shift, $\Delta\phi$, is fixed to 60°, which sets the number of elements in one linear subarray to six, as this covers one full 2π phase cycle in a periodic manner. Thus, for a = 140 μm, f_0 = 1 THz, and $\Delta\phi$ = 60 °, the angle of reflection is calculated to be 20.5°.

This design was then fabricated and validated using THz-TDS, to examine the performance of this metasurface in response to TE and TM polarised terahertz waves. The corresponding simulated and measured results are shown in Fig. 2.4(c) and (d) respectively. For this particular metasurface, the sidelobe levels of the TM polarisation are significantly lower than for the TE polarisation. Thus, this metasurface has superior performance in TM polarisation as compared to TE polarisation. This difference in performance can be related to oblique incidence, as each polarisation sees a different effective projected patch sizes.

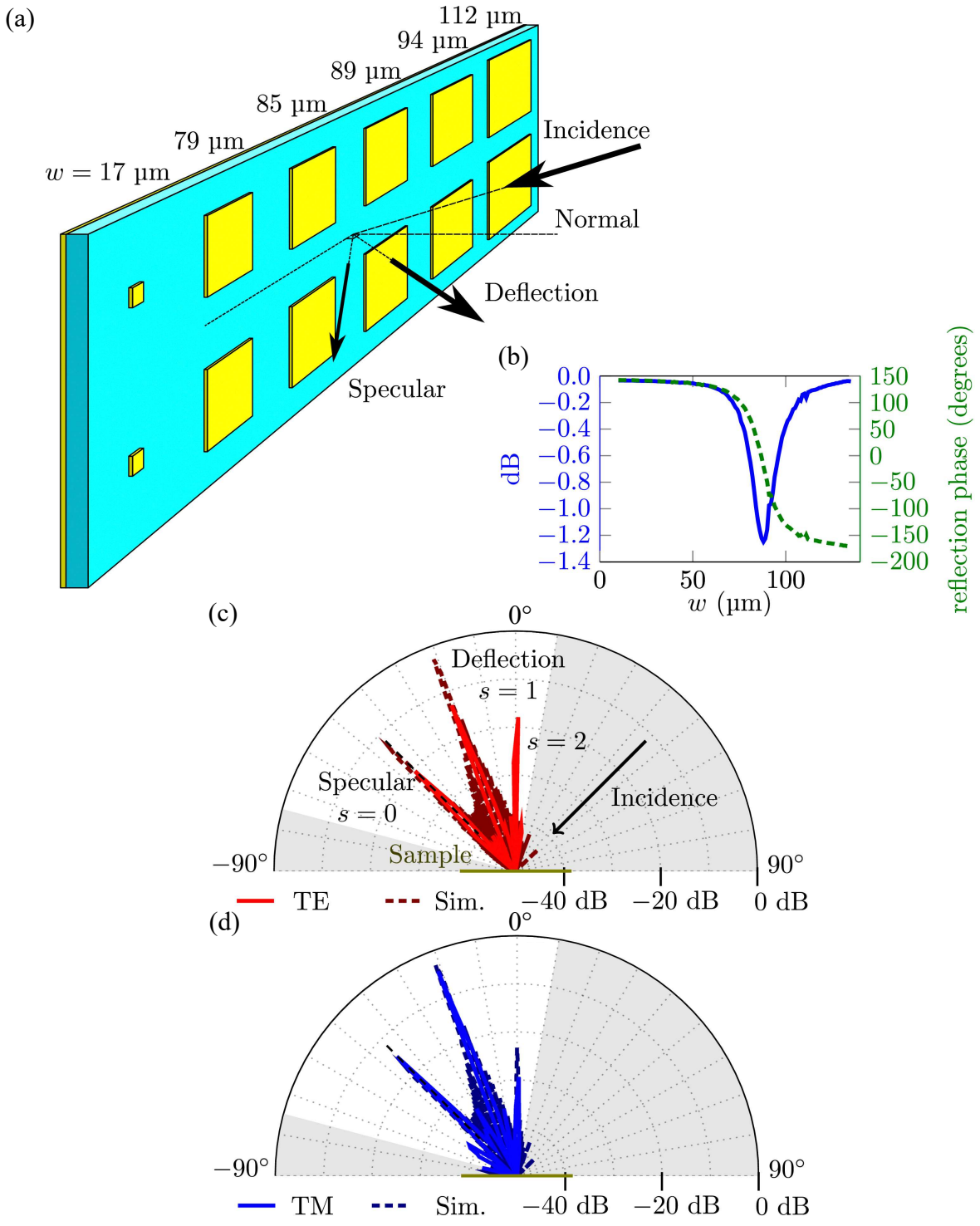

Figure 2.4. Beam deflection reflectarray. (a) Two subarrays with arrows indicating the incident, deflected and specular beams. Parameter sweep of w and its corresponding reflection phase and amplitude response at 1 THz are shown in (b). The far-field patterns for TE and TM polarisations are shown in (c) and (d) respectively. Grey areas are regions that were not measured. Simulation results are given by the dashed lines in (c) and (d). Adopted from Headland *et al.* (2017); Niu *et al.* (2013).

A reflective metasurface made of graphene has also been proposed at terahertz frequencies (Carrasco and Perruisseau-Carrier, 2013). The structure of this reflectarray consists of square graphene patches as shown in Fig. 2.5. Using the same concept of wavefront engineering, this graphene metasurface imparts a tailored phase gradient on the incident electromagnetic wave to shape the outgoing wave into a predetermined angle. By biasing the electric field applied onto the metasurface, the conductivity of graphene can be controlled. This feature would enable dynamic reconfigurability in graphene-based metasurfaces.

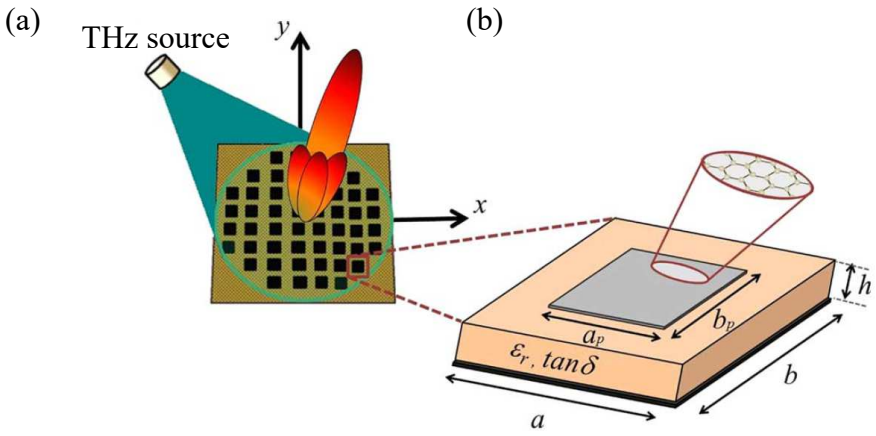

Figure 2.5. Graphene reflectarray. A graphene-based metasurface is shown in (a) and a close up image of one of the unit cell elements is shown in (b). Adopted from Carrasco and Perruisseau-Carrier (2013).

2.3 Birefringent metasurfaces

Aside from wavefront engineering, metasurfaces can provide polarisation conversion capabilities. Conversion between polarisation states is highly desirable for practical application of photonic and terahertz devices. Particularly, in applications in communications and sensing, it is desirable to convert linear polarisation to circular polarisation to ensure that the wave is more resistant to changing environments. The varying environmental conditions would severely affect the scattering of linearly polarised waves as compared to circularly polarised waves.

Conventional methods for achieving polarisation conversion is by using wave plates made of birefringent materials. Some of these materials include crystalline materials (Grischkowsky *et al.*, 1990), paper (Scherger *et al.*, 2011) and wood (Reid and Fedosejevs,

2006). These birefringent materials support different phase delays for each orthogonally polarised wave as shown in Eq. 1.1. In the terahertz region, there is however a scarcity of naturally available materials with strong birefringence, low absorption and small thickness. Standard birefringent wave plates operate at single frequencies because the phase difference between two orthogonal electric field components depends on the wavelength, λ_0, as shown in Eq. 1.1 (Born and Wolf, 2013). For example, at 1 THz, the difference in refractive indices between the orthogonal cuts of quartz is approximately 0.043. Thus, a terahertz quartz quarter-wave plate has to be at least a 8 mm thick in order to be functional, and for a half-wave plate the thickness has to be doubled. Aside from that, paper and wood raise controllability and reliability issues. The aforementioned disadvantages prove the difficulty of integrating polarisation converters made of natural materials into compact terahertz optical devices.

As a solution, metasurfaces can be employed towards providing engineered birefringence at terahertz frequencies. The capability of metasurfaces to offer a 2π phase range over a broad bandwidth with subwavelength resolution addresses the issues of conventional methods. By introducing resonating elements of different lengths and widths, the phase of orthogonal field components can be tuned independently. This section will detail metasurfaces and their effectiveness as polarisation control devices.

2.3.1 Quarter-wave plates

Quarter-wave plates convert linearly polarised waves into circularly polarised waves. In a conventional wave plate, as a 45°-polarised electromagnetic wave passes through the birefringent material, the two orthogonal electric field components experiences different refractive indices. This leads to a $\pi/2$ phase difference between the two orthogonal electric field components, while the amplitude responses remain equal. As mentioned previously, conventional wave plates are inherently bulky and work at discrete frequencies.

Over time, researchers have come up with alternatives to improve the bandwidth of conventional wave plates. Based on Eq. 1.1, it is evident that the variation in phase difference relies on the fixed path difference. Destriau and Prouteau (1949) has shown that stacking a standard half-wave plate with a standard quarter-wave plate results in a broadband quarter-wave plate. This broadband capability can be attributed to partial cancellation of the change of phase retardance in each waveplate, with respect

to the frequency. It has been shown that by increasing the number of waveplates stacked together, the phase retardance can be maintained over a broad bandwidth (Kang *et al.*, 2010; Chen *et al.*, 2013; Masson and Gallot, 2006; Hariharan, 1996; Beckers, 1971; Boulbry *et al.*, 2001; Saha *et al.*, 2012). The fabricated quarter-wave plate by Chen *et al.* (2013) consists of nine crystalline quartz plates of different optical axis rotations and thicknesses. An illustration of the stacked quarter-wave is shown in Fig. 2.6. Although this technique is effective, the resultant device is inherently expensive, bulky, lossy and prone to misalignment as the device contains multiple layers.

Apart from that, periodic gratings have been used to enhance the bandwidth of quarter-wave plates (Lopez and Craighead, 1998; Nordin and Deguzman, 1999; Tyan *et al.*, 1996; Nouman *et al.*, 2016; Zhang and Gong, 2015). An example of a typical silicon grating structure is shown in Fig. 2.7. As the incident wave propagates through the grating along the direction as indicated by k in Fig. 2.7, the structure provides a birefringent phase delay for the field components in the x- and y-directions. The grating, period, depth and bandwidth can be determined using the quasi-static effective medium theory, which is used to describe the refractive indices along the x- and y-directions (Scheller *et al.*, 2010). Essentially the refractive indices along the x- and y-directions which determine the

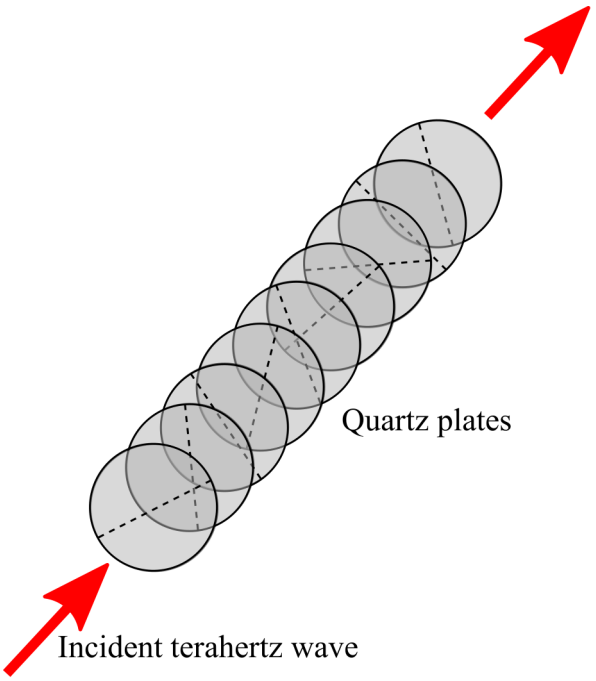

Figure 2.6. Stacked quarter-wave plates. Stacked quarter-wave plates can be used to increase bandwidth. Nine plates are used cohesively to provide achromatic functionality. Each plate is rotated around its axis slightly as indicated by the dashed line, adopted from Chen *et al.* (2013).

phase difference rely on the fill factor of the silicon and the period to wavelength ratio. Thus, the grating itself can be modified to operate around a particular center frequency with an optimised fill factor, which determines the bandwidth of the grating structure.

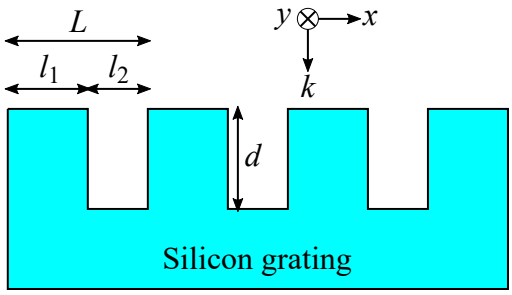

Figure 2.7. Grating quarter-wave plates. Conventional periodic silicon grating used for quarter-wave plates is shown in (b). The subwavelength grating period is given by L. The width of the silicon section is denoted by l_1, the width of the air section is given by l_2 and k indicates the direction of wave propagation. Adopted from Zhang and Gong (2015).

Metasurfaces have been used as alternatives to create quarter-wave plates. Several examples of planar quarter-wave plates made up of metallic resonators were demonstrated at terahertz frequencies (Weis *et al.*, 2009; Imhof and Zengerle, 2007; Wang *et al.*, 2015a; Strikwerda *et al.*, 2009). These planar structures essentially rely on subwavelength resonators to induce birefringence. An example of a metasurface quarter-wave plates is shown in Fig. 2.8. Although many structures are available in the literature, a majority of these structures are still narrow-band. Even though stacking these planar metasurfaces extends their functionality to broadband operation, an increased thickness leads to complication in fabrication processes.

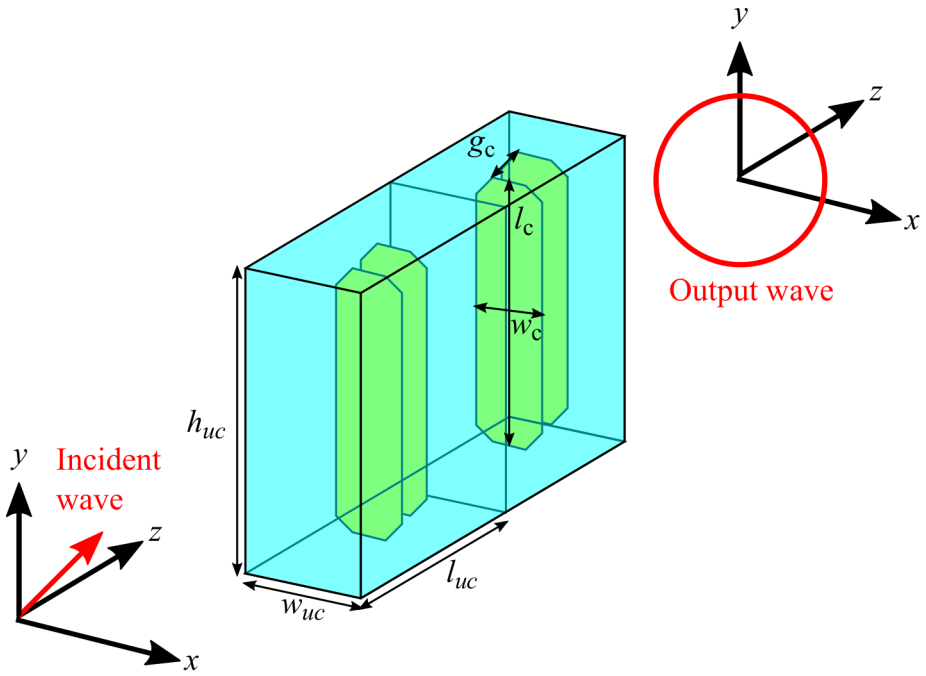

Figure 2.8. Metasurface based quarter-wave plates. Cut-wire pair structure consisting of two unit cells stacked on top of one another to realise a quarter-wave plate, adopted from Weis *et al.* (2009). The 45° linearly polarised wave impinges on the metasurface at normal incidence and outputs as a circularly polarised wave.

2.3.2 Half-wave plates

Half-wave plates rotate linearly polarised waves into their orthogonal polarisation. For circularly polarised waves, half-wave plates change their handedness of polarisation. Unlike quarter-wave plates, half-wave plates introduce a π phase difference between the two orthogonal field components. Conventional wave plates used to achieve this half-wave response also suffer from the same limitations as the quarter-wave plates. At terahertz frequencies, stacking multiple half-wave plates has also been shown to increase the bandwidth (Matsumura *et al.*, 2009) through the same approach as detailed in Section 2.3.1. As such, the resultant device incurs more power loss and cost.

Metasurface-based half-wave plates have been demonstrated with high efficiency and broadband functionality (Cheng *et al.*, 2014; Grady *et al.*, 2013; Xia *et al.*, 2017; Ma *et al.*, 2014; Cong *et al.*, 2013; Mo *et al.*, 2016). A flexible ultrathin reflective half-wave plate based on metasurfaces is shown in Fig. 2.9(a). This metasurface consists of birefringent metallic resonating elements. The anisotropy in this metasurface is provided by the rectangular-shaped resonators, which supports a different phase response for the two orthogonal electric field components. However, aside from narrowband operation, the conversion efficiency of this metasurface is very low, being 27.5% at 0.1 THz (Mo *et al.*, 2016).

Similar to quarter-wave plates, the performance of half-wave plates can be increased by multilayered structures. As demonstrated by Cong *et al.* (2013), a trilayer metasurface is capable of enhancing bandwidth and polarisation conversion efficiency. The operational mechanism of the structure is shown in Fig. 2.9(b). Each layer essentially contains a Fabry-Pérot cavity that improves the efficiency of the metasurface. The wire grids at the top and bottom of each layer allows for the cross-polarisation wave to pass through the structure and suppresses the back propagating co-polarised waves. Hence, only the cross-polarised wave is transmitted through this multilayer metasurface. Although this design has remarkably high transmission amplitudes of 85% over a fractional bandwidth of 80% for a frequency range of 0.45 to 1.06 THz, multilayered structures are complicated to fabricate and difficult to integrate with terahertz devices.

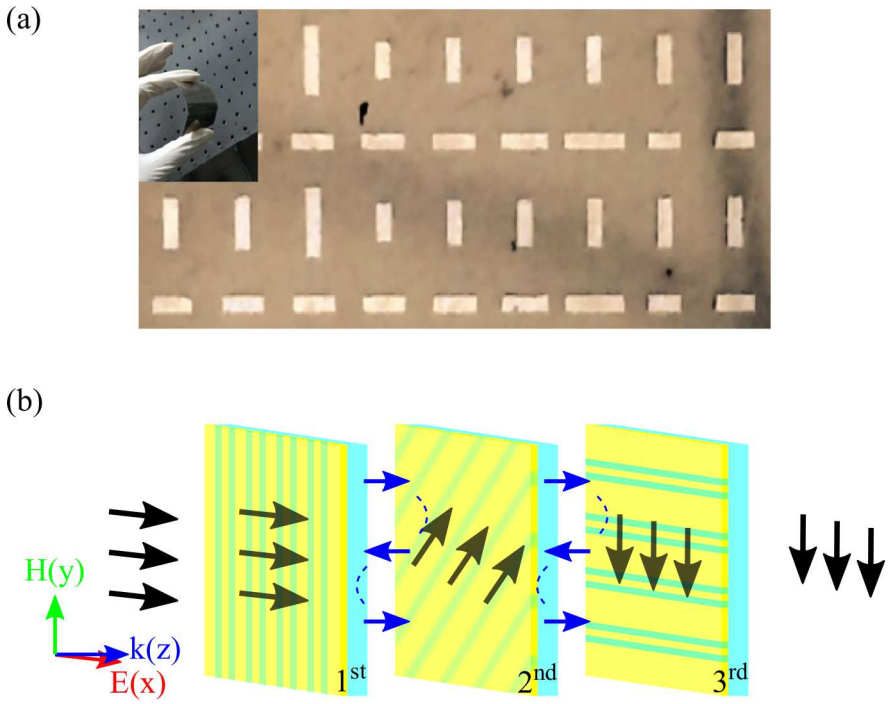

Figure 2.9. Metasurface based half-wave plates. (a) Micrograph of a section of the birefringent metasurface with an inset photograph showing the flexibility of the device, adopted from Mo *et al.* (2016). (b) Schematic of a multilayer metasurface half-wave plate. The electric field distribution is shown by black arrows. The Fabry-Pérot interference between the layers enhances transmission, as indicated by blue arrows. Adopted from Cong *et al.* (2013).

2.3.3 Polarisation beam splitters

A polarisation beam splitter is a device that can split an arbitrarily polarised terahertz wave into its two orthogonal polarisation components. Polarisation beam splitters are particularly useful in terahertz communications as incoming waves can be manipulated independently, which allows for multiplexing of signals in one communication channel (Song *et al.*, 1992). Aside from that, polarising beam splitters can benefit applications in imaging (Wolff, 1994) and polarimetric devices (Mendis *et al.*, 2017). In the terahertz region, wire-grid structures (Tyan *et al.*, 1996; Yamada *et al.*, 2009; Berry and Jarrahi, 2012; Lopez and Craighead, 1998), metamaterials (Peralta *et al.*, 2009), dielectric bi-layers (Li *et al.*, 2010), and stacked metal plates (Mendis *et al.*, 2017) have been shown as functional polarising beam splitters. Wire-grid polarisers are limited to linear polarisation beam splitting and cannot perform circular polarisation beam splitting or beam forming. Thus, it is essential to search for a promising route for structures capable of exotic polarisation beam splitting functions.

Niu *et al.* (2015) has demonstrated a wire-grid polariser consisting of two layers. A subarray of this design is shown in Fig. 2.10(a). The top layer consists of smaller patterned striplines that function as the resonating elements. Owing to the design and geometry of the resonating elements, this polarisation-dependent metasurface has dual-functionality. Firstly, it passes TM-polarised waves through the structure. Secondly, it can operate as a beamforming reflectarray for TE-polarised waves. This configuration is more commonly known as a combination of a reflectarray and a wire-grid polariser. By limiting the complexity to two layers, the transmission and reflection amplitudes still remain remarkably high for both TM- and TE-polarised waves respectively, as shown in Fig. 2.10(b). Apart from that, the 2π phase range is also preserved in the parametric sweep of the width of the resonating elements.

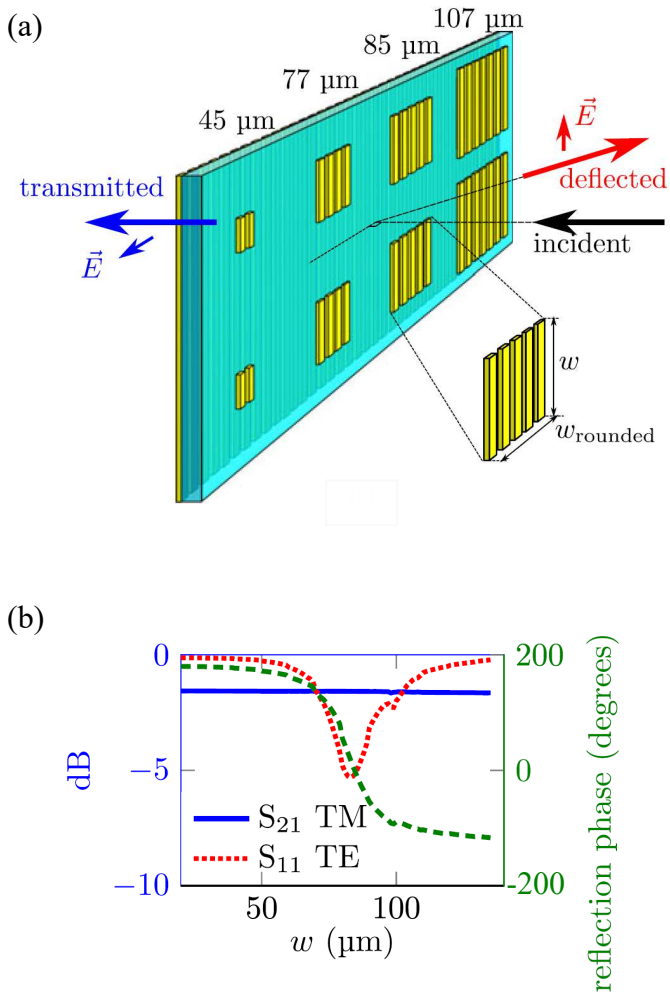

Figure 2.10. Multilayer metasurface designs based on metallic resonators. (a) Subarray of an metasurface that consists of subwavelength metallic striplines as the ground plane and the resonating elements. This structure passes TM-polarisation, but reflects TE-polarisation. (b) The polarisation-dependent transmission and reflection responses based on the parameter sweep of the dimension, w. After Niu *et al.* (2015); Headland *et al.* (2017).

2.4 Resonator types

In order to have full control of electromagnetic waves, it is essential that the resonating elements in metasurfaces can provide high transmission or reflection amplitudes, accompanied by a 2π phase coverage. These resonant elements play a pivotal role in creating the necessary phase shifts which collectively direct the incident waves into the desired direction. For wave plates, the different phase shifts in different axes will yield full polarisation control. The local phase shift generated by these resonators rely on several factors, including geometry, unit cell size and materials. In particular radially asymmetric geometries of the resonators can selectively influence the phase change seen by orthogonal polarisations of electric fields. Efficient beam control and polarisation control can be achieved if the unit cell is of subwavelength dimensions. If the size of the unit cell is greater than or equal to the wavelength of operation, then the wave will be diffracted into several directions, i.e. the diffraction pattern will include grating lobes (Balanis, 1982). Unit cells sizes of half-wavelength or less would avoid these undesired grating lobes.

There are two main considerations when it comes to material selection for creating resonators: The resonant structure can be made of metal or dielectric material. In general, dielectric resonators have a smoother phase variation as a function of frequency as compared to metallic resonators. To have a better understanding of the nature of this phase gradient we examine the following equation of the complex reflection coefficient r, of a single mode of resonance modelled by coupled-mode theory (Qu *et al.*, 2015; Haus, 1984; Fan *et al.*, 2003; Suh *et al.*, 2004):

$$r = \frac{2\pi f_0 Q_a}{\frac{Q_a}{2} + \frac{Q_r}{2} - jQ_rQ_a(\frac{f}{f_0} - 1)} - 1, \tag{2.5}$$

where f_0 is the resonant frequency while Q_a and Q_r describe the absorption and radiation quality factors respectively. Eq. 2.5 shows that the phase response of a resonator is clearly determined by Q_a and Q_r, where Q_a relates to energy lost to dissipation, while Q_r relates to energy released into free-space.

An illustration in Fig. 2.11 shows the reflection phase profiles of varied Q_r for an ideal case, where Q_a is infinite, in a one-port network (Headland *et al.*, 2017). It is observed in Fig. 2.11 that the phase range increases with larger Q_r values. Dielectric resonators typically have better coupling with free space than metallic resonators. Thus, Q_r for metallic resonators is generally higher than Q_r for dielectric resonators. However, a

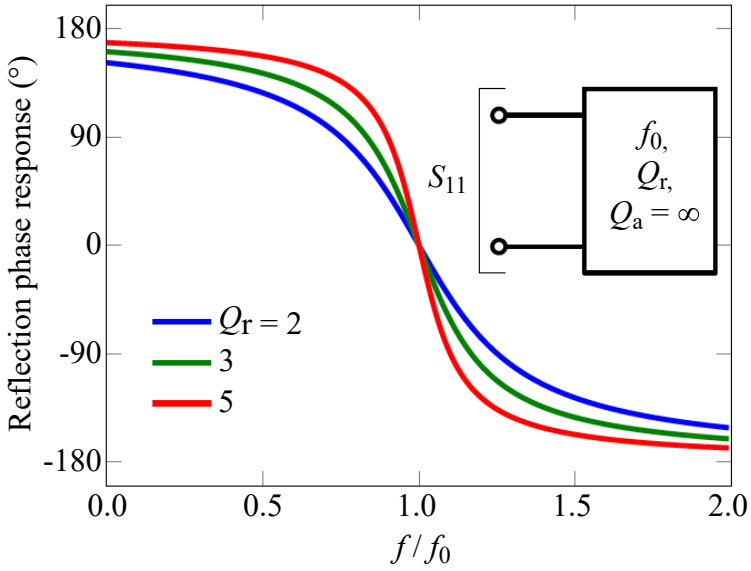

Figure 2.11. Reflection coefficient of patch resonators. The reflection phase response of passive reflective patch resonators in a lossless one-port network with varied Q_r, after (Headland *et al.*, 2017).

higher Q_r would result in a steeper phase gradient, which increases sensitivity as a slight change to the resonance frequency would cause a large change in the phase response. Thus, it is evident that there is a trade-off related to the value of Q_r. Depending on the application, one has to select the suitable quality factor that provides the required phase range. For metasurfaces in wavefront control, it is ideal that Q_r remains moderate as higher Q_r results in narrowband operation, which is not suitable for most terahertz applications. It is also desirable to aim for a large Q_a to ensure highly efficient resonators. The next section will showcase some examples of metasurfaces made up of metallic or dielectric resonators and highlight their interesting features.

2.4.1 Metallic resonators

Most metasurfaces are made up of subwavelength metallic resonators. Their effectiveness in scattering radiation and ease of micro-fabrication makes metallic resonators a formidable choice in metasurface design, particularly at the lower end of the terahertz spectrum. Metallic-resonator metasurfaces typically consist of a resonating element layer which rests on a dielectric substrate. They can be employed to shape wavefronts either in reflectarray (Yu *et al.*, 2011; Huang and Encinar, 2008) or transmitarray (Pfeiffer *et al.*, 2014; Pfeiffer and Grbic, 2013; Chang *et al.*, 2017) configuration, where the latter requires multiple layers. It is a known issue that as the operational frequency increases, the metallic-resonators suffer from increasing Ohmic loss, which results in a decrease in efficiency (Zou *et al.*, 2014).

One notable design by Niu *et al.* (2014) demonstrates the capabilities of rectangular metallic resonators. Birefringent rectangular patch resonators were employed to realise a reflectarray that can effectively deflect normally incident TE and TM polarisations of terahertz waves into opposing directions. From Fig. 2.12(a) which shows the subarray design of the metasurface, we can observe two different sets of elongated resonators. One set is horizontally-aligned for interaction with the TM polarisation, and the other is vertically-aligned to interact with the TE polarisation. By varying the l and w of the resonators, the reflection phase response can be tailored for deflection. A parameter sweep of the varied value of l is shown in Fig. 2.12(b). This gradual increment in l is shown to cover the required 2π phase range with high reflection amplitude. The corresponding simulated and measured results for TE and TM deflection is shown in Fig. 2.12(c) and Fig. 2.12(d) respectively. For this metasurface, the sidelobe levels of the TM polarisation are lower than for the TE polarisation, which implies that the metasurface has better performance in TM polarisation as compared to TE polarisation. Similar to the design presented in Section 2.2.2, a progressive phase change is applied to the incident wave which moulds the reflected wave into a predetermined direction. The metasurface presented by Niu *et al.* (2014) however, is not designed to have broadband functionality and is not highly efficient.

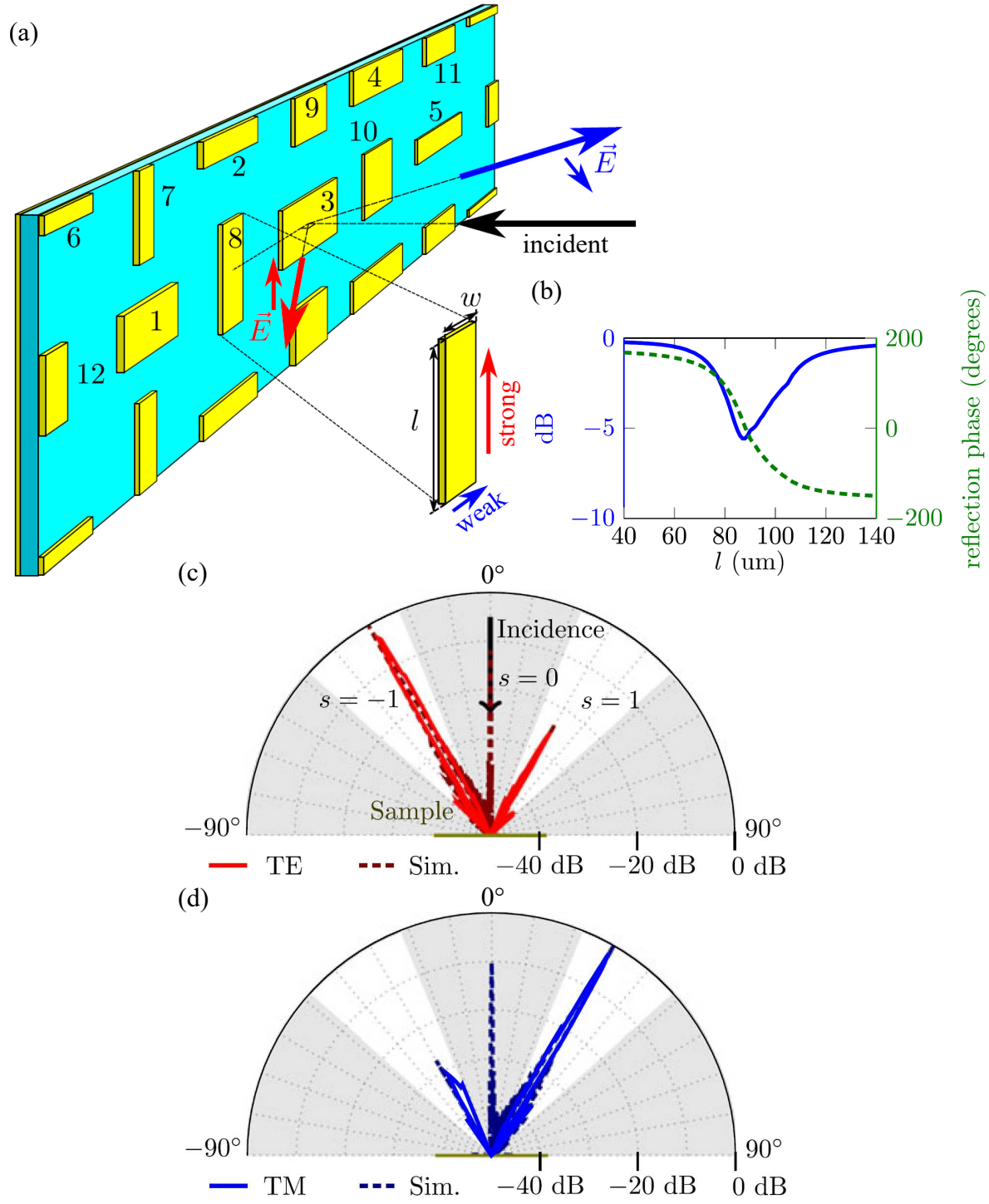

Figure 2.12. Linear beam splitter reflectarray. Beam splitting reflectarray, (a) subarray design with arrows indicating the incident and reflected beams. Parameter sweep of varied values of l and its corresponding reflection phase and amplitude response at 1 THz are shown in (b). The far-field patterns for TE and TM polarisations respectively for the intended deflection are shown in (c) and (d) respectively. Grey areas are regions that were not measurable. Simulation results in (c) and (d) are given by the dashed lines. Adopted from Headland *et al.* (2017); Niu *et al.* (2014).

2.4.2 Dielectric resonators

Dielectric resonators at terahertz frequencies are typically in the form of silicon structures that rest on a metallic ground plane. Usually, dielectric resonators are cylindrical or hexahedral but there essentially no restrictions on the shape. An illustration of typical dielectric resonator geometries are shown in Fig. 2.13. Dielectric resonators operate based on oscillation of displacement currents at specific resonant frequencies (Petosa, 2007). As the free-space electromagnetic wave impinges on the dielectric resonator, the difference in refractive index with the surrounding free space causes reflections of energy within the resonator. Thus, the dielectric resonator behaves as a resonant cavity, where the electromagnetic waves reflects off the boundary on each side of the resonator. This forms a standing wave at a particular resonance frequency. As dielectric resonators operate based on displacement current as opposed to conduction current, Ohmic loss is considerably lower than their metallic counterpart. Dielectric-resonator metasurfaces can operate in either transmission or reflection modes.

For full 2π phase control in a metasurface operating in transmission, i.e. without a ground plane, a single resonance is not sufficient (Pors and Bozhevolnyi, 2013) as it can only contribute up to a π phase range with low transmission. Hence, the utmost important feature of dielectric resonators is the ability to support spectrally overlapping magnetic and electric resonances in a single layer. This is achieved by tuning the geometry and spacing of dielectric resonators which allows for extraordinary phase, amplitude and polarisation control of output waves beyond what metallic resonators can provide in a single layer. Similar to metallic-resonator metasurfaces, dielectric resonators are capable of shaping the outgoing wavefront in transmission (Staude *et al.*, 2013; Wang *et al.*, 2014; Li *et al.*, 2016) and reflection (Zou *et al.*, 2014, 2013; Liu *et al.*, 2014; Headland *et al.*, 2016, 2015a).

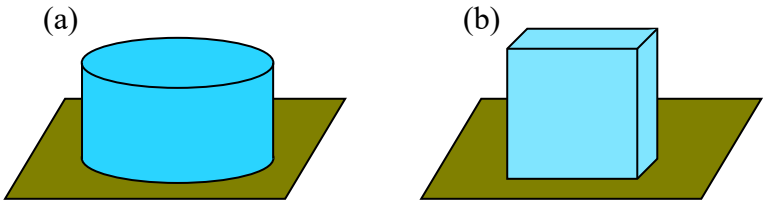

Figure 2.13. Illustration of dielectric resonators. A diagram of typical dielectric resonator geometry with a ground plane, showing (a) cylindrical and (b) hexahedral shapes.

Headland *et al.* (2015a) has shown that uniform silicon-resonator reflectarrays can accommodate a magnetic dipole mode denoted as $HEM_{11\delta}$ in the microwave literature. The schematic of the unit cell resonator is given in Fig. 2.14(a). In uniform array configuration, the structure is excited with a normally incident plane wave, which results in the excitation of the magnetic dipole mode as shown in Fig. 2.14(b). The magnetic dipole resonance can be identified by a circulating electric field within the resonator (Petosa, 2007). We can observe from the reflection amplitude and phase responses of the dielectric-resonator array in Fig. 2.14(c) that the metasurface is very efficient and provides a 2π phase range in the terahertz range.

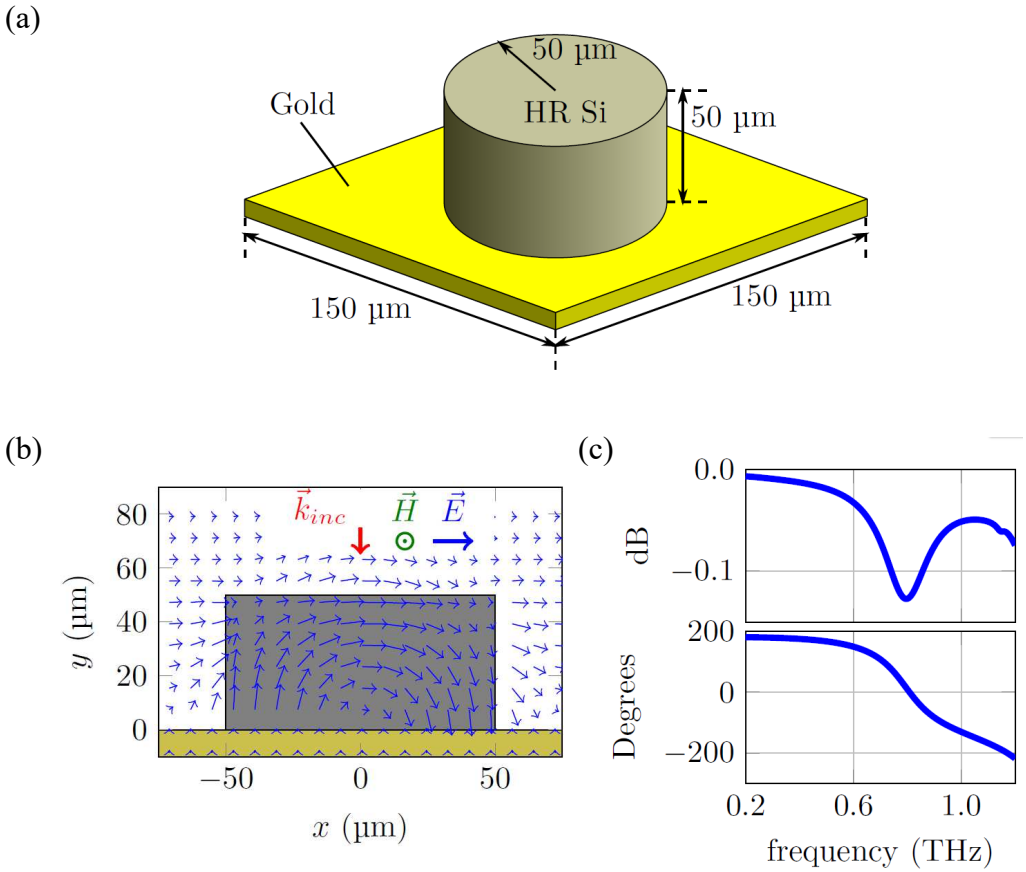

Figure 2.14. Unit cell of a terahertz dielectric resonator. An individual dielectric resonator schematic is shown in (a). The cross-section of the single element in array configuration is shown in (b) upon illumination of normally incident waves. The magnetic dipole mode is excited in the dielectric resonators, as indicated by circular electric fields. The reflection amplitude and phase response is shown in (c). After Headland *et al.* (2015a).

2.5 Challenges and summary

From the detailed analysis of past literature in this field of study, several challenges become evident. Firstly, in the terahertz region, there are limited naturally available materials that exhibit strong birefringence. The low-cost naturally available materials such as paper and wood are not reliable. Furthermore, these materials are not integrable into photonic devices as they are bulky. In addition, crystalline quartz is very costly. Secondly, conventional optical systems that are used to provide complex polarisation conversion at terahertz frequencies consist of multiple bulk optical components which include lenses and mirrors. Thus, these conversion systems are inherently large and hinder practical applications and device integrations. Thirdly, the wave plates made of naturally available birefringent materials operate at single wavelengths. Several researchers have attempted to stack multiple optical devices together to enhance bandwidth. However, this was ultimately followed by a drastic loss of output power, which is not favourable.

In order to meet the demand for highly efficient and broadband devices with designable birefringence, an alternative is sought out. Metasurfaces provide the platform for engineered birefringence at a subwavelength scale. The structures discussed in this Chapter detail both low efficiency and narrow-band behaviours of conventional polarisation converters. Evidently, metasurfaces are capable of providing polarisation control at terahertz frequencies. Furthermore, the amount of bulk optical components in complex polarisation conversion systems can be reduced with metasurfaces. This is because metasurfaces can be designed to exhibit exotic polarisation control that can encompass beamforming functions. This concludes the background portion of this thesis. The upcoming Chapters will detail how metasurfaces can be utilised to provide highly efficient, broadband polarisation control at terahertz frequencies.

Chapter 3

Broadband terahertz circular-polarisation beam splitter

SPLITTING circularly polarised waves is desirable for high-data rate wireless communications and study of molecular chirality at terahertz frequencies. Typically, this functionality is achieved using bulk optical systems with limitations in material availability, bandwidth and efficiency. As an alternative, we employ metasurfaces with spatially varying broadband birefringence to attain the same functionality. In this chapter, we demonstrate that a metasurface designed with gradually rotated birefringent metallic resonators can deflect normally incident left-handed circularly polarised (LHCP) and right-handed circularly polarised (RHCP) waves into different directions. The circularly polarised waves obtained is a result of decomposing linearly polarized waves onto opposing sides. This beam splitting functionality is experimentally demonstrated over relative deflection bandwidth of 53%, namely covering the band of 0.58 to 1.00 THz. Without a limit in the measurement setup, simulation results suggest a bandwidth extending from 0.70 THz to 1.50 THz.

3.1 Introduction

Polarisation control is one of the fundamental functionalities that can be found in various optical components, including polarisers, polarising beam splitters and polarisation converters. Conventional components for polarisation control exploit the strong anisotropy of materials at certain frequency ranges. At optical frequencies, birefringent devices are usually manufactured from crystalline materials (Saha *et al.*, 2012; Masson and Gallot, 2006; Hsieh *et al.*, 2006) while at lower terahertz frequencies, structured materials such as wood (Reid and Fedosejevs, 2006) and paper (Scherger *et al.*, 2011) were shown to possess moderate birefringence. Alternatively, birefringence can be derived from periodic structures in the form of reflectarrays, (Niu *et al.*, 2014, 2015) multilayered materials (Lopez and Craighead, 1998; Yu *et al.*, 2006; Tyan *et al.*, 1996; Suzuki *et al.*, 2016b) or gratings (Lopez and Craighead, 1998; Nordin and Deguzman, 1999; Tyan *et al.*, 1996).

One functionality of interest in polarisation control is beam splitting for circular polarisation. Devices capable of polarisation beam splitting can be constructed by assembling multiple anisotropic material sections together, with their fast axis rotated relative to each other. However, drawbacks of these conventional polarisation-sensitive devices include narrow operation bandwidth, high cost, low efficiency, and bulkiness. In the terahertz region, an additional issue is related to material availability, since few natural materials exhibit strong birefringence with low loss (Reid and Fedosejevs, 2006; Scherger *et al.*, 2011). Circularly polarised terahertz waves are important for studying chiral structures as many molecules in biology and chemistry are chiral and respond differently to LHCP and RHCP waves (Ferguson and Zhang, 2002). Additionally, circular polarisation can increase channel capacity in wireless communications.

As an alternative, metasurfaces can provide designable birefringence at desirable frequencies, among other properties not commonly found in nature (Withayachumnankul and Abbott, 2009). For example, dielectric chiral structures made of silicon Khorasaninejad and Crozier (2014) and titanium dioxide nanofin gratings (Khorasaninejad *et al.*, 2017) capable of circular polarisation beam splitting have been demonstrated at optical frequencies. Aside from that, metal nanoantennas (Shaltout *et al.*, 2014) at the mid-infrared range and rotated microstrip patches (Huang and Pogorzelski, 1998) at microwave frequencies have also been demonstrated with a similar concept. Likewise, dual-image holograms can be generated because of different responses to LHCP and

RHCP waves (Khorasaninejad *et al.*, 2016; Levy *et al.*, 2005; Desiatov *et al.*, 2015). However, many of these existing designs are either inherently lossy, complicated and/or narrowband. At terahertz frequencies, there are to-date, no existing metasurface designs capable of circular polarisation beam splitting.

In this chapter we detail the design of the ultrathin broadband and efficient reflective beam splitter for circular polarisation operating at the terahertz band. Relying on the concepts of birefringent metamaterials and localised phase control, the structure employs metallic planar coaxial disk-ring resonators over a ground plane as phase-shifting elements. Each element offers three neighbouring resonances that altogether provide a half-wave-mirror response over a large bandwidth. A proper relative orientation between the cells results in a linear phase ramp with a positive or negative phase trend depending on the handedness of circular polarization. Effectively, this metasurface deflects incident LHCP or RHCP waves into opposite sides with predetermined angles away from specular reflection. The design of the metasurface is detailed in Section 3.2. Section 3.3 details the fabrication process used to manufacture this device. The measurement set-up is shown in Section 3.4 where the design is characterised using a customised fibre-coupled terahertz time-domain spectroscopy (THz-TDS) system. A thorough discussion of the results obtained is shown in Section 3.5 followed by a conclusion in Section 3.6.

3.2 Design

The unit cell for the reflective beam splitter is shown in Fig. 3.1. A planar coaxial disk-ring resonator of gold with a thickness of 200 nm makes up the top layer of this unit cell. The middle layer is 27 µm thick, and composed of low loss cyclo olefin copolymer (COC) which has a relative permittivity of $\epsilon_r = 2.34$ and loss tangent $\tan\delta = 0.0007$ (Peytavit *et al.*, 2011; Nielsen *et al.*, 2009). This dielectric material used as a spacer has lower dielectric loss compared to polydimethylsiloxane (Headland *et al.*, 2015b) and other polymers (Walia *et al.*, 2015) with $\tan\delta = 0.06$ used in the base half-wave mirror designed by (Cheng *et al.*, 2014). In order to avoid grating lobes, the unit cell size is chosen to be 120 µm, which is less than the shortest operating wavelength of 200 µm at 1.50 THz. The ground plane is a gold layer with a thickness of 200 nm.

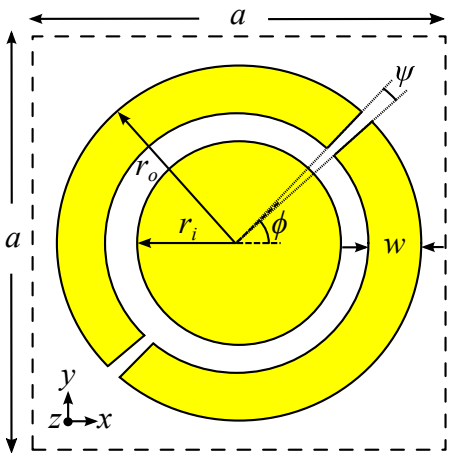

Figure 3.1. Unit cell design. The dimensions are as follows: $a = 120$ µm, $r_i = 28$ µm, $r_o = 48$ µm, $w = 12$ µm, $\psi = 4.11°$. The fast axis is rotated with an angle of ϕ as indicated. A uniform array of this resonator functions as a broadband half-wave mirror.

When this unit cell is repeated periodically along the x and y axes, it functions as a half-wave mirror over 0.70 – 1.50 THz. Figure3.2(a) shows the reflection phase profile of the uniform array in response to the two orthogonal electric field components. From this figure, we can infer the three resonance modes from the zero phase crossings. These resonances support a phase difference of close to one π radian between the two orthogonal linearly polarised electric field components between 0.70 – 1.50 THz as shown in Fig. 3.2(b). We then rotate the resonators with a progressive, anti-clockwise rotation angle of 36° with respect to the center of each element to examine the phase difference between the two linear orthogonal electric field components. The results are

presented in Fig. 3.3, indicating that the near-π phase difference is maintained over a 0.75 – 1.40 THz band.

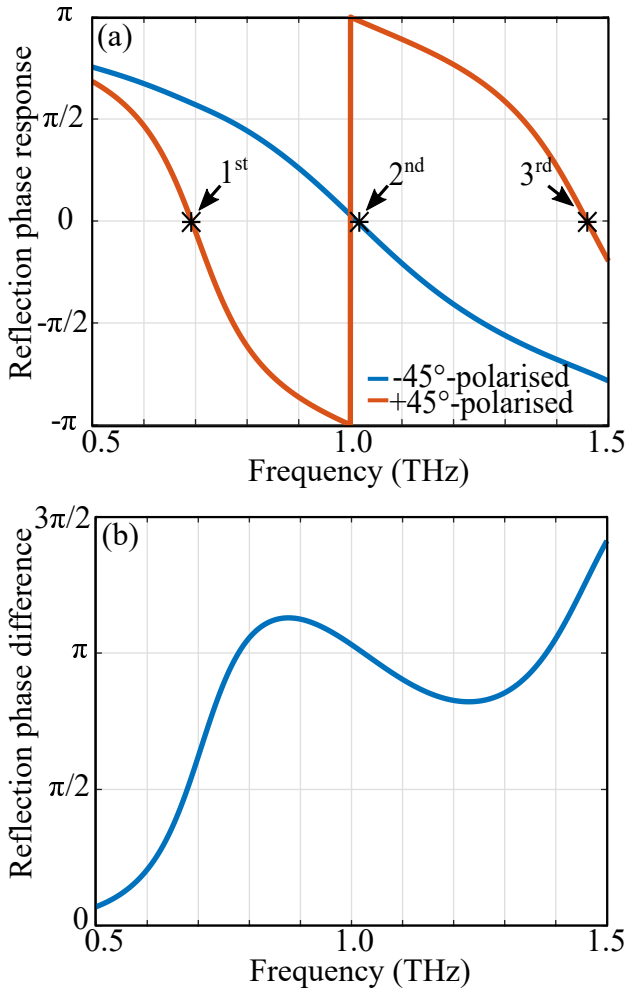

Figure 3.2. Reflection phase responses for the uniform resonator array. (a) The phase profiles in response to $+45^\circ$ and -45° linearly polarised waves. The arrows indicate the positions of the 3 resonance modes that altogether support a continuing near-π phase difference between the two orthogonal electric field components over a 0.70 – 1.50 THz band as shown in (b).

The mechanism of this half-wave mirror can be understood from resolved current distributions in response to decomposed incident electric fields. At the lowest resonant frequency of 0.7 THz, as shown in Fig. 3.4(a), the arcs of the coaxial disk-ring resonator behaves as a dipole resonator which couples with the $+45^\circ$ linearly polarised wave. Thus, a zero phase shift is imposed upon reflection. The -45° linearly polarised wave does not resonate at this frequency, and hence a $-\pi$ reflection phase is imposed by the ground plane. At the second resonance, as shown in Fig. 3.4(b), a set of shorter dipoles is excited in the arcs when coupled with the -45° linearly polarised component.

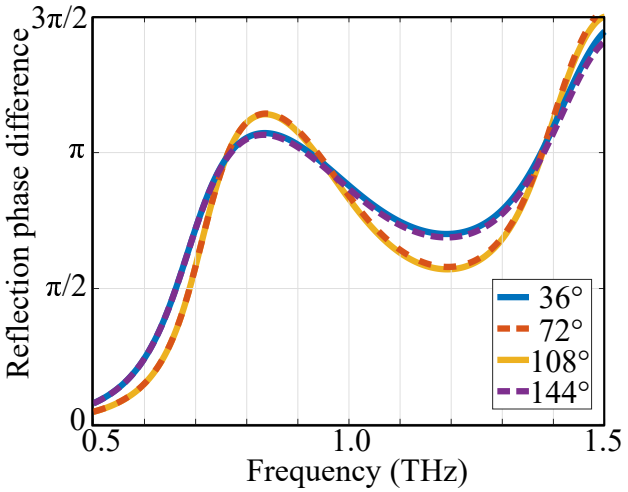

Figure 3.3. Reflection phase response for the array. Reflection phase response where the resonator elements in the array are rotated as by the indicated angles with respect to the center of the unit cell. The phase profiles in response to $+45^\circ$ and -45° linearly polarised waves. The near-π phase difference between the two orthogonal electric field components is maintained over a 0.70 – 1.50 THz band despite rotating the resonating elements.

A zero phase shift is therefore imparted upon reflection. The $+45^\circ$ linearly polarised component will be reflected off the ground plane at this frequency, thus the phase difference between the two orthogonal components will be close to π radian. At the third resonance frequency, the disk and the arcs of the coaxial disk-ring resonator together exhibit a set of dipoles which couple to the $+45^\circ$ linearly polarised wave as shown in Fig. 3.4(c). Again, this imposes a zero phase shift on reflection. The -45° linearly polarised wave however, sees a $-\pi$ phase change at this frequency. Superposition of tailored multiple resonant modes on the metasurface results in broadband half-wave response.

For circularly polarised waves, such a half-wave mirror preserves the handedness upon reflection (Plum and Zheludev, 2015). In principle, by rotating the mirror around the propagation axis (z-axis), we can impose a phase shift to the reflected circularly polarised waves. This rotation can be applied locally at the unit cell level to create a spatially varying phase response across the mirror surface. As a result, the outgoing wavefront can be controlled to create a desirable field distribution or radiation pattern (Headland *et al.*, 2017). This is consistent with the aforementioned traditional method of rotating the fast axis of a half-wave plate in sectors, to form a larger structure with beam splitting functionality.

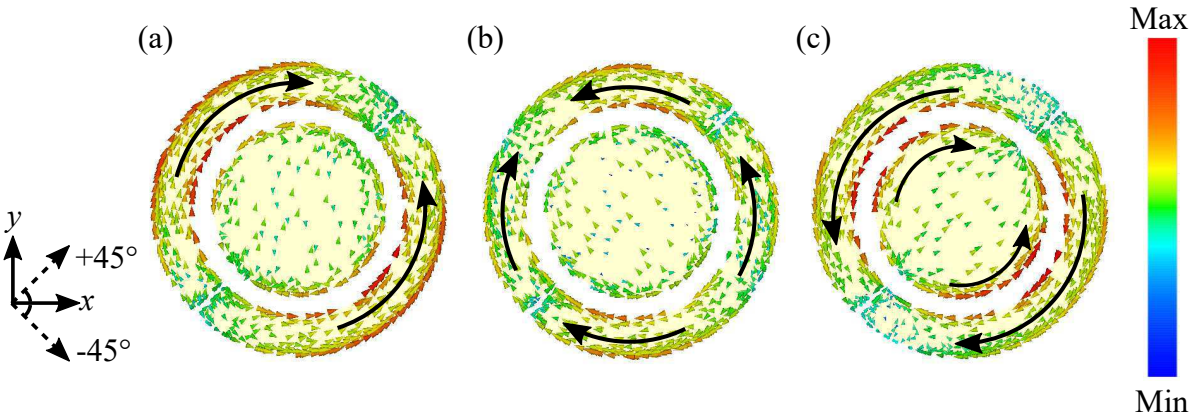

Figure 3.4. Surface current distributions on the coaxial disk-ring resonator. Surface current distributions on the coaxial disk-ring resonator for incident 45°-polarised waves at the three resonant frequencies. (a) 0.70 THz, (b) 1.04 THz, and (c) 1.46 THz.

Mathematically, the relation between the cell rotation and the phase response for circular polarisation can be explained in the formalism of the Jones matrices. Each unit cell in Fig. 3.1 can be loosely considered as a local half-wave mirror, which can be represented by a Jones matrix, $\mathbf{M}(\phi)$ where the fast axis of the unit cell is at ϕ angle with respect to the x-axis. The incident LHCP and RHCP Jones vectors are given by $\mathbf{A}_{\pm}$, where the $+$ and $-$ signs indicate their respective handedness. Thus, the resultant Jones vector can be determined by the following equation,

$$\begin{aligned}\mathbf{J}(\phi) &= \mathbf{M}\mathbf{A}_{\pm}, \\ &= \begin{bmatrix} -\cos(2\phi) & -\sin(2\phi) \\ -\sin(2\phi) & \cos(2\phi) \end{bmatrix} \frac{1}{\sqrt{2}} \begin{bmatrix} 1 \\ \pm i \end{bmatrix}, \\ &= \frac{1}{\sqrt{2}} \begin{bmatrix} -1 \\ \pm i \end{bmatrix} \exp(\pm i 2\phi).\end{aligned} \tag{3.1}$$

It is observed from the resultant Jones vector $\mathbf{J}$ that the incident wave retains its polarisation handedness upon reflection, given a change in the propagation direction. This is accompanied by a $|2\phi|$ phase discontinuity that is imposed to the reflected wave. The sign for this phase discontinuity is dependent on the handedness of the incident polarisation as shown by $\mathbf{A}_{\pm}$.

This means that, for our metasurface, the phase of the reflected wave can be controlled for a full continuous 2π phase range by rotating each individual element without affecting the polarisation response. Thus, a progressive phase distribution, i.e., a linear phase ramp, can be implemented to deflect the normally incident wave into

a predetermined angle away from the specular direction. Importantly, LHCP and RHCP waves will undergo different phase ramps with opposite signs. Applying phase wrapping in a 2π range results in a periodically-repeated subarray that forms the metasurface. For our design, each single subarray comprises 5 unit cells, each with a progressive $\Delta\phi = 36^\circ$ cell rotation. As shown in Fig. 3.5, one subarray covers a phase gradient of 2π. The deflection angle of the outgoing wavefront can be calculated by using the following equation, (Niu *et al.*, 2013; Headland *et al.*, 2017)

$$\theta_r = \arcsin \frac{\Delta\phi c}{\pi f_0 a}, \tag{3.2}$$

where a is the unit cell size, $\Delta\phi$ is the relative angle between two adjacent unit cells, c is the speed of light in vacuum and f_0 is the operation frequency. Due to the handedness-dependent phase sign as discussed in Eq. 3.1, this equation suggests that, for an incident LHCP or RHCP wave, the outgoing wavefront will be deflected to $-\theta_r$ or $+\theta_r$ respectively. Thus, this metasurface operates as a circularly polarised beam splitter.

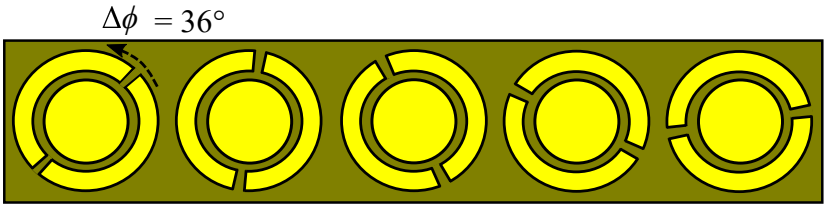

Figure 3.5. Subarray design for beam deflection. Each subarray for beam deflection consists of 5 resonating elements rotated by $\Delta\phi = 36^\circ$ cumulatively.

We simulate this structure using the frequency-domain solver in CST Microwave Studio. The surface impedance model accounting for metal loss in gold (Niu *et al.*, 2013) is used to model the thin metal layers in the simulation. In order to simulate an infinite gradient array, we apply periodic boundary conditions to the subarray with a Floquet port excitation of LHCP and RHCP waves. Numerical results are shown in Fig. 3.6. We can observe that the metasurface can split circularly polarised waves with a minimum deflection angle of $\theta_r = \pm 20^\circ$ over a large bandwidth. Its broadband operation is inherent from the original uniform half-wave mirror. The deflection angle is frequency-dependent as shown in Fig. 3.6 and is in good agreement with the analytical results from Eq. 3.2. Figure 3.6 also reveals higher diffraction orders that are caused by the subarray periodicity, but are largely suppressed by the phase gradient of the metasurface.

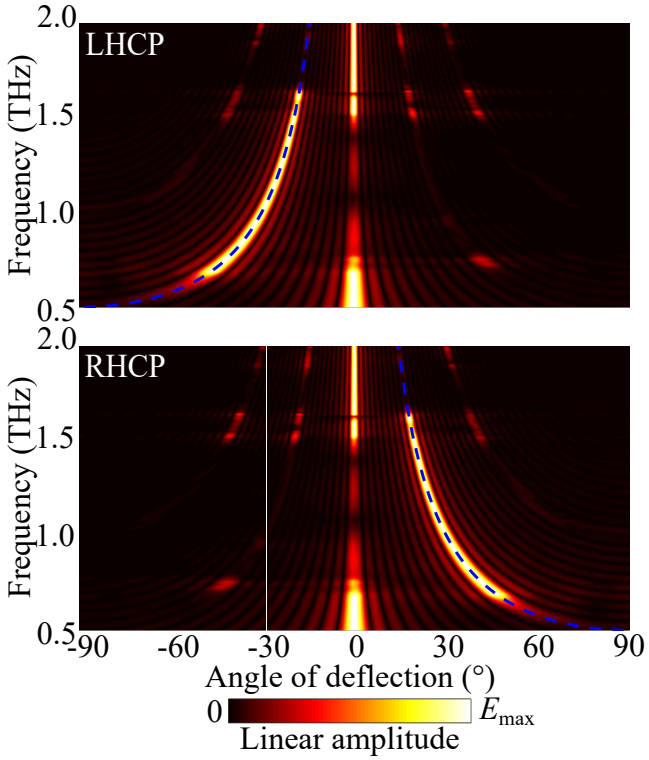

Figure 3.6. Frequency-dependent far-field patterns. The simulated far-field patterns for LHCP and RHCP excitations across the scanning range. The blue dashed lines indicate the analytical solution from Eq. 3.2.

3.3 Fabrication

A fabricated sample is shown in Fig. 3.7. The reflective circular-polarisation beam splitter is realised using microfabrication techniques. A 3-inch silicon wafer is cleaned with solvents and dried with compressed nitrogen. The ground plane layer is defined using 200 nm of gold (Au) deposited with 20 nm chromium (Cr) adhesion layer by electron beam evaporation (PVD75, Kurt J. Lesker). This gold-coated wafer is coated with 27 μm thick COC, by a double-layer spin coating process. This process involved spin coating of the liquid phase COC followed by curing. Subsequent photolithographic patterning is performed to define the unit cell resonators covering a 50 mm by 50 mm area. This is then followed by metal deposition, under conditions identical to the ground plane, of Au 200 nm with Cr 20 nm. Lift-off patterning is then done in an acetone bath with ultrasonic agitation to complete the fabrication.

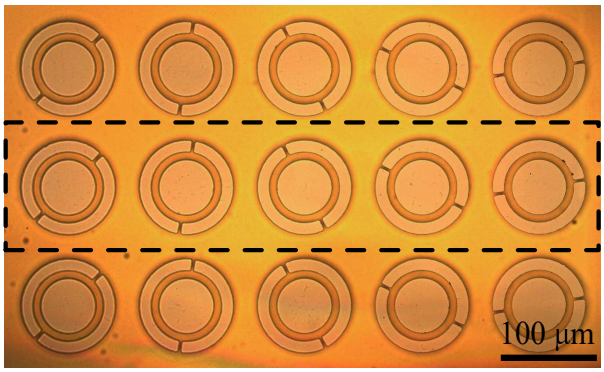

Figure 3.7. Optical micrograph of the fabricated sample. An optical micrograph of a portion of the fabricated sample is shown. The dashed rectangle encloses a single subarray consisting of 5 resonating elements rotated by 36° cumulatively.

3.4 Measurement

We use a fiber-coupled (THz-TDS), the Tera K15 by Menlo Systems GmbH, to conduct the experiment. A photo of the experiment set-up for angular scanning is shown in Fig. 3.8(a) and the corresponding schematic is shown in Fig. 3.8(b). For this measurement, we use lenses with a focal length of 5 cm for beam collimation and focusing. A collimated, vertically-polarised terahertz beam with a diameter of approximately 25 mm illuminates the sample at normal incidence. The sample then deflects the beam to different directions. This deflected beam is detected by a linearly polarised receiver attached to a rotating mount that adjusts the angle of linear polarisation. Wire-grid polarisers are employed to ensure polarisation purity. In order to measure the radiation across an angular scanning range, we fix the emitter and the sample on a rotating arm with the pivot aligned to the sample surface. This arm then rotates over the scanning range between $+30^\circ$ to $+60^\circ$ and -30° to -60°, progressively acquiring pulses at increments of 1°. It is noted that the clearance between components prevent us from reaching the minimum deflection angle of 20° as estimated by the simulation for the highest operation frequency of 1.50 THz. A gold-plated mirror with specular reflection at 45° is used to normalise all the measurements. All scans are conducted under ambient conditions. It is noteworthy to mention that THz-TDS sources are typically linearly polarised. In order to generate RHCP waves, the linearly polarised terahertz waves has to pass through a quarter-wave plate, which converts linearly polarised waves into RHCP waves. For LHCP waves, the quarter wave plate has be rotated by 180°.

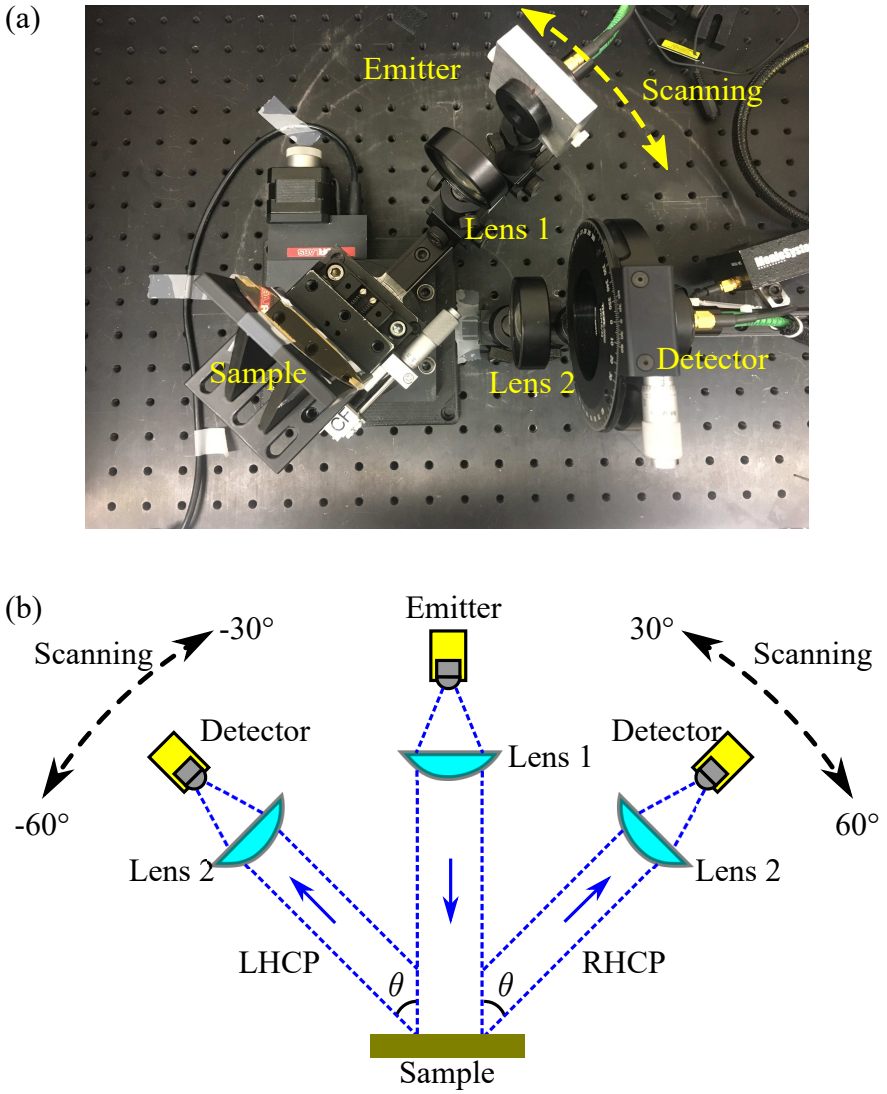

Figure 3.8. Photo and schematic of experimental set-up. (a) Photo of the experimental set-up. The scanning range here is used to measure RHCP terahertz waves. Alternatively, the emitter is rotated to the opposite side to measure the LHCP terahertz waves. (b) Schematic of the experimental set-up. The negative and positive angular ranges are used to measure LHCP and RHCP terahertz waves respectively. Here, θ represents the deflection angle.

3.5 Results

Based on the setting discussed Section 3.4, two sets of measurements are taken. The first set performs the angular scans of the designed metasurface for vertical-in vertical-out (VV) deflection and vertical-in horizontal-out (VH) deflection. More specifically, the exciting vertically polarised waves can be decomposed to the LHCP and RHCP waves that are deflected to different sides. These deflected circularly polarised waves are then measured for their vertical and horizontal components. This measurement is carried out to observe the angular deflection for LHCP and RHCP respectively and its broadband behaviour. A second set of measurements is taken to infer that our metasurface is capable of discriminating circular polarisation. This set of measurements gauges the polarisation ellipses of the deflected beams. For this measurement, the detector is rotated around the propagation axis to obtain measurements for 7 different polarisation angles from 0° to 180° with a step size of 30°. The polarisation measurements are repeated at different deflection angles from $\pm 30^\circ$ to $\pm 60^\circ$ with 5° increments.

Figure 3.9 shows the amplitude spectra obtained at different scanning angles from the first set of measurements in comparison to the simulation results. An array factor and an incident Gaussian beam profile is applied to the simulated radiation pattern to emulate the results obtained from the measurement. The array factor is a function that is multiplied with the radiation pattern of an individual subarray to obtain the directivity of the entire array. This array factor is dependent on the position and near-field response of each subarray. We can observe that the measured, simulated and analytical results are in general agreement. However, there is a slight angular shift in the measured results as compared to the analytical result. This shift is attributed to alignment tolerances in the experiment set-up. It is also noted that the beam width of the simulated results is slightly smaller than the measured results. The slight difference in the beam widths is likely because of the finite aperture size of the detector.

From Fig. 3.9, it appears that linearly polarised waves are decomposed to two sides as LHCP and RHCP waves across the frequency range of 0.58 THz to 1.00 THz. The operational bandwidth of our metasurface is determined by calculating the range of frequencies where the maximum amplitude corresponds to the expected deflection angle. Hence, the measurable fractional bandwidth of our metasurface is calculated to be 53%. We expect this structure to work at higher frequencies which could not be measured due to the angular clearance of the setup. As predicted by full-wave simulations, the bandwidth for this metasurface should be much larger, up to 73%

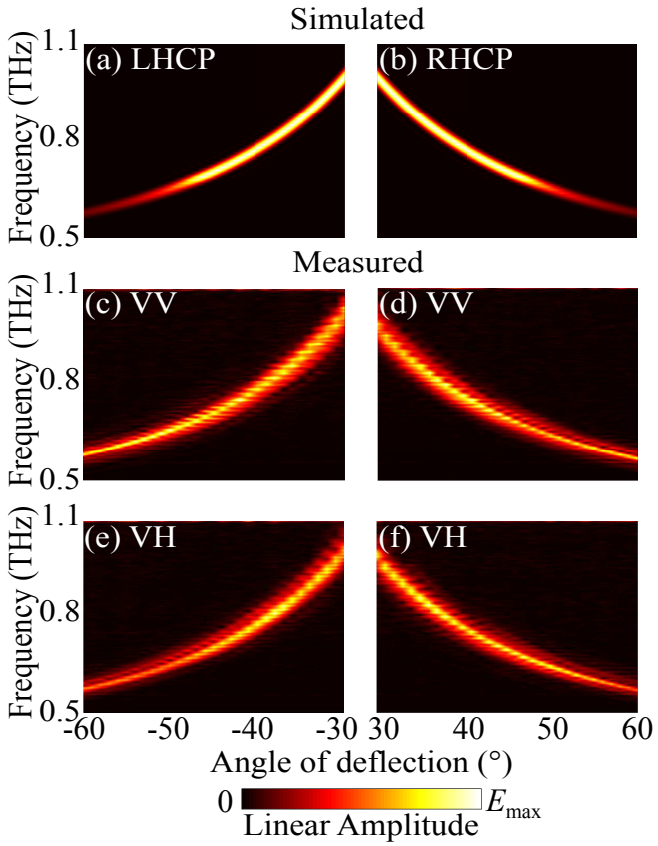

Figure 3.9. Normalised amplitude spectra. Normalised amplitude spectra from the simulation (a,b) and the measurement (c-f). Each spectral map is normalised to its own maximum. Figures on the left and right columns correspond to the negative and positive scanning ranges in the experiment set-up. Abbreviations VV and VH denote the incoming vertical polarisations and corresponding received polarisation, namely vertical 'VV' or horizontal 'VH'.

which covers a frequency range from 0.70 THz to 1.50 THz according to Fig. 3.6. A slight discrepancy in the lower frequency limit could be due to fabrication tolerances. In addition, a slight asymmetry between the measured LHCP and RHCP results for both VV and VH components can be attributed to the minor adjustments made to the experiment set-up to compensate the non-ideal Gaussian beam profile of the system. Further information regarding this non-ideal Gaussian beam profile can be found in Appendix A. This measurement highlights the angular deflection and broadband behaviour of our metasurface.

Figure 3.10 illustrates the normalised amplitude spectra obtained from measurement at a scanning angle of $+50^{\circ}$. The spectra include the VV deflection and VH deflection. As our metasurface is designed to split circularly polarised waves, the resulting power on each side upon incidence with linearly polarised waves will be 50%. Consequently, the power will be split once again, at each side, as the circularly polarised waves are measured for their vertical and horizontal linearly polarised components. At this point, the measurable power will be 25%, which corresponds to a normalised linear amplitude of 0.50 for both vertical and horizontal linearly polarised components. At 0.65 THz, as shown in Fig. 3.10, we can observe that the linear amplitude for the vertical and horizontal components is 0.34, compared with the expected amplitude of 0.50. The beamwidth difference between the VV and VH components can be attributed to the different angular coverage intrinsic to the detector as it scans the VV and VH components. As the amplitude for both vertical and horizontal components are equal, this measurement would suggest that our metasurface is capable of deflecting circular polarisation.

While attempting to determine the efficiency of our metasurface, several underlying factors require consideration. We observe that the measured results exhibit beam broadening, which is due to the finite aperture size of the detector. Furthermore, these measurements are normalised using a mirror reference where the specularly reflected beam is of higher amplitude as compared to the sample measurement. This high

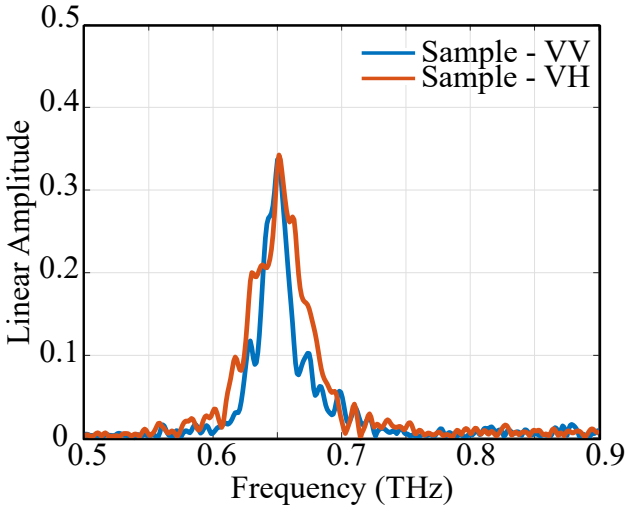

Figure 3.10. Measured normalised amplitude spectra at a specified angle. The measured normalized amplitude spectra at a deflection angle of $+50^{\circ}$ is shown. The red and blue lines represent the measured vertical (VV) and horizontal (VH) reflected waves for a vertically polarised excitation.

amplitude can be attributed to a larger projected aperture size of the reference mirror at specular reflection. A smaller projected aperture size of the sample off the specular direction causes stronger diffraction in the reflected beam. This is a known property in optical systems, which is referred to as anamorphic magnification as illustrated in Figure 3.11. Based on these aforementioned factors, it is difficult to obtain an accurate measurement of efficiency for our metasurface.

Nevertheless, we accounted for the effects of anamorphic magnification on the measured results to determine the efficiency of our metasurface. Figure 3.12 shows the measured and simulated efficiencies of our metasurface. For the measured data, a Gaussian beam profile on a mirror reference is used to normalise the measured data. Similarly, for the simulation of a mirror reference, an array factor with a Gaussian beam profile is applied to the radiation patterns to emulate the results obtained from the reference measurement. The total power of the measured and simulated reflected beams are then calculated by integrating the power over the angular beamwidth of $\pm 30^\circ$ to $\pm 60^\circ$ at each frequency. The measurable efficiency is limited to a range of frequencies where the entire main beam is within the scanning range of measurement. The simulation suggests a maximum efficiency of 96% at 1.05 THz. The approximate maximum efficiency obtained from measurement is 61% at 0.78 THz. Reduction in measured efficiency despite accounting for anamorphic magnification can be attributed to other beam broadening factors such as the finite aperture size of the detector. Since the beam is a result of convolution with the angular response of the detector, the measured efficiency obtained is a rough estimation.

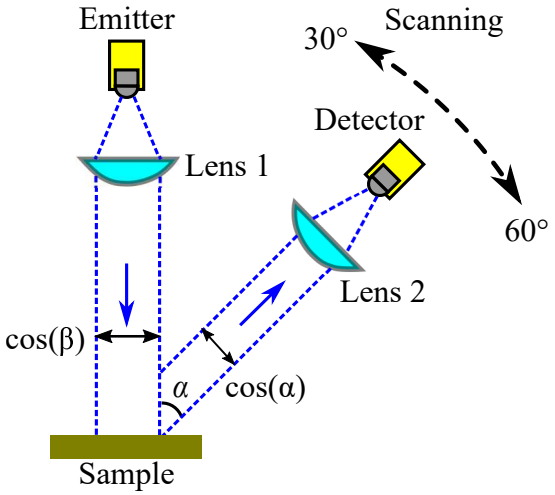

Figure 3.11. Simplified experimental setup. Geometry of the experimental setup with respect to the anamorphic magnification factor.

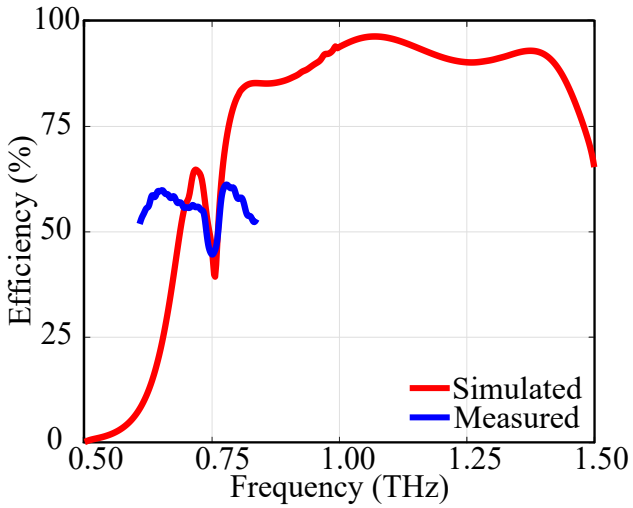

Figure 3.12. Overall efficiency of the designed metasurface. The result is obtained by calculating the total power of the deflected circularly polarised waves at their respective frequencies.

Figure 3.13 shows the resulting polarisation ellipses obtained from the second set of measurements. They are created by averaging the measured amplitude spectra over a 3-dB bandwidth around the specified frequency and normalising to the maximum amplitude among different polarisation angles. It can be seen that the relative amplitude of the deflected waves remains very similar across all polarisation angles. Furthermore, the normalised amplitudes are well above the half-power standard for circular polarisation. We can thus infer that the incoming LHCP and RHCP waves can be split into opposite deflection angles over the entire bandwidth.

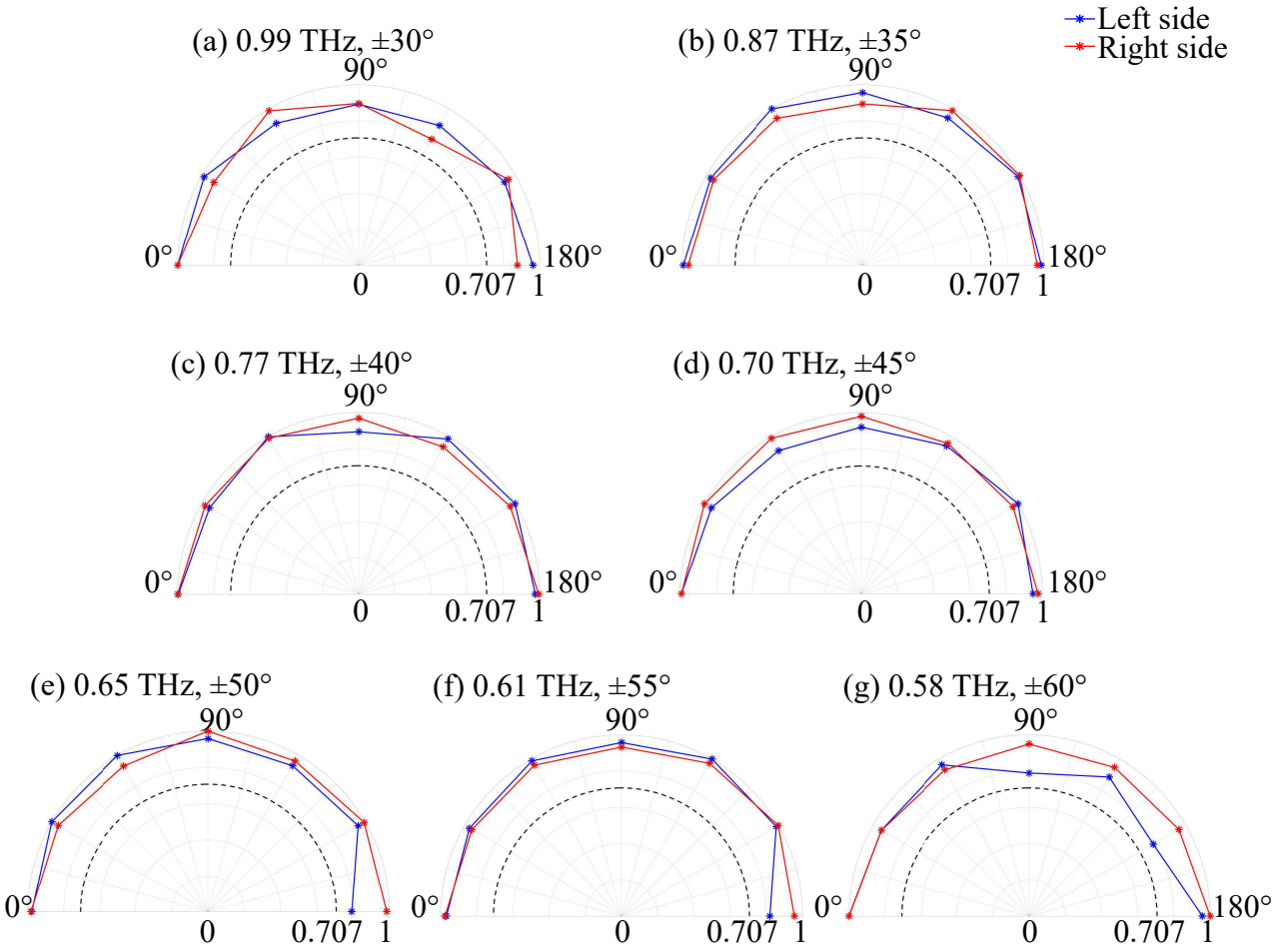

Figure 3.13. Polarisation ellipses of the designed metasurface. Polarisation ellipses with linear amplitude for increasing deflection angle (a)-(g). Each ellipse is normalised to its own maximum. The blue and red lines denote the left and right side of the scan range. Dashed black line mark the half-power threshold for circular polarisation.

3.6 Conclusion

In conclusion, we have demonstrated a broadband reflective circular polarisation beam splitter based on coaxial disk-ring resonators. The obtained measurements confirm that this metasurface is capable of deflecting LHCP and RHCP waves into predesigned angles, with opposite signs on either side of the normal direction. The confirmed angular range of deflection covers $\pm 30^{\circ}$ to $\pm 60^{\circ}$ for LHCP and RHCP waves respectively, corresponding to a frequency range of 1.00 THz to 0.58 THz. Our design has a measurable relative deflection bandwidth of 53%. At 0.78 THz, the measurable efficiency for the designed metasurface is approximately 61%. Theoretically, our design is capable of achieving a bandwidth of 73% which covers a frequency range from 0.70 THz to 1.50 THz with an average efficiency of 85%. Future applications in high-data rate terahertz communications in particular would benefit from polarisation-division multiplexing. In the next Chapter, metasurfaces consisting of dielectric-resonators are employed in place of metallic-resonators for enhanced performance.

Chapter 4

Terahertz near-field imaging of dielectric resonators

AS an alternative to metallic resonators, dielectric resonators can increase the radiation efficiency of metasurfaces at terahertz frequencies. Such subwavelength resonators made from low-loss dielectric materials operate on the basis of oscillating displacement currents. For full control of electromagnetic waves, it is essential that dielectric resonators operate around their resonant modes. Thus, understanding the nature of these resonances is crucial towards design implementation. To this end, an array of silicon resonators on a quartz substrate is designed to operate in transmission at terahertz frequencies. The resonator dimensions are tailored to observe their low-order modes of resonance at 0.58 THz and 0.61 THz. In this Chapter, we employ a terahertz near-field imaging technique to investigate the complex near-fields of this dielectric resonator array. This unique method allows direct experimental observation of the first two fundamental resonances.

4.1 Introduction

Metasurfaces or two-dimensional metamaterials (Zheludev and Kivshar, 2012) consist of miniaturised resonators with subwavelength periodicity, and are capable of manipulating the wavefront of incident waves. The principle of metasurfaces to control the wavefront reconciles with that of reflectarrays (Huang and Encinar, 2008) and transmitarrays (Ryan *et al.*, 2010), well established at microwave frequencies. Conventionally, metallic resonators are employed for shaping wavefronts either through reflection (Yu *et al.*, 2011; Huang and Encinar, 2008) or transmission by using multilayer configurations (Pfeiffer *et al.*, 2014; Pfeiffer and Grbic, 2013). Typically, metallic resonators exhibit decreasing radiation efficiencies with increasing frequencies (Zou *et al.*, 2014). This is due to increasing Ohmic loss at frequencies beyond the microwave regime (Khurgin, 2015). In contrast, metasurfaces made of dielectric resonators have been shown to intrinsically maintain high efficiencies from the microwave to the visible frequency range (Zou *et al.*, 2014, 2013). As dielectric resonators operate based on the oscillation of displacement current at specific resonance frequencies, Ohmic loss is alleviated, and dielectric losses can be minimised through the use of low-loss dielectric materials (Petosa, 2007).

Apart from the superior efficiency as discussed above, dielectric resonators can support magnetic dipole resonances with a single dielectric layer, as opposed to two layers required by their metal counterparts. With proper magnetic and electric resonances, dielectric resonator metasurfaces can exhibit extraordinary phase, amplitude and polarisation control of output waves. As for the phase control, individual resonators can induce a phase discontinuity within the 2π range for shaping the outgoing wavefront in transmission (Staude *et al.*, 2013; Wang *et al.*, 2014; Li *et al.*, 2016) and reflection (Zou *et al.*, 2014, 2013; Liu *et al.*, 2014). A number of components have exploited electric and magnetic resonances in dielectric resonators for different beam shapes, which include holograms (Chong *et al.*, 2015) and optical vortices (Chong *et al.*, 2016). Other research works have demonstrated ways to mechanically tune dielectric resonator arrays as crucial steps towards implementing high performance reconfigurability (Gutruf *et al.*, 2016; Sautter *et al.*, 2015).

In the terahertz frequency regime, high-efficiency components are particularly important as power is generally limited and there is degradation in the signal-to-noise ratio due to free-space path loss and atmospheric absorption. Practical applications for terahertz metasurfaces of subwavelength metallic resonators have been proposed

in sensing (Debus and Bolivar, 2007; Cheng *et al.*, 2014; Chen *et al.*, 2012; Singh *et al.*, 2014), filtering (Ebrahimi *et al.*, 2015) and wavefront manipulation (Niu *et al.*, 2014, 2013, 2015; Cheng *et al.*, 2014; Wang *et al.*, 2015a). Dielectric resonators have the potential to become crucial building blocks in the terahertz frequency region by increasing the efficiency of basic components. Magnetic mirrors and reflectarrays based on dielectric resonators that exploit the properties of magnetic resonances have been realised with high performance (Headland *et al.*, 2016, 2015a). Terahertz dielectric resonators that utilise overlapping magnetic and electric resonances have been designed and show capabilities of extraordinary wavefront manipulation in reflection (Ma *et al.*, 2016).

Most metasurfaces have been characterised by far-field measurements using terahertz time-domain spectroscopy systems (THz-TDS). However, terahertz far-field measurements are lacking the microscopic resolution needed to investigate the properties of samples in the near-field. Importantly, reactive near-fields cannot be observed through far-field measurement. In contrast, terahertz near-field microscopy has been useful in mapping the two-dimensional electromagnetic responses of various samples with spatial resolutions below the diffraction limit (Bitzer *et al.*, 2010; Adam, 2011; Blanchard *et al.*, 2011). Some components characterised by terahertz near-field microscopy include metallic resonators (Wallauer *et al.*, 2011; Bitzer *et al.*, 2009, 2011), metallic subwavelength holes (Bitzer and Walther, 2008) and dielectric microspheres (Mitrofanov *et al.*, 2014). It should be noted that dielectric microspheres, although considered dielectric resonators, were fabricated via a bottom-up approach, where the geometry, size and arrangement can be hardly controllable.

Here in this Chapter, we conduct a near-field measurement to examine the properties of the fundamental electric and magnetic dipole resonances of a dielectric resonator array, fabricated via a top-down approach. Section 4.2 provides details of the design of the terahertz dielectric resonator array while Section 4.3 describes the fabrication process undertaken by our collaborators at RMIT University, Melbourne. This experiment was conducted at the University of Freiburg, Germany, during my visit, and details regarding the experiment set-up used is highlighted in Section 4.4. The measured results for both far-field and near-field studies are found in Section 4.5, followed by a conclusion in Section 4.6. It is crucial to understand these fundamental resonances as they are the basic building blocks towards designing highly efficient metasurfaces.

4.2 Design

A terahertz dielectric resonator array is constructed from periodically arranged silicon cylinders on a quartz substrate. The cylindrical shape of the resonator is chosen mainly because of its isotropy. High-resistivity float-zone silicon is chosen as the dielectric material as it has moderate relative permittivity $\varepsilon_r = 11.68$ and negligible loss (Dai *et al.*, 2004). The substrate is quartz with thickness of 500 μm and relative permittivity $\varepsilon_r = 3.8$ with loss tangent $\tan\delta = 0.01$ Grischkowsky *et al.* (1990). The resonator height of 82 μm and the radius of 105 μm are selected to exhibit electric and magnetic dipole resonances centered around 0.60 THz. As dielectric resonators operate based on oscillation of displacement currents, the size of the resonator dictates the field confinement within the boundary. Consequently, the resonance frequency of the dielectric resonator is dependent on the size of the resonator. For example, a larger size results in a lower resonance frequency. The unit cell of the dielectric resonator array is 245 μm which is explicitly chosen to be less than half the operating wavelength (λ = 500 μm) to avoid diffraction.

Numerical computations are performed using CST Microwave Studio with unit cell boundary conditions. The structure is illuminated with a y-polarised plane wave at normal incidence. We can classify the electric and magnetic dipole resonance modes by examining their electric and magnetic fields, as revealed by cross-sectional views in Fig. 4.1. The electric dipole resonance in Fig. 4.1(a) shows an electric field that is oscillating in the direction of the incident wave's polarisation ($\mathbf{E}_y$). Magnetic dipole resonances in Fig. 4.1(b) can be identified with a circulating electric field around the center of the resonator. We can further confirm the positions of the electric dipole resonance and the magnetic dipole resonance by examining Fig. 4.2. The simulated reflection phase curve exhibits a π radian crossing at 0.58 THz, which is the location of the electric dipole resonance and a zero crossing at 0.61 THz, which is the location of the magnetic dipole resonance. This is in line with the expected π phase difference between electric and magnetic dipole resonances (Liu *et al.*, 2014).

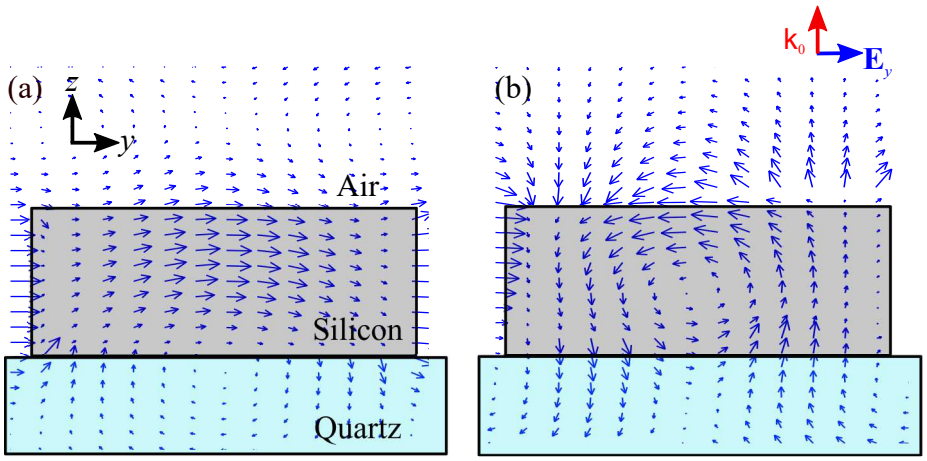

Figure 4.1. Cross-sectional view of a single dielectric resonator. The instantaneous electric fields are represented by blue arrows. (a) Electric dipole resonance and (b) magnetic dipole resonance.

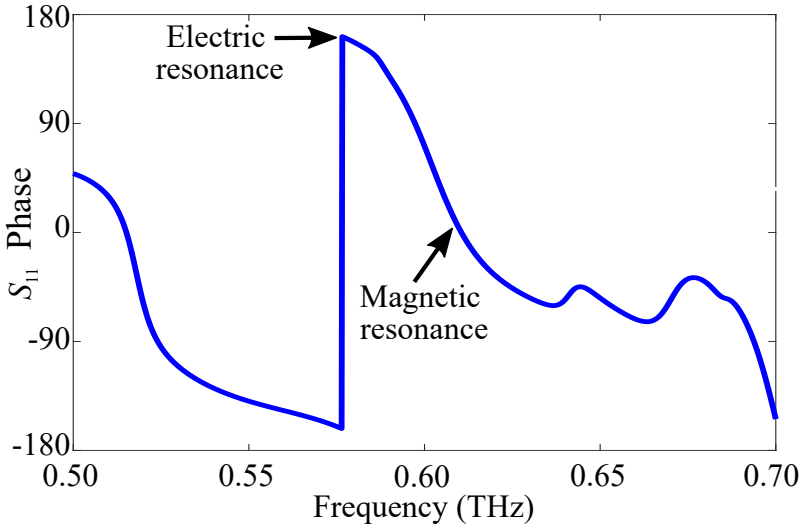

Figure 4.2. Reflection phase response of the dielectric resonator array. The labels indicate the positions of the electric dipole resonance and the magnetic dipole resonance.

4.3 Fabrication

For this structure, micro-fabrication approach involves a combination of SU-8 assisted bonding, photolithography, and deep reactive ion etching (DRIE). To begin with, a thin adhesion layer of SU-8 is spin-coated on a 3-inch quartz wafer. A 125 µm thick, high-resistivity silicon wafer is then bonded to the substrate by passing it through a laminator at 100 °C at slow speed. The bonded silicon is thinned down as per the design requirements by plasma-enhanced DRIE (Oxford PlasmaPro 100 Estrelas). Finally, the silicon layer is patterned with thick photoresist (AZ4562) and subsequently etched down with the Bosch silicon etching process to realise an array of cylinders. It should be noted that, considering the low thermal conductivity of quartz, the aforementioned etching steps are performed at -5°C. Fabricated structures are imaged using scanning electron microscopy (FEI Verios SEM). False-colour and optical profiler images of the fabricated dielectric resonator array are shown in Fig. 4.3 and in Fig. 4.4 respectively. These images are representative of the impeccable quality and high detail accuracy of the fabricated samples.

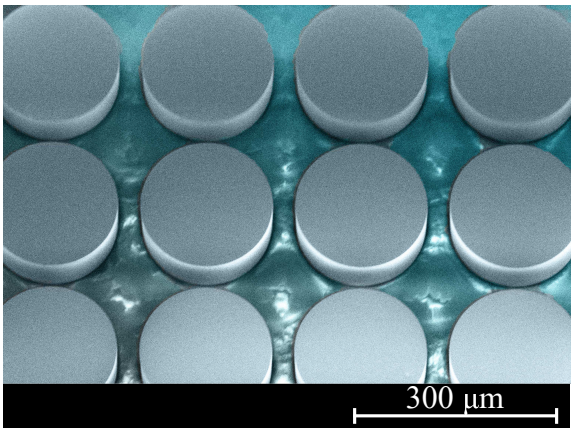

Figure 4.3. Scanning electron micrograph of the dielectric resonator array. A portion of the fabricated silicon resonator array is shown here.

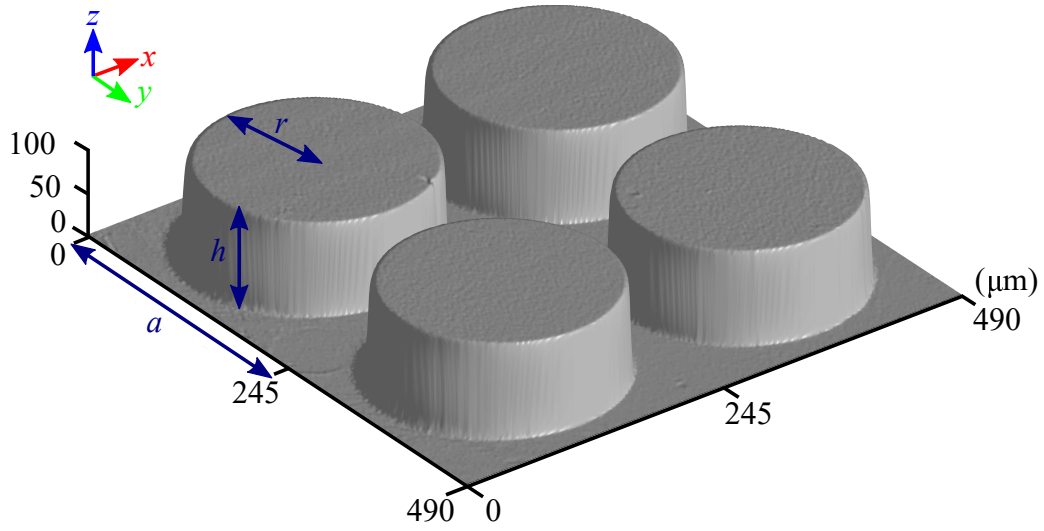

Figure 4.4. Optical profiler image of the fabricated silicon resonators. The dimensions are as follows: the unit cell size $a = 245$ μm, the resonator height $h = 82$ μm, and the resonator radius $r = 105$ μm.

4.4 Measurement

Typically, free space electro-optic sampling is used for far-field terahertz spectroscopy. In order to detect terahertz waves using the electro-optic sampling method, Pockels effect is utilised. This effect refers to a change in the birefringence of the electro-optic crystal in the presence of an electric field. Consequently, the transient electric field induced by the terahertz pulse causes a polarisation change in the laser probe pulse through phase retardation of the two orthogonal components. The arrangement for a free-space electro-optic sampling system that operates in reflection mode is shown in Fig. 4.5(a).

In the absence of a terahertz pulse, the laser probe pulse travels through the electro-optic crystal without observing any phase retardation. As shown in Fig. 4.5(b), a linearly polarised laser beam remains linear as is passes through the electro-optic crystal, which is ZnTe in this case. As the laser pulse passes through the quarter-wave plate at 45° incidence, one of its orthogonal components will be retarded by 90° with respect to the other, resulting in a circularly polarised beam output. The Wollaston prism then splits the two orthogonal components of the laser pulse. At the balanced photodiodes, the difference in intensities of both beams are measured. In this case, both beams will have the same intensity.

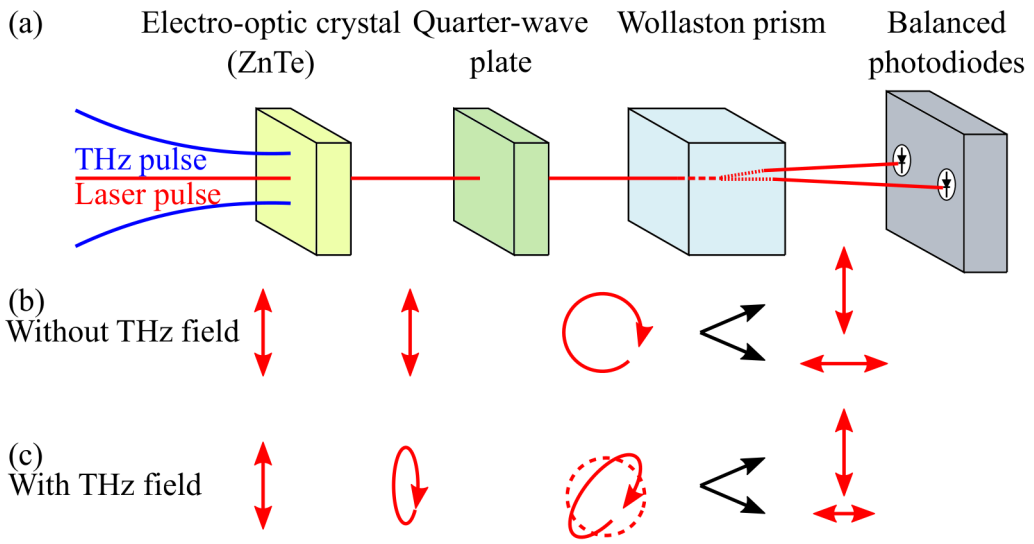

Figure 4.5. Electro-optic sampling system in transmission mode. (a) The red line indicates the laser pulse while the blue line indicates the terahertz pulse which co-propagates through the system. Polarisation states of the laser pulse when it is (b) without the presence of a terahertz electric field and (c) with the presence of a terahertz electric field.

However, with the presence of a terahertz pulse, the laser pulse experiences a phase retardation inside the crystal. At the quarter-wave plate, one of its orthogonal components will be retarded by 90° with respect to the other. As there is an earlier phase retardation experienced by the laser pulse, the polarisation state of the laser pulse is now elliptical. The change in polarisation states can be observed in Fig. 4.5 (c). Once again, the Wollaston prism splits the two orthogonal components of the laser pulse. Finally, as the resultant polarisation is elliptical, there will be a difference in intensity between the two beams. This difference correlates to the amount of phase shift experienced by the laser pulse at the electro-optic crystal and thus the amplitude of the terahertz pulse.

In order to measure the near-fields of a sample, we utilise the electro-optic sampling system in reflection mode as shown in Fig. 4.6(a). Here, the laser probe passes through a beam splitter where a portion of the signal travels to the sample. Similar to its transmission mode counterpart, the terahertz pulse will affect the polarisation of the laser pulse due to Pockels effect. The returning laser pulse propagates through the beam splitter and travels to the quarter-wave plate, the Wollaston prism and the balanced photodiodes. The electro-optic crystal is coated with a high-reflection (HR) coating of 800 nm thickness to increase the intensity of the reflected laser pulse. It is noteworthy

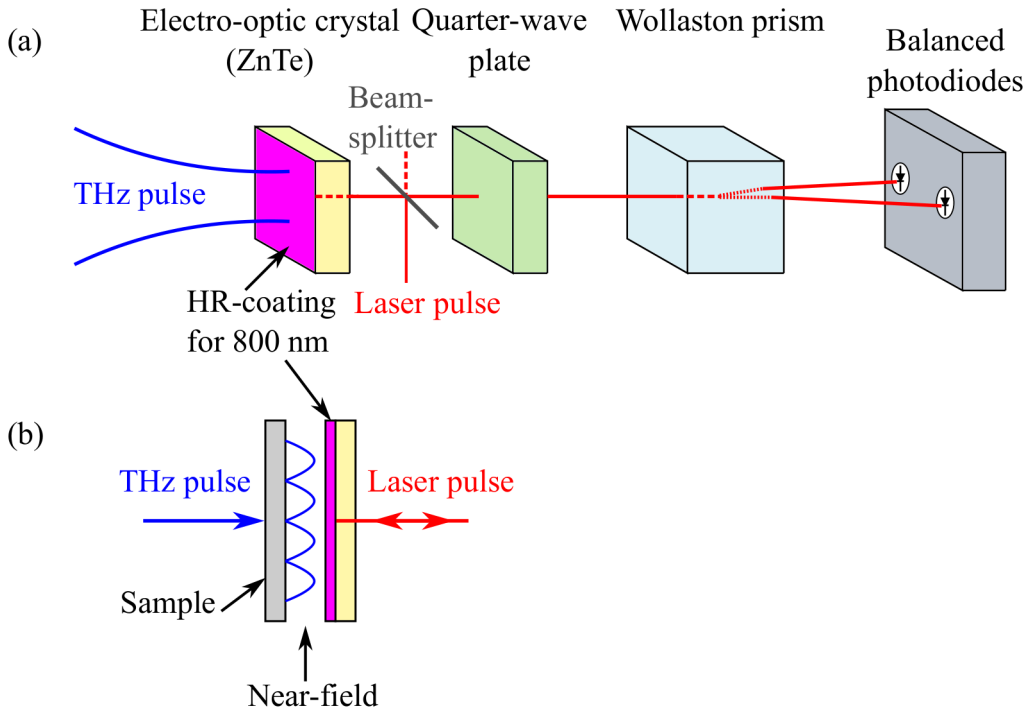

Figure 4.6. Electro-optic sampling system in reflection mode. (a) The red line indicates the laser pulse while the blue line indicates the terahertz pulse which propagates through the system. (b) Near-field measurement of a sample when the system is in reflection mode.

to mention that the terahertz pulse is not influenced by the HR-coating. The near-fields of the sample can then be measured as illustrated in Fig. 4.6(b).

As shown in Fig. 4.7, the near-field experiment setup is based on a typical THz-TDS system, with a major difference being that the electro-optic crystal is placed very close to the sample to collect reactive fields emerging from the sample and is operating in reflection mode. In order to measure the longitudinal electric fields, E_z, we used an electro-optic crystal in the (100) orientation. The dielectric resonator array is illuminated from the back of the substrate with a y-polarised focused Gaussian beam with a spot diameter of 500 µm. The E_z field measurement is taken approximately 100 µm ($\lambda_0/5$) above the dielectric resonator array to minimise electric field disturbance. It is also possible to measure the transverse components, E_x and E_y using electro-optic crystals of the (110) orientation (Zhu and Nahata, 2007). However, measurements of the transverse components (E_x and E_y) are not utilised in this work, since local evanescent transverse components outside the dielectric resonators are relatively weak. This weak field is obscured by the propagating terahertz waves that co-propagate with the probe beam throughout the crystal length. It is noteworthy that in metallic subwavelength apertures

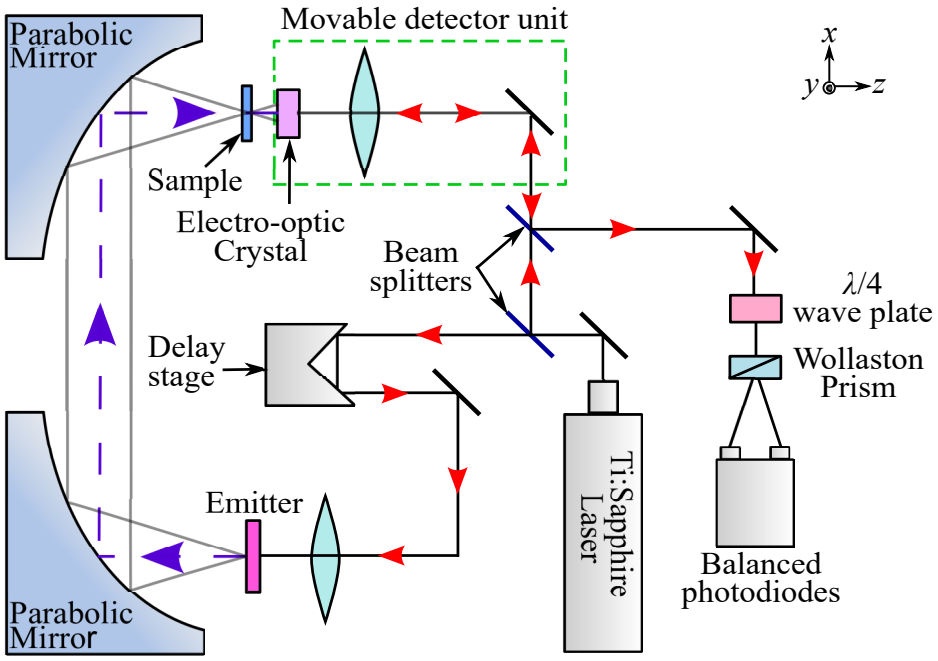

Figure 4.7. Near-field THz-TDS experimental set up. The purple arrows represent the THz pulses and the red arrows indicate the infrared laser beam paths.

(Knab *et al.*, 2009) and planar metamaterials (Bitzer *et al.*, 2009), it is possible to measure all three components of the electric field, owing to their exposed strong localised field. The employed near-field system can measure the electric field in one spot at a time with a spot diameter of 10 µm which is defined by the probe laser. A 2D raster scan is performed by moving the electro-optic crystal together with the laser beam with translation stages. The longitudinal (z-directed) electric fields hence is mapped over the xy plane with a spatial resolution of 20 µm.

A complete set of measurements for each near-field spot consists of a total electric field measurement of the E_z component, $E_{z,t}$, in the presence of the sample, and a reference or incident electric field measurement $E_{z,r}$, measured with a bare quartz substrate replacing the sample. To obtain the scattered electric field, $E_{z,s}$, which is the electric field due to interaction with the resonator solely, we subtract the reference electric field from the total electric field in the frequency domain. From data analysis a slight temporal shift is observed between the reference and sample measurements. To mitigate the effect of this shift, a phase offset ($\Delta\phi$) can be added to the reference measurement:

$$E_{z,s}\angle\phi_{z,s} = E_{z,t}\angle\phi_{z,t} - E_{z,r}\angle(\phi_{z,r} + \Delta\phi). \tag{4.1}$$

A slight spatial misalignment of the measured results is also observed in the xy dimensions. This can be straightforwardly compensated by shifting the alignment between the sample and reference data.

4.5 Results

4.5.1 Far-field analysis and results

A standard THz-TDS system is used for far-field measurements. A focused beam with a spot size of 5 mm illuminates the sample from the substrate side to excite approximately 300 dielectric resonators. A blank quartz substrate of the same thickness (500 μm) is used as a reference. All the measurements are conducted in a nitrogen-purged atmosphere to mitigate the water vapour absorption. Fourier transform is applied to the time-resolved data to obtain the complex frequency response of the sample with a spectral resolution of 5 GHz. The transmission amplitude is shown in Fig. 4.8. From the normalised spectrum, we can observe the dips at 0.58 THz and 0.61 THz which correspond to the electric dipole resonance and magnetic dipole resonance respectively. The strength and position of these resonances differ slightly from the results obtained from numerical simulation with CST Microwave Studio. This could be due to the realised focused beam as opposed to numerical plane-wave approximation (Peiponen *et al.*, 2012). Apart from that, higher-order modes can also be observed at higher frequencies in both the simulation and measurement.

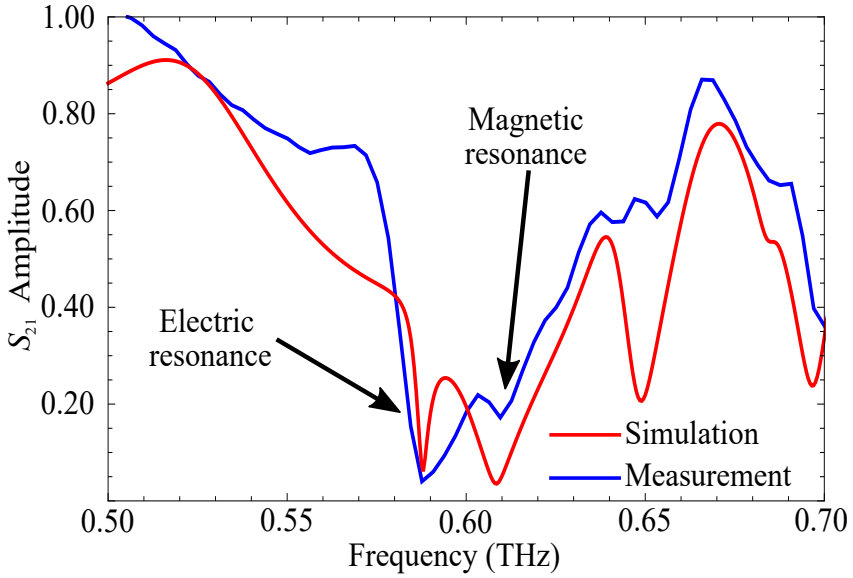

Figure 4.8. Normalised transmission spectra of the dielectric resonator array. The red and blue lines refer to simulated and measured results respectively. The positions of the electric and magnetic resonances are indicated by arrows.

4.5.2 Near-field analysis and results

As a comparison, we simulate the dielectric resonator array with CST Microwave Studio, with a 100 μm air gap space between electro-optic crystal ($\varepsilon_r = 2.25$) and sample to match experimental conditions. The measured and simulated instantaneous electric fields for both electric and magnetic dipole resonances are shown in Fig. 4.9. The fields are at the moment when the oscillation reaches their maximum amplitude and are also normalised to the maximum amplitude of the electric fields for the simulated magnetic dipole resonance. The measured near-field images show horizontal variations in amplitude which are due to the focused beam used during measurement. From the simulations, we can observe that the E_z field for the magnetic resonance is stronger than the electric resonance. As both simulated and measured plots are normalised to the same scale, the same observation is confirmed in the measured results. This relatively strong E_z field is due to the out-of-the-plane circulation of the electric field for the magnetic resonance.

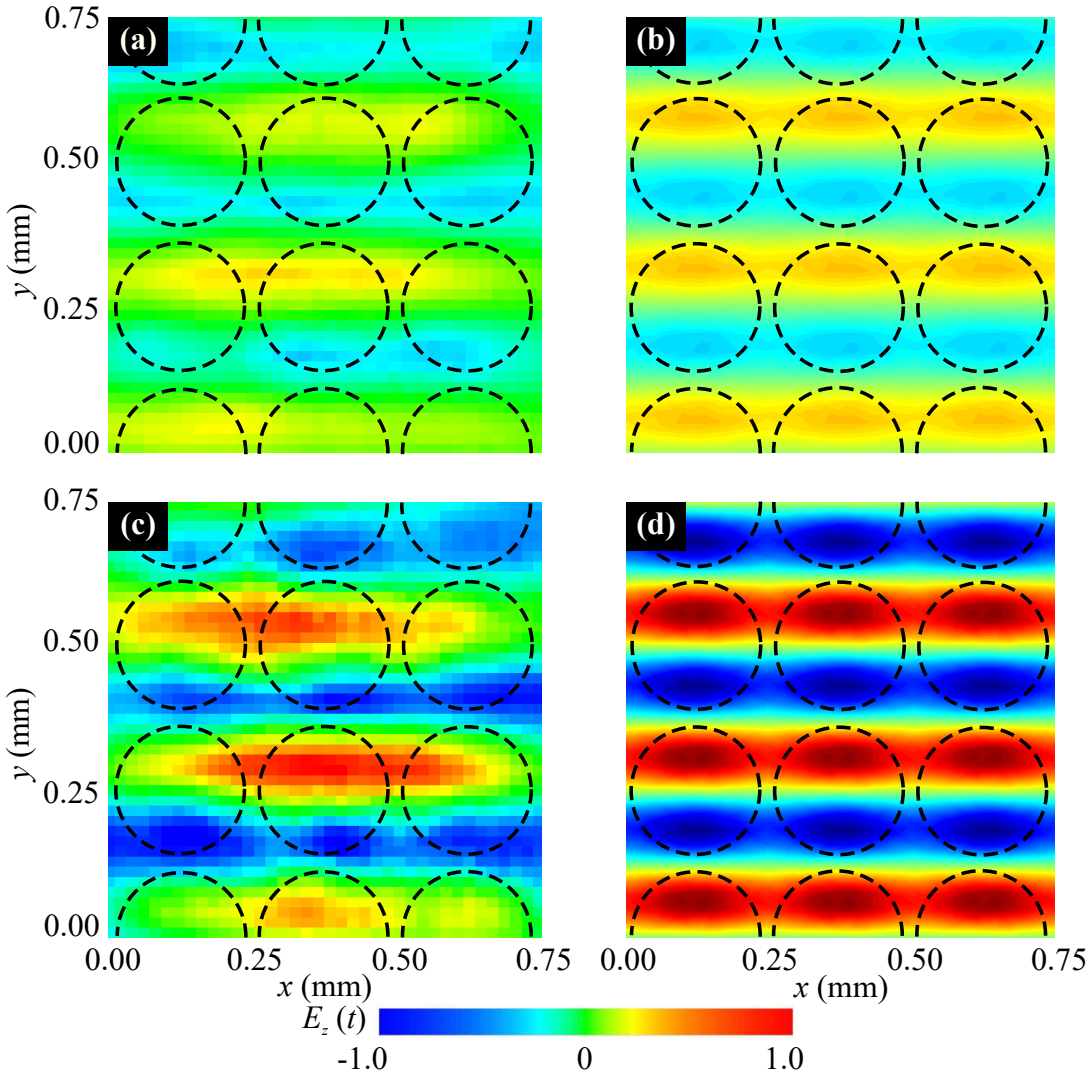

Figure 4.9. Instantaneous E_z field above the dielectric resonator array in linear scale. The circles portray the location of the dielectric resonators. The measured (a) and simulated fields (b) at 0.58 THz illustrate an electric dipole resonance. The measured (c) and simulated fields (d) at 0.61 THz illustrate a magnetic dipole resonance.

4.6 Conclusion

In conclusion, we have designed and experimentally validated an array of terahertz dielectric resonators operating in transmission at terahertz frequencies. As the resonant electric fields are solely confined within the dielectric resonators themselves, these fields are not readily accessible via near-field probe. This is in contrast to metallic resonators where resonant electric fields are not confined within the structure facilitating access to near-field transverse electric field components. Nevertheless, we have investigated dielectric resonator structures with both far-field spectroscopy and near-field spectroscopy. We achieved good agreement between our measured and simulated results for both the far-field and near-field measurements. With near-field THz-TDS techniques, we confirm the presence of the predicted fundamental electric resonance mode at 0.58 THz and the magnetic resonance mode at 0.61 THz. Electromagnetic interactions between the resonators observed in the near-field provides information that cannot be obtained in the far-field which is useful for potential future applications of metasurfaces. The work in this Chapter provides insight towards designing dielectric resonator based metasurfaces. In the next Chapters, similar dielectric resonators will be used to implement broadband quarter-wave and half-wave mirrors.

Chapter 5

Broadband quarter-wave mirror at terahertz frequencies

POLARISATION conversion of terahertz waves is important for applications in imaging and communications. Conventional wave plates used for polarisation conversion are inherently bulky, lossy and operate at discrete wavelengths. As a substitute, we employ reflective metasurfaces composed of subwavelength resonators to obtain similar functionality but with enhanced performance. More specifically, we substitute commonly used planar metallic resonators with low-order dielectric resonators to achieve high radiation efficiencies. As a demonstration of the concept, we present a quarter-wave mirror that converts 45° incident linearly polarised waves into circularly polarised waves. This metasurface operates with high efficiency over a measurable relative bandwidth of 49% in the frequency range of 0.97 THz – 1.60 THz. This broadband and high efficiency capabilities of our metasurfaces will allow to leverage maximum benefits from a vast terahertz bandwidth.

5.1 Introduction

Polarisation conversion is typically achieved by using wave plates made of birefringent materials. Specifically, as the wave propagates through such a material, orthogonal field components experience different refractive indices and thus different phase delays. A desired phase difference between the field components can be obtained by adjusting the material thickness. In the terahertz region, there is however a scarcity of naturally available birefringent materials with low absorption.

Stacked crystalline quarter-wave plates (Chen *et al.*, 2013; Masson and Gallot, 2006) could overcome narrow bandwidth limitations, but with trade-offs in substantial device thickness and high cost. Additionally, the maximum measured transmission power for a stacked quarter-wave plate is merely 55% (Masson and Gallot, 2006). In order to overcome these limitations, periodic structures such as reflectarrays (Niu *et al.*, 2014, 2015; Huang and Encinar, 2008), gratings (Lopez and Craighead, 1998; Nordin and Deguzman, 1999; Tyan *et al.*, 1996) and multilayered structures (Lopez and Craighead, 1998; Yu *et al.*, 2006; Tyan *et al.*, 1996; Suzuki *et al.*, 2016b; Han *et al.*, 2017) can be employed to provide designable birefringence.

One alternative towards providing engineered birefringence at terahertz frequencies is to utilise metasurfaces. Metasurfaces, which are two-dimensional variants of metamaterials, open perspectives for novel devices due to their tailorable exotic properties not commonly found in nature (Withayachumnankul and Abbott, 2009; Zheludev and Kivshar, 2012). In principle, metasurfaces consist of periodically arranged subwavelength resonators that collectively yield controlled amplitude and phase responses. Through metasurface designs, fundamental properties of electromagnetic waves can be controlled, including phase, amplitude and polarisation. A majority of previously proposed metasurfaces were made of metallic resonators, and demonstrated various functions including filters (Ebrahimi *et al.*, 2015), sensors (Singh *et al.*, 2014; Withayachumnankul *et al.*, 2012), absorbers (Cheng *et al.*, 2015; Withayachumnankul *et al.*, 2014), modulators (Heyes *et al.*, 2014), polarisation beam splitters (Lee *et al.*, 2018b; Niu *et al.*, 2014) and beamformers (Niu *et al.*, 2013, 2015; Yu *et al.*, 2011).

Metasurfaces can contain resonators with a birefringence response that directly benefit quarter- and half-wave plates. Quarter-wave plates introduce a $\pi/2$ phase difference between the two orthogonal electric field components of an incident wave, while the amplitude responses are equal. This allows conversion between linearly polarised waves and circularly polarised waves. Several examples of planar quarter-wave plates

made up of metallic resonators were demonstrated at terahertz frequencies (Weis *et al.*, 2009; Imhof and Zengerle, 2007; Wang *et al.*, 2015a; Strikwerda *et al.*, 2009). However, metallic resonators impose ohmic loss due to increased dissipation of electric energy in metals at higher frequencies. Additionally, many metallic-based designs require a spacer made of dielectrics causing further dissipation. It is worth mentioning that periodic, elliptical air holes which causes anisotropy in dielectric material have also been shown to be efficient wave plates in the terahertz region (Zi *et al.*, 2018). A variant of wave plates that function in reflection instead of transmission are known as birefringent mirrors. For instance, quarter-wave plates operate in transmission mode while birefringent quarter-wave mirrors have the same functionality but operate in reflection mode. At terahertz frequencies metallic resonators have been used to demonstrate broadband quarter-wave mirrors (Ma *et al.*, 2017).

A potential solution to overcome low radiation efficiencies of metallic resonators at higher frequencies is to incorporate dielectric resonators in metasurfaces. As the operation of dielectric resonators is based on resonant oscillations of displacement current, this alleviates Ohmic loss that metallic resonators suffer from. It has been demonstrated that dielectric-resonator-based metasurfaces are able to maintain high efficiencies across the microwave to visible frequency band (Zou *et al.*, 2013, 2014). Furthermore, dielectric resonators are capable of supporting magnetic dipole resonances within a single dielectric layer as opposed to two layers as required by their metallic counterparts, as demonstrated in Chapter 4 (Lee *et al.*, 2017). It implies that a dielectric spacer is not required for dielectric resonators, and thus dissipation loss can be further reduced. At terahertz frequencies, magnetic mirrors and reflectarrays based on dielectric resonators have been realised with high performance (Headland *et al.*, 2016, 2015a). It is also noteworthy that dielectric resonators exhibit a smoother phase variation as compared to their metallic counterparts as mentioned in Section 2.4. The phase gradient as a function of the frequency is dependent on the radiation quality factor of the resonators, Q_r, where a higher value would result in a larger phase gradient. The lower Q_r and thus smoother phase gradient of the dielectric resonators is due to their higher radiation loss or better coupling with free-space waves (Qu *et al.*, 2015). This feature benefits the polarisation conversion purity of resulting waveplates and mirrors.

In this Chapter, we present the design, fabrication and characterisation of broadband quarter-wave mirror at terahertz frequencies. We employ dielectric resonators as building blocks of these mirrors in order to achieve high efficiency. This metasurface operates

in reflection mode for a 45° incident angle. The geometry of these resonators is tailored for an ultra-wide operation bandwidth. Future applications in terahertz polarimetric devices and terahertz spectroscopy would benefit from these broadband planar metasurfaces.

5.2 Design

Figure 5.1 shows the unit cell design for the quarter-wave mirror. The resonators are made of instrinsic float-zone silicon of thickness 50 μm. This type of silicon has a moderate relative permittivity $\varepsilon_r = 11.68$ and negligible loss with a loss tangent of $\tan\delta = 0.0007$ (Dai *et al.*, 2004) at terahertz frequencies. Initially, the resonator was designed to be cross-shaped where the cross-arms were of different lengths. This cross geometry would resonate at different frequencies for the two orthogonal polarisations, thus leading to different phase responses. However, since curved edges are more compatible with micro-fabrication than sharp internal angles, the design was modified to incorporate sinusoidal sides. In order to avoid grating lobes, the largest dimension of the unit cell is chosen to be $l_{q1} = 70$ μm, which is less than half of the shortest operating wavelength of 171 μm at 1.75 THz. The ground plane of this metasurface is a gold layer with a thickness of 200 nm which is significantly above the skin depth at the frequency range of interest (≈56 nm at 0.95 THz).

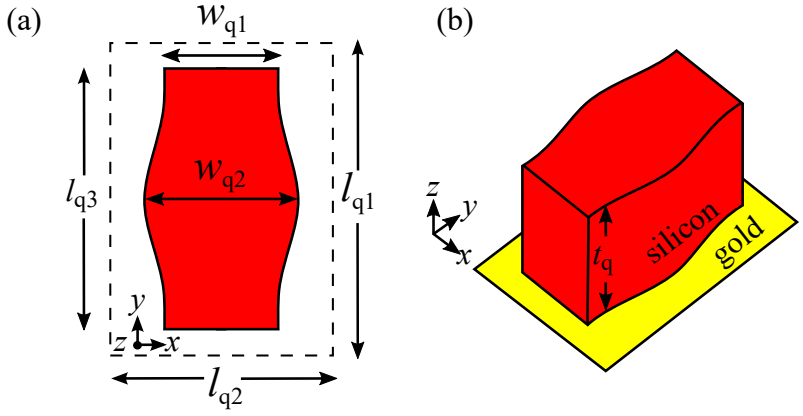

Figure 5.1. Unit cell design of the quarter-wave mirror. Unit cell design of the quarter-wave mirror. (a) Top view and (b) 3D schematic of the unit cell. The side walls of the resonator are defined by a sine function with its peak and trough aligned with w_{q2} and w_{q1}, respectively. The dimensions are as follow: $l_{q1} = 70$ μm, $l_{q2} = 50$ μm, $l_{q3} = 56$ μm, $w_{q1} = 25$ μm, $w_{q2} = 33$ μm, $t_q = 50$ μm.

This structure is simulated using the frequency-domain solver in CST Microwave Studio with unit cell boundary conditions applied to the lateral boundaries. Floquet port excitations of either x- or y-polarised waves are used. The surface impedance accounting for metal loss in gold is used to model the thin gold metal layer in this simulation (Niu *et al.*, 2013). In order to recover the phase response induced solely by the resonator, the port is de-embedded to the ground plane. For functional broadband quarter-wave mirrors, the phase difference between the x- and y-polarised electric field components in reflection is designed to be near $\pi/2$ radian across the frequency band of interest. The mechanism behind this feature will be detailed in Section 5.5.

5.3 Fabrication

A section of the fabricated metasurface is shown in Fig. 5.2. The mirror is composed of silicon resonators attached to a gold ground plane on a silicon substrate. Thus, the mirror requires two silicon wafers, a four inch double-polished <100> float-zone (FZ) silicon wafer of thickness 125±25 µm and resistivity >5 kΩ-cm, and a three inch standard Si wafer. A 50 mm × 50 mm square section is diced (Dicing saw-DISCO DAD 321-NanoFab) out of the four inch silicon wafer. Both wafers are then cleaned with acetone, isopropyl alcohol (IPA) and H_2O, consecutively, for a minute, blow-dried with N_2 gun and dehydrated at 120°C for more than 5 minutes. In this work, the used method of bonding does not involve an SU_8 adhesion layer, contrary to our previous works (Headland *et al.*, 2016, 2015a).

A gold-to-gold eutectic bonding is adopted to ensure high bonding strength that will be less affected by temperature changes. In this procedure, a 200 nm gold film with a 20 nm Cr adhesion layer is deposited on both wafers inside an electron beam evaporation chamber (PVD75, Kurt J. Lesker) at 0.5 As^{-1}, 4 $<10^{-7}$ Torr and at room temperature. After deposition, the 50 mm × 50 mm wafer is immediately placed onto the 3-inch silicon wafer using the gold-coated faces. Bonding is performed with the help of a wafer bonder (SB6 SUSS Microtech) at gold eutectic conditions. No special pre-treatment steps are required prior to bonding. Parameters such as the bonding force, bonding temperature, heating/cooling rate and pressure of chamber are sorted. For good bonding, the chamber is pumped down to a base pressure of $<5.0\times10^{-5}$ mbar and the temperature ramped up to 400 °C at 5 °C/min. Eutectic bonding commences at 300 °C with an applied force of 2260 N including a 20 min dwelling time. The sample

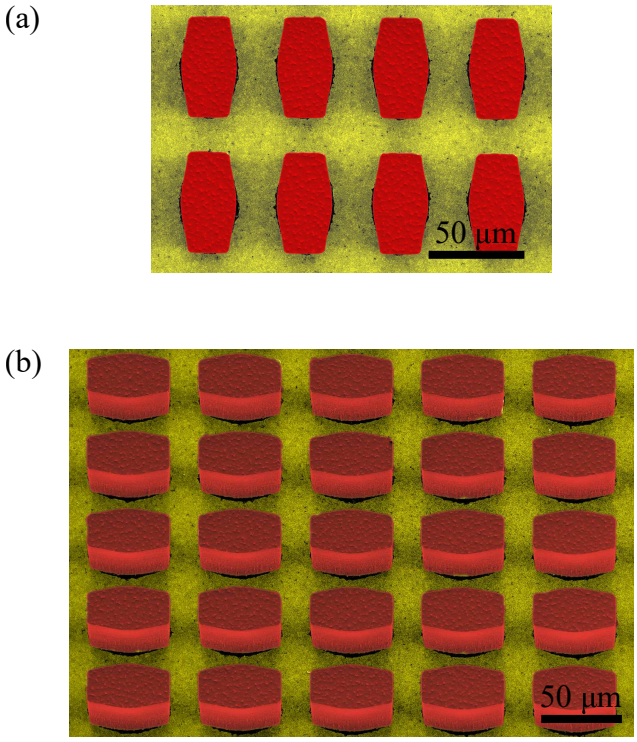

Figure 5.2. False coloured scanning electron micrographs of the quarter-wave mirror. False colour scanning electron micrographs showing a section of the fabricated quarter-wave mirror from (a) top view and (b) isometric view.

is then left to cool slowly to room temperature. The bonded sample is then properly cleaned and dehydrated with standard microfabrication cleaning steps. Hereinafter, the fabrication procedure is detailed in our previous work (Headland *et al.*, 2016). The float-zone silicon wafer of the bonded ensemble undergoes a thinning process to a height equal to that of the desired resonator, using a plasma-enhanced deep reactive ion etching. This is followed by patterning using standard photo-lithographic steps and subsequent silicon etching to the gold layer to realise desired resonators.

5.4 Measurement

A fiber-coupled terahertz time-domain spectroscopy is used in the experiment validation. The set-up used for the quarter-wave mirror is shown in Fig. 5.3. In these measurements, lenses with a focal length of 5 cm are used for beam collimation and focusing. Wire-grid polarisers are employed to ensure polarisation purity. A focused, either vertically- or horizontally-polarised beam illuminates the sample at 45° incidence. The sample then reflects the incident beam into the lenses which focuses the beam into the linearly polarised detector, which can be rotated for either vertically- or horizontally-polarised waves. For a Gaussian beam of waist of 1 mm, the corresponding Rayleigh range is 10 mm at a wavelength of 300 µm. As the focused Gaussian beam impinging on the sample is around the location of the beam waist, the beam can be assumed as having negligible angular divergence.

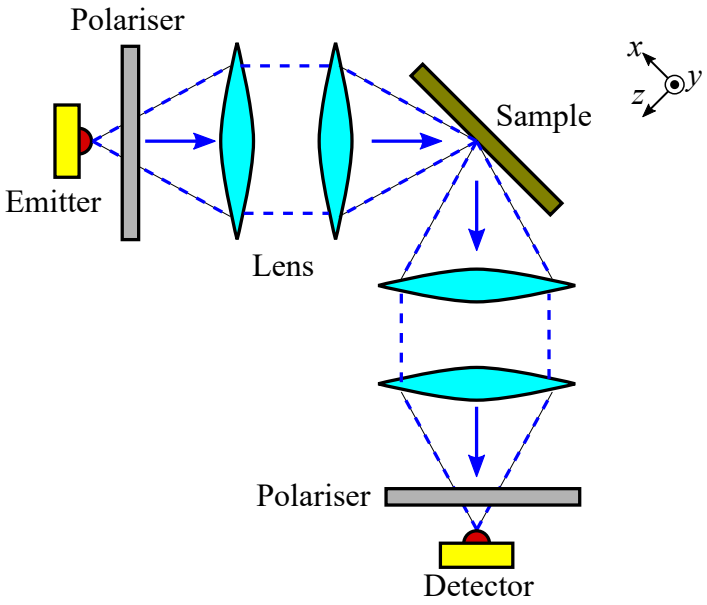

Figure 5.3. Schematic of the 45° incident set-up. Schematic of the experiment set-up. It is worth mentioning that the focused beam in this image is exaggerated. In reality, the beam has a longer Rayleigh length.

5.5 Results

The amplitude and phase response of the vertically and horizontally polarised waves are evaluated. First, the sample is excited with vertically polarised waves (y-polarised) at 45° incidence in the xz plane and the detector measures the outgoing vertically polarised waves at the specular reflection angle. This set of measurement is then repeated for horizontally polarised (x-polarised) waves. For normalisation of all measurements, a gold mirror is used in place of the sample.

The reflection phase responses of this metasurface for both polarisations are shown in Fig. 5.4(a) and the phase difference between the two orthogonal polarisations is shown in Fig. 5.4(b). The aforementioned results have been deembedded to the ground plane, so that the phase profile does not account for propagation in free space. It can be seen that the measured and simulated results are in good agreement with each other. A slight discrepancy in the phase results can be attributed to small misalignment of the gold mirror to obtain phase measurements in THz-TDS. As the detector is rotated to measure the orthogonal component of the terahertz wave, a slight error in phase and amplitude measurement also occurs. The phase profile for the measured results has been offset to match the simulation results to compensate a phase shift due to these misalignments. This phase offset is possible given the notable features in the sample phase profile. In order to illustrate the zero crossings that correspond to frequencies of resonance, the reflection phase response shown in the results are wrapped.

The phase response for the vertically polarised component approaches the zero crossing first, indicating that its fundamental resonance mode is at the lowest frequency. This is because of the larger size of the resonator in the y-dimension. The fundamental mode excited at the first resonance is a magnetic dipole aligned with the x-axis. This mode of resonance corresponds to an electric field that loops within the resonator as shown in Fig. 5.5(a). Next, the horizontally polarised component approaches its resonance at a higher frequency of around 1.7 THz. For this second resonance, as shown in Fig. 5.5(b), the fundamental mode excited is a magnetic dipole, where a circulating electric field in the resonator is again clearly identified. As shown in Fig. 5.5(b), these two resonances allow for a continuous near $\pi/2$ phase difference between the two orthogonal polarisations from 0.97 – 1.60 THz. The simulated results shown in Fig. 5.4 indicate that the metasurface should be functional up to 1.75 THz. However, due to system limitations, experimental results beyond 1.60 THz are unreliable. As the experiment set-up was done for oblique measurements, the dynamic range for vertical

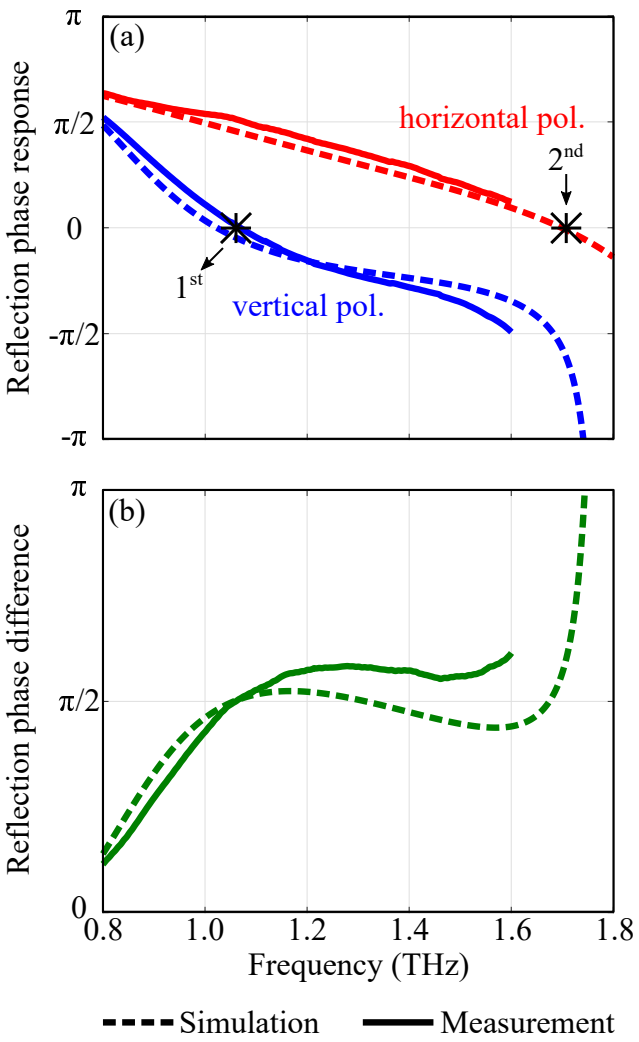

Figure 5.4. Reflection phase profiles of the quarter-wave mirror. Reflection phase profiles of the quarter-wave mirror. The reflection phase responses for the orthogonal polarisations are shown in (a) and their corresponding phase difference is shown in (b). The markers indicate the resonance modes in the quarter-wave mirror.

and horizontal measurements are reduced. Thus, the maximum frequency before the amplitude reaches the noise floor is approximately 1.6 THz.

The measured reflection amplitudes for both polarizations are shown in Fig. 5.6. It can be seen that the metasurface is highly efficient, with measured average reflected amplitudes above 92% for the operating frequencies of 0.97 – 1.60 THz. The simulated reflection amplitudes are significantly higher than the measured results. This difference in amplitude can be attributed to tolerances in alignment, which results in apparent energy loss in the experiments. An existing terahertz quarter-wave mirror by Ma *et al.* (Ma *et al.*, 2017) consisting of metallic resonators showed measured average reflected

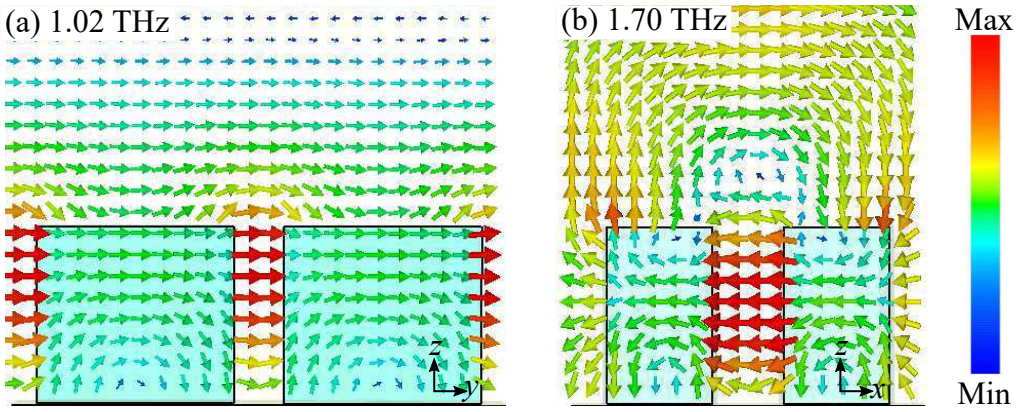

Figure 5.5. Electric field distributions of the dielectric resonators in the quarter-wave mirror on resonance for (a) the y-polarisation at 1.02 THz and (b) for the x-polarisation at 1.70 THz where the wave is 45° incident in the xz plane.

amplitudes of around 89% for the horizontal component and 74% for the vertical component at operating frequencies of 0.4 – 1.05 THz, corresponding to a bandwidth of 88%. Our design achieved markedly higher measured reflection amplitudes of greater than 92% for both orthogonal polarizations despite having a narrower bandwidth of 52% as compared to the 88% bandwidth achieved by Ma *et al.* Therefore, dielectric resonators are shown to have the potential to increase radiation efficiency as compared to their metallic counterparts.

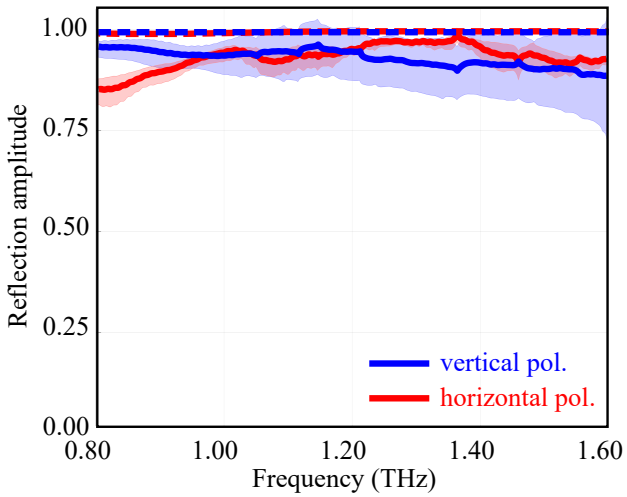

Figure 5.6. Reflection amplitude response of the quarter-wave mirror. Reflection amplitude profiles of the quarter-wave mirror. The dashed lines indicate the simulated results while the solid lines indicate the measured results. Error ranges due to experimental tolerances are indicated with shaded regions.

The results suggest that the incident wave with its linear polarisation at 45° can be converted into a circularly polarised wave upon reflection. In order to confirm that the reflected wave is circularly polarised, we calculate the axial ratio (AR) of its polarisation ellipse. The AR is defined as ratio of the major axis to the minor axis of the ellipse (Balanis, 1982), according to:

$$\mathrm{AR} = \sqrt{\frac{E_{xo}^2 + E_{yo}^2 + \left[E_{xo}^4 + E_{yo}^4 + 2E_{xo}^2 E_{yo}^2 \cos(2\Delta\phi)\right]^{\frac{1}{2}}}{E_{xo}^2 + E_{yo}^2 - \left[E_{xo}^4 + E_{yo}^4 + 2E_{xo}^2 E_{yo}^2 \cos(2\Delta\phi)\right]^{\frac{1}{2}}}} \quad , \tag{5.1}$$

where E_{xo} and E_{yo} represent the reflection amplitudes for the horizontal and vertical polarisations respectively while $\Delta\phi$ represents the phase difference between them. For ideal circular polarisation, the AR should equal unity, or 0 dB. As shown in Fig. 5.7, the axial ratios of the simulated and measured results for our metasurface are in good agreement with each other. The axial ratio of the metasurface below the 3-dB threshold for circular polarisation spans 0.97 THz – 1.60 THz, which is equivalent to a relative bandwidth of 49%. However, the relative bandwidth obtained in simulation is much higher, which is 58% for the frequency range of 0.94 – 1.71 THz. Thus, we can infer that upon excitation with a 45° linearly polarised wave, this metasurface functions as a broadband quarter-wave mirror which outputs a reflected circularly polarised wave. To the best of our knowledge, there have been no experimentally validated realisation of quarter-wave mirrors at terahertz frequencies.

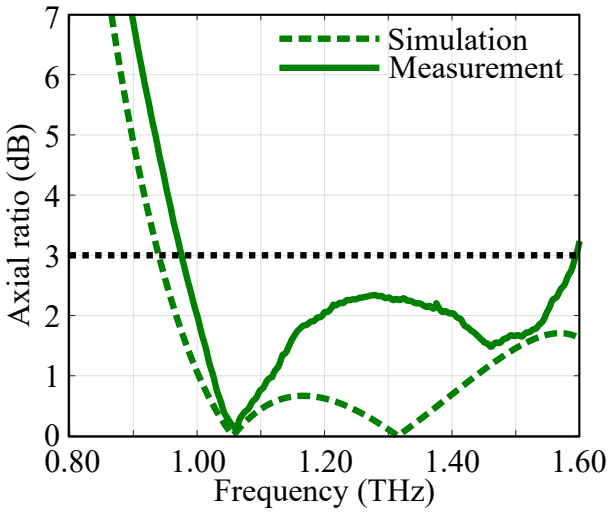

Figure 5.7. Axial ratios of the quarter-wave mirror. Simulated and measured axial ratios of the quarter-wave mirror. The black dashed line marks the 3-dB threshold for circular polarisation.

5.6 Conclusion

In conclusion, we have demonstrated a broadband and highly efficient metasurface made up of dielectric resonators. This metasurface functions as a quarter-wave mirror that operates in reflection. The quarter-wave mirror is capable of reflecting linearly polarised waves at 45° incidence into circularly polarised waves in a broadband range from 0.97 to 1.60 THz, or a relative bandwidth of 49% with high reflection efficiency. The broadband capability of this metasurface is attributed to a combination of multiple resonances arising from the geometry of the resonators. Applications of terahertz polarimetry and spectroscopy would benefit from the proposed designs. The work in this Chapter provides an alternative to metallic resonators, in order to increase the efficiency of metasurfaces at higher frequencies. Consequently, this design provides the basis for half-wave mirrors using dielectric resonators, which will be discussed in Chapter 6. A comparative study of metallic- or dielectric-resonators in metasurfaces is also detailed in Chapter 6.

Chapter 6

Broadband half-wave mirror at terahertz frequencies

IN this Chapter, we discuss half-wave mirrors at terahertz frequencies. Firstly, we present a concept and design of a broadband half-wave mirror based on dielectric resonators. The design has been fabricated and experimentally validated as a proof of concept. Based on measurement results, the half-wave mirror is shown to achieve an average conversion efficiency of 96% across the frequency range of 0.89 to 1.54 THz, corresponding to a relative bandwidth of 53%. Afterwards, we compare two designs of broadband terahertz half-wave mirrors based on metasurfaces of different types, namely either composed of metallic or dielectric resonators. As dielectric resonators operate based on oscillation of displacement currents, Ohmic loss is alleviated at terahertz frequencies. Although both designs have different operational mechanisms, the fractional bandwidth achieved by both metasurfaces is more than 67% with reflection efficiencies of greater than 80%.

6.1 Introduction

In Chapter 5 we presented a quarter-wave mirror metasurface that can convert linearly polarised waves into circularly polarised waves with high efficiencies over a large bandwidth in the terahertz range. We have demonstrated that metasurfaces can overcome the limitations set by conventional waveplates. Apart from that, we employed dielectric resonators as substitute to metallic resonators which are affected by decreasing radiation efficiencies at terahertz frequencies. In this Chapter, we present half-wave mirror metasurfaces to further demonstrate the capabilities of these structures.

Unlike quarter-wave plates, half-wave plates introduce a π phase difference between the two orthogonal field components. Consequently, they can rotate 45° linearly polarised waves by 90° and can swap the handedness of circularly polarised waves. A variant of wave plates that operate in reflection instead of transmission can be referred to as birefringent mirrors. For example, half-wave plates operate in transmission mode whereas birefringent half-wave mirrors have the same functionality but operate in reflection mode. A normally incident 45° linearly polarised wave is rotated by 90° upon reflection of a half-wave mirror. This functionality is illustrated by Fig. 6.1. As conventional metallic mirrors are isotropic, the handedness of circularly polarised (CP) waves is reversed upon reflection. An illustration of this situation is shown in Fig. 6.2(a). By contrast, a half-wave mirror can be used to preserve handedness of CP waves in reflection as shown in Fig. 6.2(b). At terahertz frequencies metallic resonators have been used to demonstrate broadband half-wave mirrors (Cheng *et al.*, 2014; Xia *et al.*, 2017; Grady *et al.*, 2013; Cong *et al.*, 2013; Mo *et al.*, 2016; Cong *et al.*, 2014; Nakata *et al.*, 2017). With metallic resonators, radiation efficiencies decrease with increasing frequencies due to Ohmic loss (Khurgin, 2015).

This Chapter includes firstly, the design, fabrication and characterisation of a broadband half-wave mirror at terahertz frequencies in Section 6.2. Then, we present metallic and dielectric broadband terahertz half-wave mirrors, with a focus on their comparative performance in Section 6.3. These metasurfaces operate in reflection mode for 45° incidence angle. The geometry of these resonators is tailored for an ultra-wide operation bandwidth.

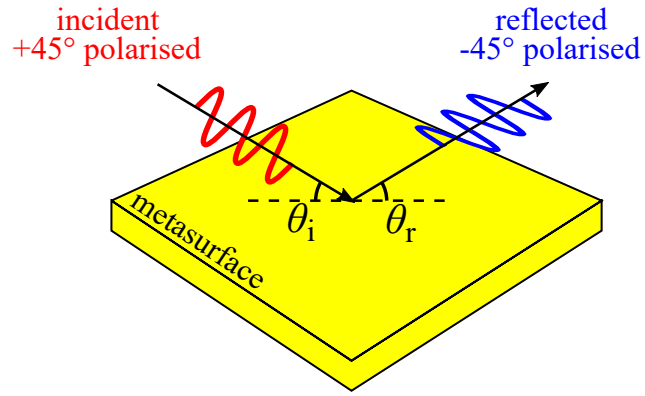

Figure 6.1. Polarisation conversion concept of half-wave mirrors. Polarisation conversion concept of half-wave mirrors. The incident $+45°$ polarised wave impinges onto the metasurface at $\theta_i = 45°$ and is reflected at angle $\theta_r = 45°$as a $+45°$ polarised wave.

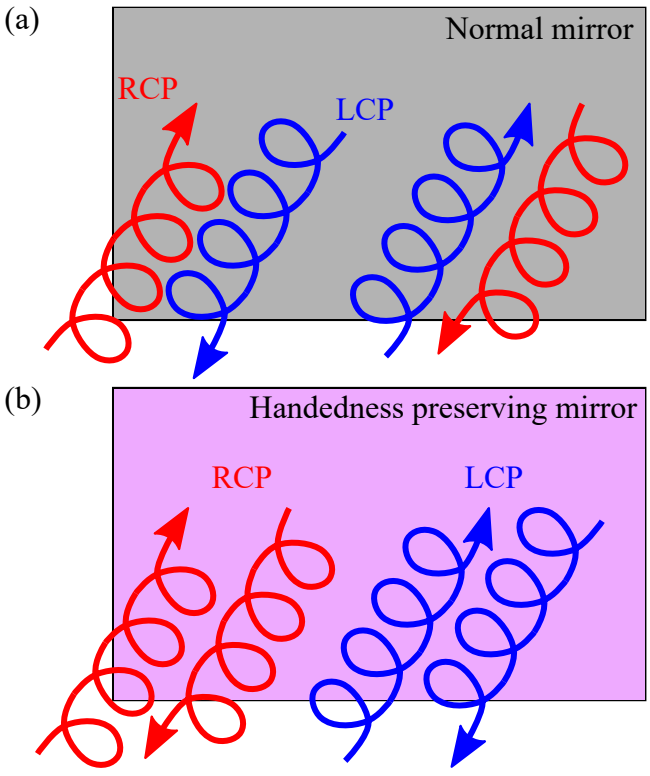

Figure 6.2. Handedness preservation concept of half-wave mirrors. Handedness preservation concept of half-wave mirrors.(a) An aluminium mirror reverses the handedness of circularly polarised waves. (b) A half-wave mirror preserves the handedness of circularly polarised waves upon reflection. Adapted from Plum and Zheludev (2015).

6.2 Dielectric-resonator half-wave mirror

In this section, dielectric resonators are employed as building blocks of half-wave mirrors in order to achieve higher efficiency. The unit cell design of the dielectric-resonator metasurface is detailed in Section 6.2.1. As the fabrication technique of this metasurface is identical to the one for the quarter-wave mirror presented in Chapter 5, it is not further elaborated here beyond an image of the fabricated sample shown in Section 6.2.2. The measurement set-up is briefly highlighted in Section 6.2.3. Experiment results of this design are shown in Section 6.2.4 followed by a conclusion in Section 6.4.

6.2.1 Design

A similar design concept as for the quarter-wave mirror presented in Chapter 5 can be adapted to create a half-wave mirror. The initial unit cell design for the half-wave mirror is shown in Fig. 6.3(a). A dielectric resonator with sinusoidal edges is again made up of high-resistivity float-zone silicon on a 200 nm thick gold ground plane. For this design however, the height of the resonator is slightly reduced to 48 μm. The square unit cell is 76 μm in length, which is less than half the shortest operating wavelength of 176 μm at 1.70 THz to avoid grating lobes. A periodic repetition of this unit cell as shown in Fig. 6.3(a) in the x and y directions makes a reflective half-wave mirror. The large difference in length and width in this design is essential to obtain the required phase response from the orthogonal electric field components. In this configuration, as a main difference to the previously presented quarter-wave mirror design, the resonators connect to form long, continuous bars in the y-dimension. This causes the structure to be very fragile due to the high mechanical stress at material interfaces between the continuous silicon bars and gold plate, particularly under temperature variations. As such, in the manufactured prototype, the continuous silicon bars of narrow width relative to long length (of 50 mm) developed stress cracks, causing delamination. In order to alleviate this mechanical stress, a gap of 6 μm is periodically introduced at every 14 unit cells. 14 unit cells were sufficient to provide a similar phase response with the introduction of the gap.

The simulated reflection phase profiles for the original and modified designs are shown in Fig. 6.4(a) and 6.4(b) respectively. In general, the performance of the two designs are very similar. From either Fig. 6.4(a) and (b), we can infer three resonance modes from zero phase crossings, two of which for the vertical polarisation and the other one for the

horizontal polarisation. These three resonances support a phase difference of close to π radian between the two orthogonal linearly polarised electric field components from 0.95 THz to 1.70 THz as shown in Fig. 6.4(c). It is noted that, with the introduction of a gap, as shown in Fig. 6.3(b), the positions of the three unique resonances do not shift, as indicated in Fig. 6.4(b). However, there are minimal fluctuations in the phase response for the vertically polarised component due to weak high-order resonances arising in the finite-length bars.

The mechanism of the three resonances is directly linked to the resonator geometry. Figure 6.5 shows the electric fields of the three resonances at their respective frequencies. There are three unique resonances that contribute to the broadband behaviour of the half-wave mirror. The phase response for the vertically polarised component approaches the zero crossing first, as the resonator is much larger in the y-dimension. Figure 6.5(a) shows this first resonance at 0.77 THz, which is a magnetic dipole as the electric fields oscillate in a half-loop manner. Subsequently, the phase response of the horizontally polarised component approaches the zero crossing on resonance at 1.27 THz. This second resonance is also a magnetic dipole as the electric fields oscillate in a half-loop manner, as shown in Fig. 6.5(b). Lastly, the phase response of the vertically polarised component approaches the zero crossing once more at 1.78 THz. As shown in Fig. 6.5(c), this resonance mode is of a higher-order mode, with two magnetic dipoles with circulating electric fields around the top and bottom of the resonator. The variation

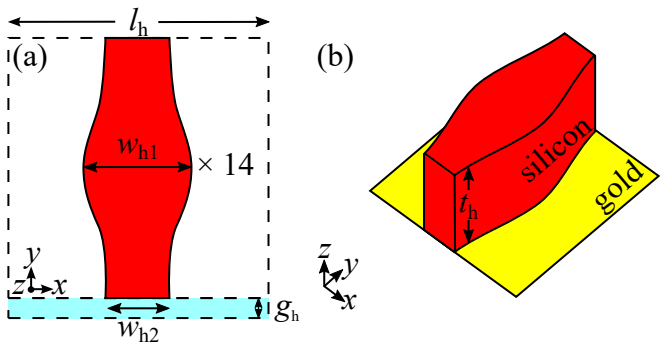

Figure 6.3. Unit cell design of the half-wave mirror. Unit cell design of the half-wave mirror. (a) Unit cell design and (b) 3D schematic of the original unit cell design. The modified array design consists of 14 identical unit cells as shown in (a), followed by an extra gap of 6 µm as indicated by the shaded area. The dimensions are as follow: $l_h = 76$ µm, $w_{h1} = 30$ µm, $w_{h2} = 16$ µm, $g_h = 6$ µm, $t_h = 48$ µm.

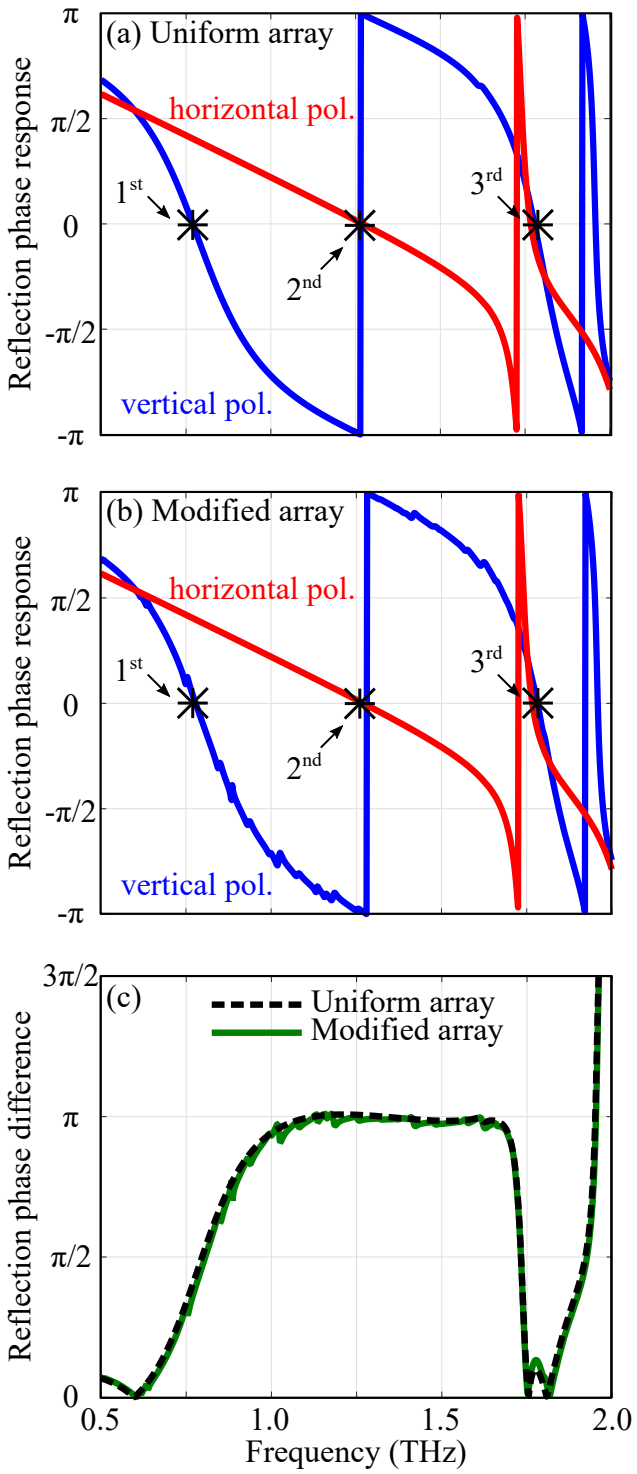

Figure 6.4. Simulated reflection phase profiles of the half-wave mirror. Simulated reflection phase profiles of the half-wave mirror. Reflection phase responses of the two orthogonal polarisations for the (a) original uniform array and (b) the modified array. (c) The reflection phase difference between the two orthogonal polarisations. The markers in (a) and (b) indicate resonance modes of the half-wave mirrors.

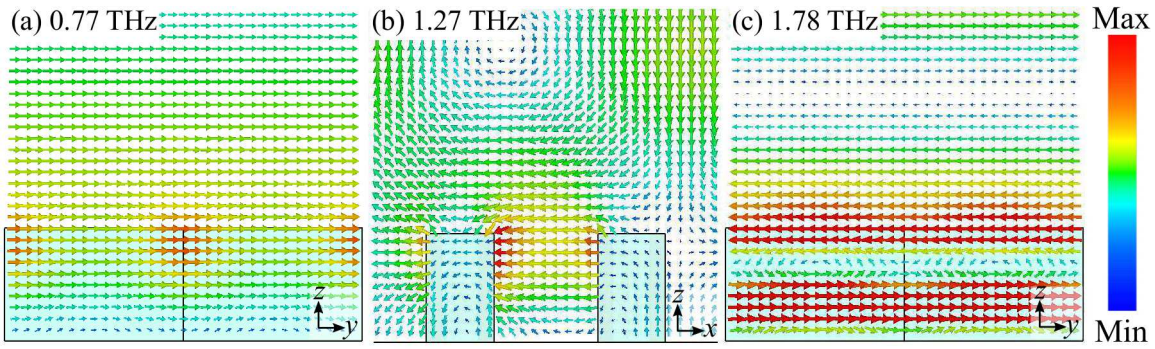

Figure 6.5. Electric field distributions of the half-wave mirror. Electric field distributions of the uniform dielectric resonator array of the half-wave mirror in their respective planes at the three resonances at (a) 0.77 THz, (b) 1.27 THz and (c) 1.78 THz. These figures are snapshots when the electric fields are at their maximum. The waves are y-polarised in (a-b) and x-polarised in (c) and the incident wave is at 45° in the xz plane.

in the width of the resonator allows for the confinement and thus oscillation of displacement currents which support the excitation of both considered resonance modes for vertical polarisation. Thus, the reflective near π phase difference is maintained, with minimal fluctuations as shown in Fig. 6.4(c).

6.2.2 Fabrication

A portion of the manufactured half-wave mirror is shown in Fig. 6.6, where the gap between two long bars, each comprising 14 unit cells, is illustrated. The half-wave mirror is fabricated using the same procedure used for the quarter-wave mirror in Chapter 5.

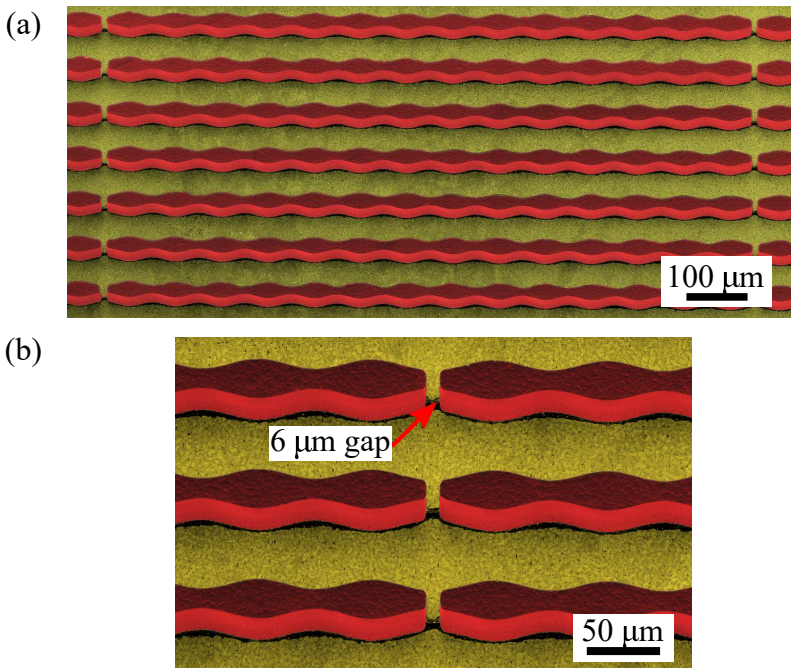

Figure 6.6. Scanning electron micrographs of a section of the half-wave mirror. Scanning electron micrographs of a section of the half-wave mirror at isometric views. (a) Blocks of 14 unit cells and (b) a closed up of the gap, which is indicated by an arrow.

6.2.3 Measurement

We use a fiber-coupled terahertz time-domain spectroscopy for experiment validation. A schematic of the experiment set-up is shown in Fig. 6.7. To collimate and focus the Gaussian beam, we use lenses with a focal length of 5 cm. Additionally, wire-grid polarisers are utilised to ensure polarisation purity. The focused beam, either vertically- or horizontally- polarised, illuminates the sample at 45°. The metasurface then reflects the incident beam into the lenses, which focuses the beam into the linearly polarised detector. This detector can be rotated to measure either vertically- or horizontally-polarised waves. For a Gaussian beam of waist of 1 mm, the corresponding Rayleigh range is 10 mm at a wavelength of 300 μm. As the focused Gaussian beam impinging on the sample is around the location of the beam waist, the beam can be assumed as having negligible angular divergence.

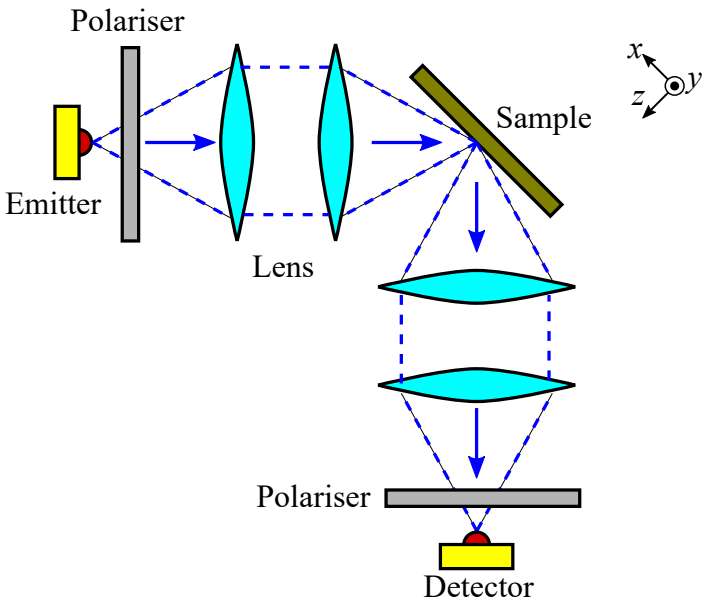

Figure 6.7. Schematic of the 45° incident set-up. Schematic of the experiment set-up. The focused beam in this image is exaggerated and does not reflect on actual Rayleigh length of the beam.

6.2.4 Results

For the validation experiment, the half-wave mirror is excited with a 45°-polarised wave at 45° incidence and the detector measures the outgoing specularly reflected waves. Two sets of measurements are taken where the first set measures the co-polarisation and the second set measures cross-polarisation, which correspond to the reflected $+45°$ and $-45°$ polarised waves respectively. Figure 6.8 indicates that the simulated and measured results are in good agreement. From Fig. 6.8, it is observed that the cross-polarisation amplitude is greater than 88%, with an average of 97% in simulation while the co-polarisation amplitude is smaller than 31%, with an average around 9% for a frequency range of 0.79 – 1.58 THz. In measurement, the cross-polarisation amplitude is greater than 72%, with an average of 79% while the co-polarisation amplitude is smaller than 31%, with an average of 15% for a frequency range of 0.89 – 1.54 THz. Experimental tolerances including beam quality and system alignment contribute towards the missing energy in the measured co-polarisation component. The slight shift in the frequency range of interest can be attributed to fabrication tolerances.

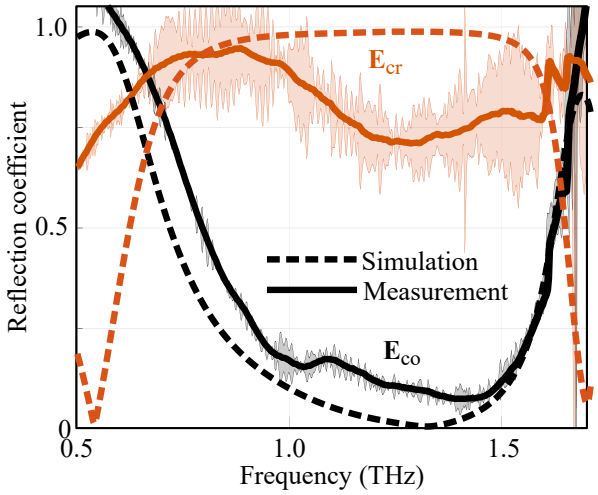

Figure 6.8. Reflection amplitude profiles of the half-wave mirror at $45°$ incidence. Reflection amplitude profiles of the half-wave mirror at $45°$ incidence. E_{co} and E_{cr} correspond to the reflected $+45°$ and $-45°$ polarised waves respectively. The solid lines indicate measured results while the dashed lines indicate simulated results. Error ranges due to experimental tolerances are indicated with shaded regions.

To determine the conversion efficiency of this half-wave mirror, we then proceed to calculate the polarisation conversion ratio (PCR) (Hao *et al.*, 2007) which is defined as:

$$\mathrm{PCR} = \frac{|E_{\mathrm{cr}}|^2}{|E_{\mathrm{cr}}|^2 + |E_{\mathrm{co}}|^2}, \tag{6.1}$$

where E_{cr} represents cross-polarised amplitude and E_{co} represents co-polarised amplitude.

The PCR for the half-wave mirror is presented in Fig. 6.9, showing a relative bandwidth of 53% within the operating range of 0.89 THz – 1.54 THz. The relative bandwidth is defined to be the region where the PCR is above 90%. Similarly, the PCR obtained from simulation has a relative bandwidth of 66%, corresponding to a frequency range of 0.79 THz – 1.58 THz. An existing design by Cheng *et al.* (Cheng *et al.*, 2014) achieved a simulated relative bandwidth of 65%, corresponding to a frequency range of 0.72 THz – 1.41 THz. Ma *et al.* (Ma *et al.*, 2017) demonstrates a metallic half-wave mirror with a relative bandwidth of 85%, corresponding to a frequency range of 0.40 THz – 0.99 THz. For the band where the PCR is greater than 90%, we calculate the PCR values for all three designs. Our design ultimately, achieves a markedly higher measured average polarization conversion efficiency of 96% as compared to 71% by Cheng *et al.* and 94% by Ma *et al.* Thus, polarization conversion mirrors consisting of dielectric resonators improve radiation efficiencies as compared to their metallic counterparts. The high value of conversion efficiency implies that our metasurface can rotate 45° incident linearly polarized waves by 90°. Additionally, in reflection, a half-wave mirror can preserve the handedness of circularly polarized waves.

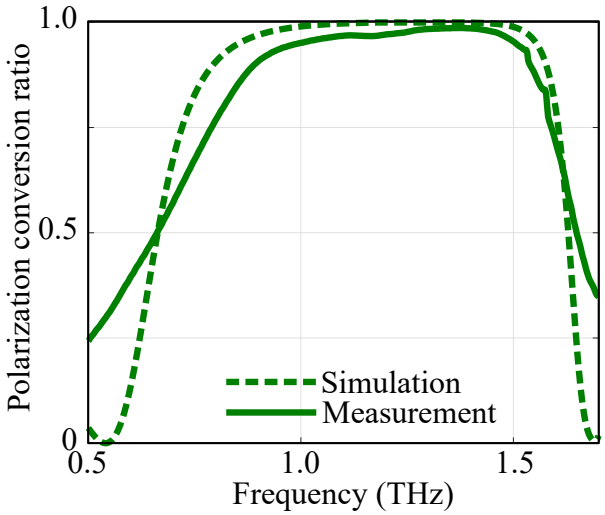

Figure 6.9. Polarisation conversion ratio of the half-wave mirror. Polarisation conversion ratio of the half-wave mirror. This PCR is calculated from the amplitude responses in Fig. 6.8 by using Eq. 6.1.

6.3 Metallic- and dielectric-resonator half-wave mirrors

In this section, we compare the performance of metallic- and dielectric-resonator based metasurfaces that are functional broadband half-wave mirrors. The unit cell design is detailed in Section 6.3.1, followed by simulated results and discussion in Section 6.3.2. Lastly, a conclusion to this work is presented in Section 6.4.

6.3.1 Design

The unit cell design for the half-wave mirror based on metallic resonators is shown in Fig. 6.10(a). This design is adapted from Cheng *et al.* (2014) for comparison purposes. The top layer of the unit cell consists of a planar coaxial disk-ring resonator of gold with a thickness of 0.2 μm. The dielectric spacer is made of 27 μm thick cyclo-olefin copolymer (COC) which has a relative permittivity of $\epsilon_r = 2.34$ and loss tangent $\tan\delta = 0.0007$ (Peytavit *et al.*, 2011; Nielsen *et al.*, 2009). Figure 6.10(b) shows the unit cell design for dielectric resonators. A cross-shaped resonator on the top layer is made of high-resistivity float-zone silicon with relative permittivity of $\epsilon_r = 11.68$, $\tan\delta \simeq 0.0002$ and thickness of 44 μm. The ground plane of both metallic and dielectric resonators is a gold layer of thickness 0.2 μm. Both structures can be fabricated with photolithographic technologies (Headland *et al.*, 2017; Lee *et al.*, 2018b).

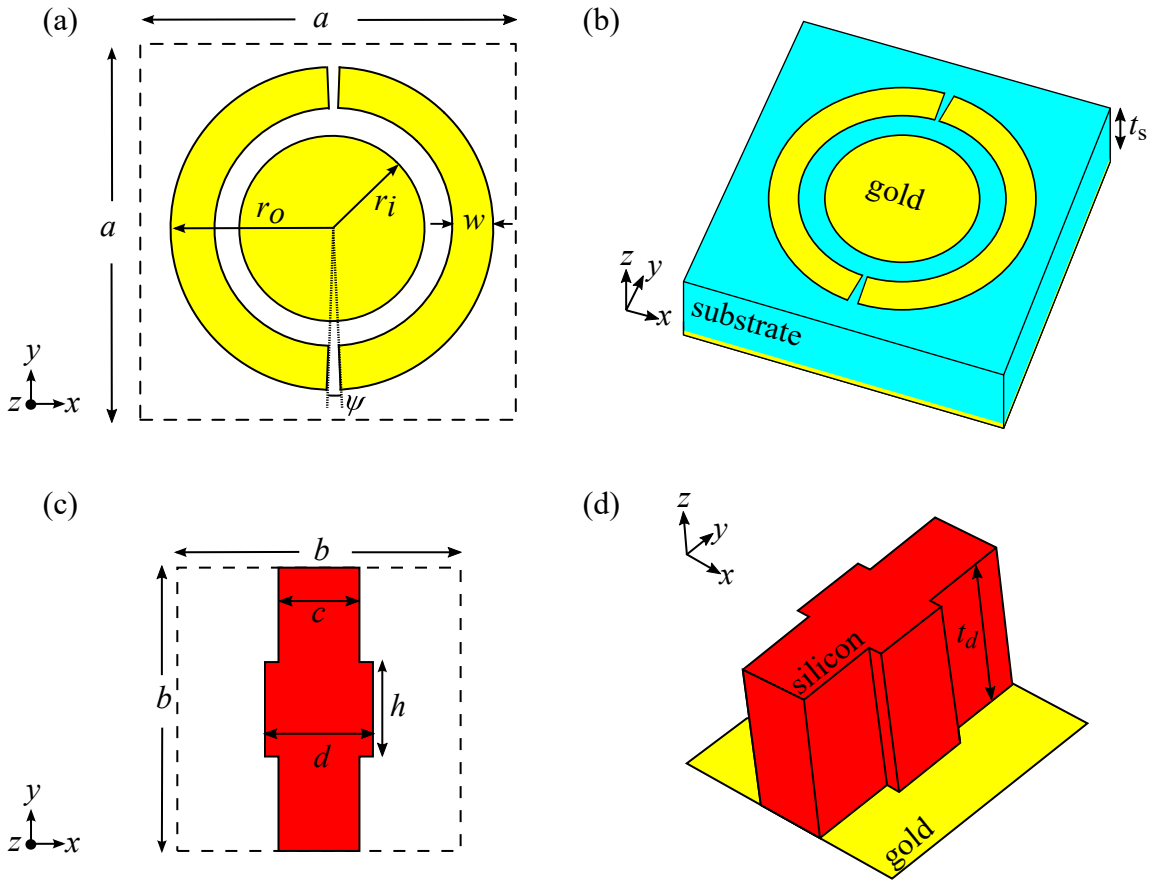

Figure 6.10. Unit cell design of metallic- and dielectric-resonator half-wave mirrors. Unit cell design of the respective half-wave mirrors. (a) Metallic resonator. The dimensions are as follows: a = 92.5 μm, r_i = 21.5 μm, r_o = 37 μm, w = 9 μm, $\psi = 4.11°$, t_s = 27 μm. (b) Three-dimensional representation of the metallic-resonator unit cell. (c) Dielectric resonator. The dimensions are as follows: b = 70 μm, c = 20 μm, d = 28 μm, h = 22 μm, t_d = 44 μm. (d) Three-dimensional representation of the dielectric-resonator unit cell.

When the metallic resonator in Fig. 6.10(a) or (b) is repeated periodically along the x and y axes, the resulting arrays function as half-wave mirrors over 0.9 – 1.8 THz. The mechanism of the metallic resonator metasurface can be understood from the resolved current distributions in response to the decomposed incident electric fields (Cheng *et al.*, 2014). Figure 6.11 shows the surface current distributions of the three unique resonances present in the metallic-resonator half-wave mirror. At the first resonance frequency of 0.89 THz as shown in Fig 6.11(a), the outer ring of the unit cell couples with the y-polarised component, which constitutes a zero phase in reflection. A $-\pi$ phase shift is imparted by the ground plane on the y-polarised component, as the x-polarised component does not resonate at this frequency. At the second resonance frequency of 1.32 THz as shown in Fig. 6.11(b), the y-polarised component excites a set of dipoles which constitutes a zero phase in reflection. The x-polarised component does not resonate at this frequency, thus a $-\pi$ phase is imparted off the ground plane in reflection. At 1.87 THz, the y-polarised component once again excites dipoles in the disk and the outer ring of the resonator as shown in Fig 6.11(c). This imparts a zero phase change in reflection. The ground plane then inflicts an $-\pi$ phase difference in the y-polarised component. Thus, the resonating element yields a π phase difference between the x- and y-polarised electric field components in reflection across a broad spectral band.

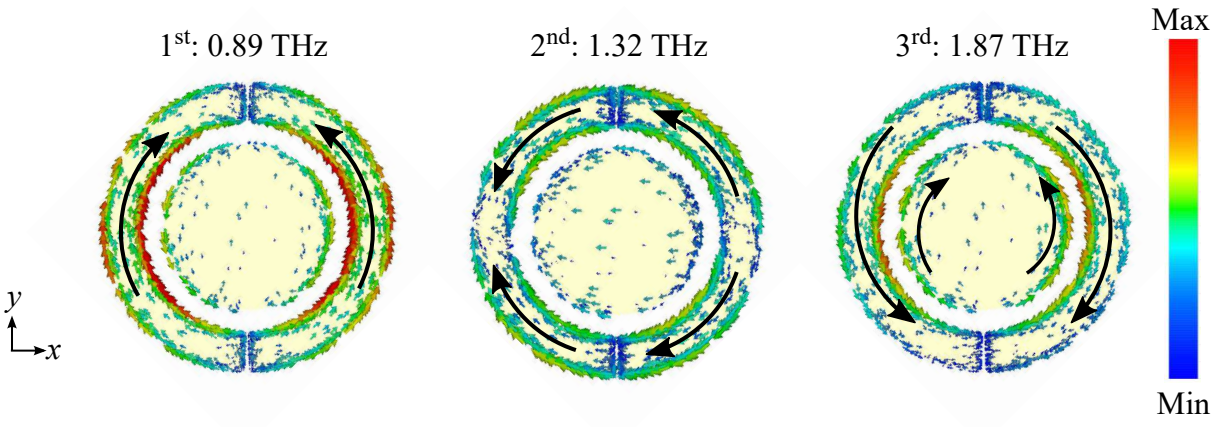

Figure 6.11. Surface current distributions of the metallic-resonator half-wave mirror. Surface current distributions of the uniform metallic-resonator array of the half-wave mirror from the top view at the three resonances at (a) 0.89 THz, (b) 1.32 THz and (c) 1.87 THz. The incident wave is at 45° in the xz plane.

Like the sine-shaped dielectric-resonator half-wave mirror in Section 6.2, there are also three unique resonances in this design. The first resonance at 0.81 THz, a magnetic dipole resonance is shown in Fig. 6.12(a). Next, the second resonance at 1.34 THz which is also a magnetic dipole resonance is shown in Fig. 6.12(b). Lastly, the third resonance, which is of a higher-order mode consisting of two magnetic dipoles is shown in Fig. 6.12(c). It is noteworthy that, since the resonator is infinitely long in simulation, the electric field distributions corresponding to the magnetic dipoles appear more horizontal rather than circular.

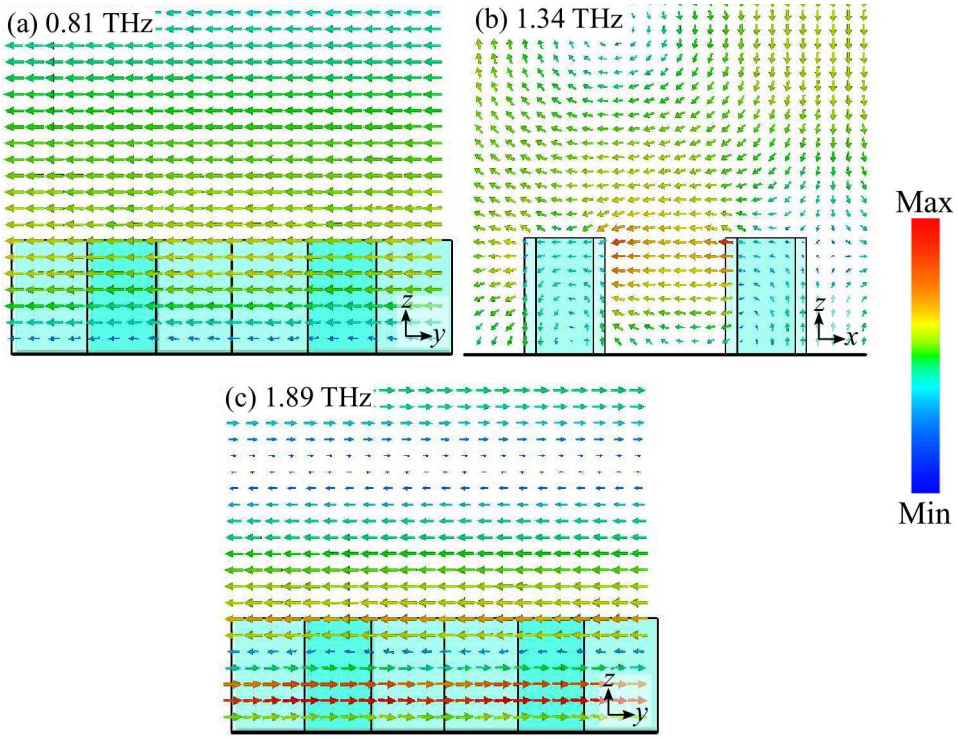

Figure 6.12. Electric field distributions of the dielectric-resonator half-wave mirror. Electric field distributions of the uniform dielectric resonator array of the half-wave mirror in their respective planes at the three resonances at (a) 0.81 THz, (b) 1.34 THz and (c) 1.89 THz. These figures are snapshots when the electric fields are at their maximum. The waves are y-polarised in (a-b) and x-polarised in (c) and the incident wave is at 45° in the xz plane.

6.3.2 Simulation results

We simulate these structures with the frequency-domain solver in CST Microwave Studio. For an infinite array simulation, we apply periodic boundary conditions to the unit cell with a Floquet port excitation at an incidence angle of $+45^\circ$. The reflection amplitude profiles for arrays consisting of metallic and dielectric resonators are shown in Fig. 6.13(a) and (b), with curves for both co- and cross-polarisation. Co- and cross-polarisation correspond to reflected $+45^\circ$ and -45° polarised waves respectively, where the incident wave is $+45^\circ$ polarised. We can infer that both metasurfaces are excellent at polarisation conversion as the cross-polarised amplitudes are significantly higher than the co-polarised amplitudes.

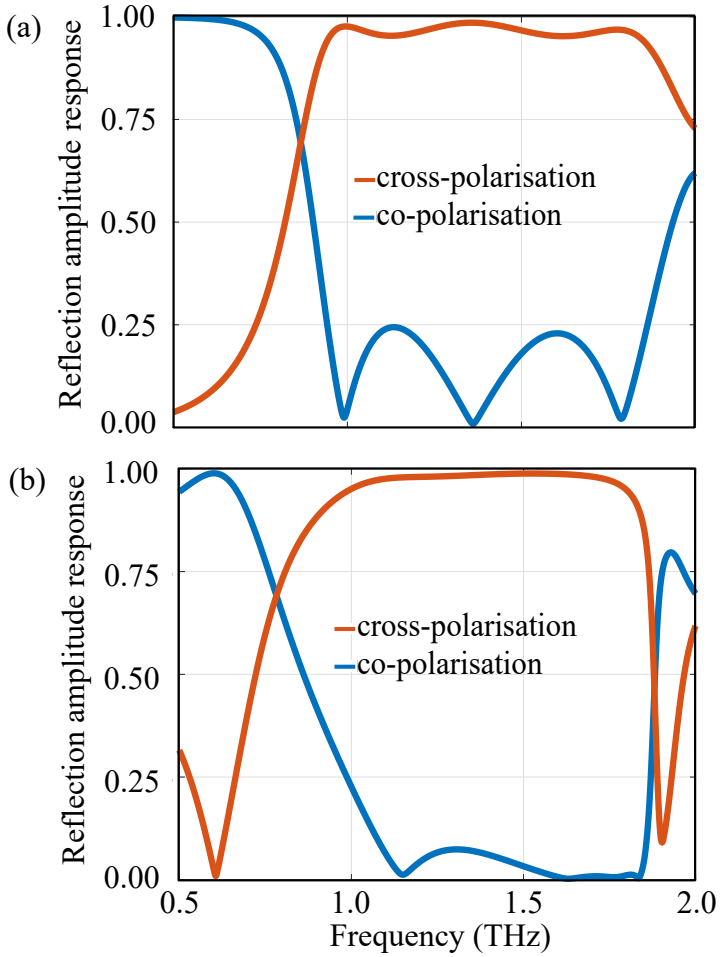

Figure 6.13. Reflection amplitude profiles of half-wave mirrors. Reflection amplitude profiles of (a) metallic- and (b) dielectric-resonator metasurfaces at 45° incidence. The co- and cross-polarisation labels correspond to the reflected $+45^\circ$ and -45° polarised waves respectively.

Figure 6.14 shows the polarisation conversion efficiency (PCR) for the metallic- and dieletric-resonator metasurfaces. The average PCR for the dielectric-resonator metasurface is 99% as compared to 97% for the metallic-resonator counterpart (0.92 THz – 1.87 THz). For the region where the PCR is greater than 80%, the fractional bandwidth is 71% for metallic-resonator metasurfaces (0.91 THz – 1.91 THz) and 67% for dielectric-resonator metasurfaces (0.89 THz – 1.87 THz).

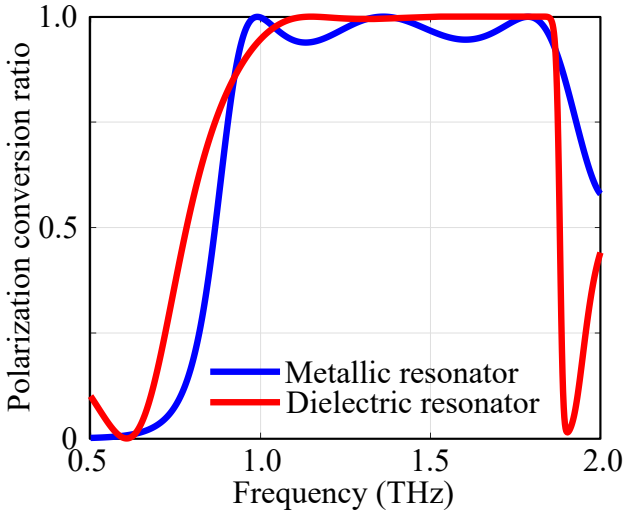

Figure 6.14. Polarisation conversion ratio of the half-wave mirrors. This PCR is calculated from the amplitude responses in Fig. 6.13 by using Eq. 6.1. The blue line indicates the PCR of the metallic-resonator metasurface while the red line indicates the PCR of the dielectric-resonator metasurface.

For the same bandwidth requirements, we calculate the efficiencies of both metallic- and dielectric-resonator half-wave mirrors as shown in Fig. 6.15. The average efficiency across their respective fractional bandwidths is 93% for metallic resonators and 94% for dielectric resonators. These values of efficiency indicate that both metasurfaces are highly efficient half-wave mirrors.

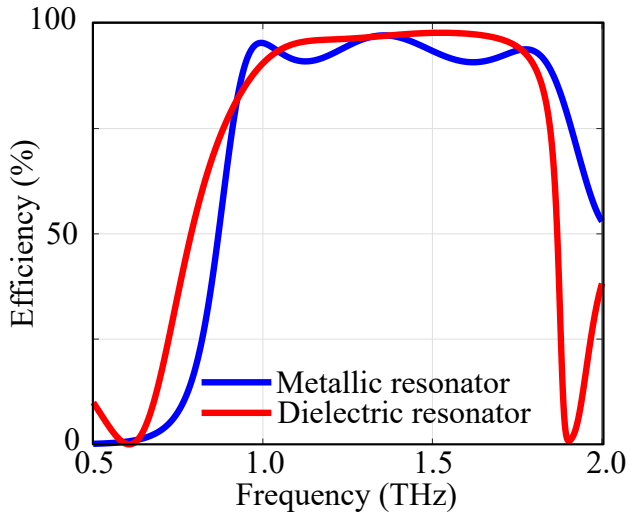

Figure 6.15. Simulated efficiencies of the half-wave mirrors. Simulated efficiencies of the metallic- and dielectric-resonator half-wave mirror. The blue line indicates the efficiency of the metallic-resonator metasurface while the red line indicates the efficiency of the dielectric-resonator metasurface.

The reflection phase profiles of the uniform array in response to x- and y-polarised waves are shown in Fig. 6.16(a) and (b). From the zero phase crossings in these figures, we can infer the three resonance modes existing in both metasurfaces. By design, these resonances support a phase difference of close to π radian between the two orthogonal linearly polarised electric field components. It is also noteworthy that dielectric resonators exhibit a smoother phase variation as compared to their metallic counterparts as mentioned in Section 2.4. The phase gradient as a function of the frequency is dependent on the radiation quality factor of resonators, Q_r where a larger value would result in a steeper phase gradient. The lower Q_r and thus smoother phase gradient of the dielectric resonators is due to their higher radiation loss or better coupling with free space.

From Fig. 6.17 we can observe the reflection phase difference between the two orthogonal linearly polarised electric field components for both metasurfaces. We can observe that within the 0.92 THz – 1.87 THz range, a near π phase difference between the two orthogonal electric field components in reflection is well maintained. Based on the phase profile and PCR values, dielectric metasurfaces appear slightly more efficient in polarisation conversion with better coupling to free space due to their lower Q_r compared to their metallic counterparts.

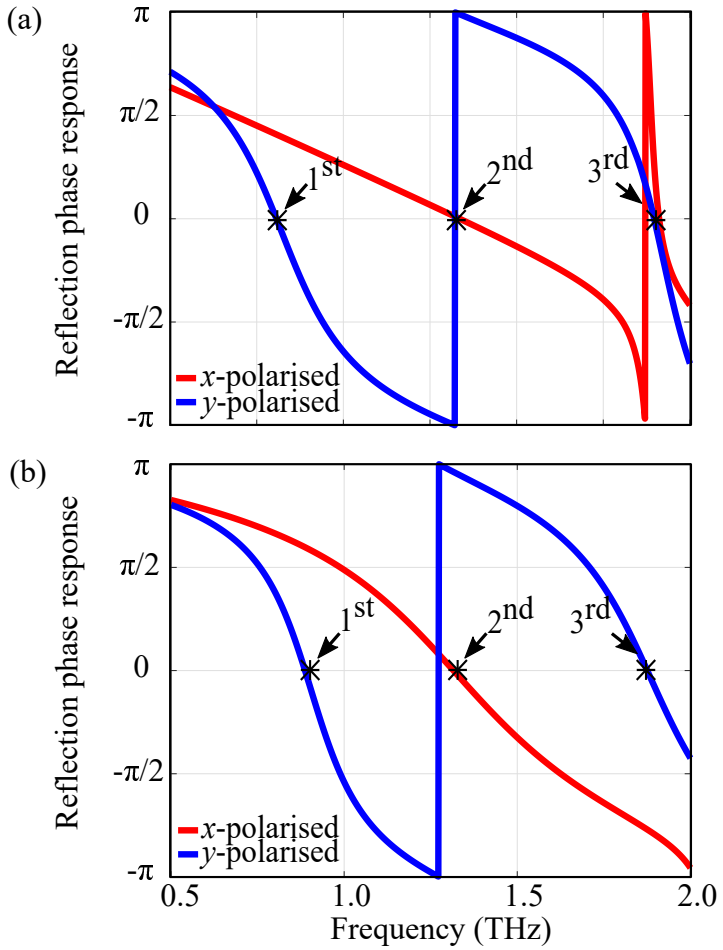

Figure 6.16. Reflection phase responses of the half-wave mirrors. (a) Metallic- and (b) dielectric-resonator metasurfaces.

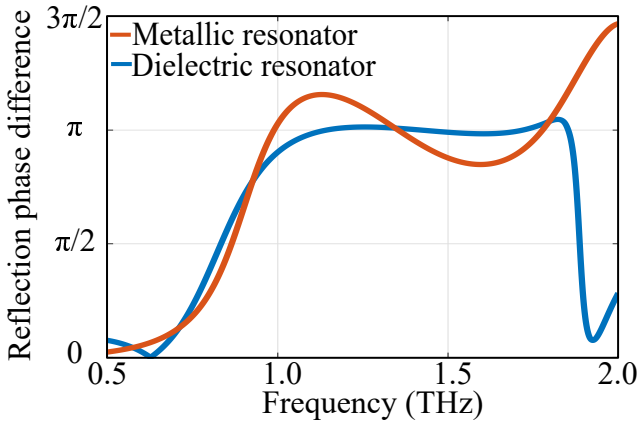

Figure 6.17. Simulated reflection phase difference of the half-wave mirrors. Phase difference between x-polarised and y-polarised waves for metallic-and dielectric-resonator half-wave mirrors.

6.4 Conclusion

As proof of concept, we fabricated and demonstrated a modified dielectric-resonator based half-wave mirror. This broadband and highly efficient half-wave mirror is capable of converting linearly polarised terahertz waves into its orthogonal polarised counterpart as well as preserving the handedness of circularly polarised waves upon reflection, in contrast to common mirrors. The average measured conversion efficiency of the half-wave mirror is 96% across the frequency range of 0.89 to 1.54 THz, corresponding to a relative bandwidth of 53%. The broadband capability of both metasurfaces is attributed to a combination of multiple resonances arising from the geometry of the resonators. Applications of terahertz polarimetry and spectroscopy would benefit from the proposed design.

In the second part of the chapter, we used simulations to directly compare designs of metallic-resonator and dielectric-resonator metasurfaces capable of rotating linearly polarised waves by 90° and preserving handedness of circularly polarised waves. The fractional bandwidth for metallic-resonators is 71% (0.91 THz – 1.91 THz) while the fractional bandwidth for dielectric-resonators is 67% (0.89 THz – 1.87 THz) for a polarisation conversion ratio greater than 80%. Dielectric resonator metasurfaces are slightly more efficient in polarisation conversion than metallic resonators as expressed by a higher polarisation conversion ratio. Nevertheless, both metasurfaces exhibit similar performance across the frequency band of interest despite different operation mechanisms.

Chapter 7

Summary and outlook

THIS Chapter concludes the work presented in this thesis. Part I of this thesis contains Chapters 1 and 2, which details the relevant background information of this doctoral thesis. This covers the motivation behind the studies in this thesis, techniques for wavefront engineering and previous relevant work. Chapters 3 to 6 describe original contributions to the design and realisation of broadband, highly efficient metasurfaces with engineered birefringence. Specifically, Part II, which includes Chapter 3 contains a metasurface design with metallic resonators. Part III, which includes Chapters 4 to 6, showcases efforts to improve the efficiency of metallic-resonator metasurfaces by substituting them with dielectric-resonators and examining their comparative performance. Lastly, an outlook for future research on terahertz metasurfaces is presented.

7.1 Part I: Background

The first part of this thesis has introduced the research challenges that were addressed throughout this study. Relevant background information has been provided in Chapter 2 to give the reader basic concepts utilised in this work.

Chapter 1: Introduction

This Chapter has briefly introduced the conventional method used to achieved polarisation conversion. Usage of bulk optics such as wave plates to achieve polarisation conversion has several limitations, which include large thickness, low efficiencies and narrowband operations at terahertz frequencies. There are also limited options for natural materials that exhibit strong birefringence. This motivates researchers to look for alternative methods to design devices that have engineered birefringence at desired frequencies. Thus, the main motivation behind this work is to overcome limitations set by conventional polarisation conversion methods in the terahertz frequency range. An alternative solution is provided by metasurfaces, which have been proposed with the aim to address said limitations. Compact, planar, highly efficient and broadband metasurfaces are essential towards practical applications in the terahertz region. Additionally, this Chapter has also presented a detailed structure of this thesis, accompanied by a summary of the original contributions.

Chapter 2: Background

The proposed solution towards creating engineered birefringence through exploiting the concept of metasurfaces, has been elaborated in this Chapter. General laws of reflection and refraction have been introduced to give a better understanding of the behaviour of electromagnetic radiation in free space, and as it propagates through materials of different refractive indices. The operational mechanism of metasurfaces are detailed to give a better understanding on how the incident electromagnetic wave is shaped to its desired output. Furthermore, a thorough literature review of past and present work was included in this Chapter. Most of the metasurfaces discussed have been experimentally validated. Experimentally demonstrated devices provide the stepping stone towards accelerated integration into real-world applications. The advantages and disadvantages of previous metasurfaces designed for polarisation conversion have been discussed.

Consequently, key issues worthy of investigation were highlighted which provide the backbone of the work in this thesis.

7.2 Part II: Metallic resonators

The second part of this thesis has solely focused on metasurfaces with engineered birefringence consisting of metallic resonators to validate the proposed alternative.

Chapter 3: Broadband terahertz circular-polarisation beam splitter

Aim: Polarisation-dependent beam splitting is an important function in terahertz communications, particularly in applications that require polarisation-dependent multiplexing or demultiplexing. As there are limited natural materials available that exhibit strong birefringence in the terahertz region, devices that can split circularly polarised waves have not been realised. The proposed alternative is to utilise metasurfaces that can effectively distinguish between the handedness of circularly polarised terahertz waves and split them into opposing directions. The reflected beam directions can be controlled by the resonating elements that are tailored for such a function.

Methodology: Metallic resonators were employed to achieve circular-polarisation beam splitting. Each resonator provides a half-wave response over a large bandwidth. These resonators are then gradually rotated up to 180°, to form a metasurface, that can achieve the required deflection. With this geometry, the left- or right-handed circularly polarised waves will undergo a different phase response. Thus, left- or right-handed circularly polarised waves will be reflected into different directions. A design based on this principle was fabricated according to the procedures detailed in this Chapter. Additionally, cyclo-olefin copolymer (COC) was used as a dielectric spacer as it has a lower loss than more commonly used polydimethylsiloxane (PDMS) spacers. THz-TDS with angular scanning was used to characterise the functionality of this metasurface.

Results: The beam splitting capabilities of the metasurface were verified. Experiments revealed that the metasurface is able to deflect arbitrary incident circularly polarised terahertz waves into predetermined opposing angles, depending on their

handedness. In addition, the metasurface is functional for a frequency range of 0.58 THz to 1.00 THz, corresponding to a relative deflection bandwidth of 53%. The measured efficiency for this metasurface is 61% at 0.78 THz.

Original contribution: The main contribution of this work is the functionality of this metasurface. To the best of our knowledge, this is the first reflective circular-polarisation beam splitter at terahertz frequencies with broadband functionality. Lastly, this study achieves the main aim of this doctoral thesis, which is to design highly efficient, broadband metasurfaces with engineered birefringence.

7.3 Part III: Dielectric resonators

The third part of this thesis aimed at improving the efficiency of metasurfaces by employing dielectric-resonators in place of metallic-resonators. Several metasurfaces were designed and validated to demonstrate this concept. Lastly, a comparative study between metallic- and dielectric-resonator based metasurfaces was conducted.

Chapter 4: Terahertz near-field imaging of dielectric resonators

Aim: Dielectric-resonator metasurfaces can exhibit low-order resonant modes, namely the electric dipole resonance and the magnetic dipole resonance in a single layer. As these resonances are crucial elements towards designing highly efficient metasurfaces, a study utilising a near-field microscope has been conducted to examine the nature of these resonances.

Methodology: A dielectric-resonator array was designed and fabricated with the process detailed in this Chapter. The geometry of the dielectric resonator was tailored to exhibit an electric dipole resonance at 0.58 THz and the magnetic dipole resonance at 0.61 THz. This intrinsic silicon dielectric resonator makes up the top layer of this metasurface, while the substrate is quartz. To characterise the sample, the near-field microscope at the University of Freiburg was used. Far-field measurements were also taken to confirm the positions of these resonances.

Results: A two-dimensional raster scan was done on the sample to examine the electric near-fields. At the lower frequency of 0.58 THz, we can observe a resonance pattern that constitutes to an electric dipole resonance. Strong electric fields in the

direction of propagation at 0.61 THz indicates that the magnetic dipole resonance is present, as it is characteristic for this mode of resonance to have out-of-the-plane circulation of electric fields. Far-field measurements also confirm the positions of these resonances through examining the resonant dips in the transmission amplitude response. Both near-field and far-field measured results are in good agreement with the simulated results.

Original contribution: Resonant electric fields in dielectric resonators are solely confined within the resonators. Thus, these fields are not readily accessible with the near-field probe. In contrast, resonant electric fields of metallic resonators are easily accessed with a near-field probe as their resonant electric fields are not confined within the structure. Unique electromagnetic interactions between dielectric resonators were observed in the near-field through this study. It is noteworthy to mention that these interactions cannot be observed in the far-field measurements. This study provides insight towards designing dielectric resonator based metasurfaces that utilise these low-order resonant modes.

Chapter 5: Broadband quarter-wave mirror at terahertz frequencies

Aim: Metasurfaces with engineered birefringence require a specific resonator geometry that exhibits the required phase difference between orthogonal electric field components. Typically, this resonator geometry has a larger dimension in length as compared to width. Additionally, metasurfaces as polarisation converters require broadband capabilities which are essential towards practical applications in the terahertz region. Thus, dielectric resonators were employed as resonating elements to function as a quarter-wave mirror with high efficiency and broadband functionalities.

Methodology: A sine-shaped resonator where the length is larger than the width allows for a different phase response of the two orthogonal electric field components. The required phase difference between the orthogonal electric field components for a quarter-wave mirror is $\pi/2$. The resulting resonating elements are then arranged in a periodic manner and a full array has been fabricated by our collaborators in RMIT University. Collectively, the geometry of these resonators allow for a broadband functionality through a combination of multiple resonances. An experiment was then conducted using THz-TDS to characterise this sample.

Results: The quarter-wave mirror is able to reflect linearly polarised waves at 45° incidence into circularly polarised waves. This functionality is preserved over a broadband range from 0.97 to 1.60 THz, which is equivalent to a relative bandwidth of 49% with high reflection efficiency.

Original contribution: To the best of our knowledge, this is the first experimentally demonstrated quarter-wave mirror at terahertz frequencies. The geometry of the resonator was also tailored to better suit fabrication processes. Dielectric-resonator metasurfaces were shown to increase efficiencies at terahertz frequencies. This study is also aligned with the main aim of this doctoral thesis.

Chapter 6: Broadband half-wave mirror at terahertz frequencies

Aim: Based on the design in Chapter 5, a further study on dielectric-resonator metasurfaces was conducted. The phase difference between the two orthogonal electric field components has been increased to exhibit a half-wave response. Apart from that, a comparative study of metallic- and dielectric-resonator metasurfaces is conducted in this Chapter.

Methodology: Initially, a sine-shaped dielectric resonator that exhibited a π phase difference between the orthogonal electric field components was chosen as the resonant element. The unit cell was then repeated in the xy dimensions to realise an array. This array was then fabricated and experimentally validated. Next, a metallic- and dielectric-resonator half-wave mirror were designed and simulated. The metallic-resonator half-wave mirror was inspired from a study by Cheng *et al.* (2014) while the dielectric-resonator was of a cross-shaped silicon resonator. The cross-shape was chosen for its design, where the length is larger than the width, which exhibits a different phase response for the two orthogonal electric field components. Using CST Microwave Studio, these structures were simulated to examine their comparative performance.

Results: The fabricated dielectric-resonator half-wave mirror was shown to be capable of converting linearly polarised terahertz waves into its orthogonal polarised counterpart as well as preserving the handedness of circularly polarised waves upon reflection, in contrast to common mirrors. This structure is highly efficient, with a measured averaged conversion efficiency of 96% covering a relative bandwidth of

53% for a frequency range of 0.89 to 1.54 THz. Through simulation, metallic- and dielectric-resonator metasurfaces exhibit similar performance as half-wave mirrors. The operational bandwidth for metallic-resonator half-wave mirrors is 71% (0.91 THz – 1.91 THz) while the operational bandwidth for dielectric-resonators is 67% (0.89 THz – 1.87 THz) for a polarisation conversion ratio greater than 80%. However, dielectric-resonator metasurfaces are more efficient at polarisation conversion with a PCR of 94% as compared to a PCR of 93% obtained by their metallic-resonator counterpart.

Original contribution: This study constitutes the first demonstration of single layer dielectric-resonator metasurfaces as broadband, highly efficient half-wave mirrors at terahertz frequencies. The broadband capability of this metasurface is attributed to a combination of multiple magnetic dipole resonances arising from the resonator geometry. Furthermore, we confirm through simulations that dielectric resonators provide slightly better efficiencies as compared to their metallic counterparts. This study further confirms that metasurfaces are suitable alternatives for conventional bulk optics to create designable birefringence with high efficiencies and broadband capabilities.

7.4 Outlook

The works in this thesis provides a stepping stone towards technological advancements in the field for polarisation control of terahertz waves. In order to hasten widespread integration into practical applications, a few areas of research needs to be looked into. These research areas include reconfigurability, efficiency and bandwidth of metasurfaces. Terahertz devices for a myriad of applications would benefit greatly with development in these areas.

Reconfigurability: Metasurfaces that are reconfigurable will be highly sought after for practical applications in the terahertz region. The metasurfaces presented in this thesis are static, and thus do not have tunable phase or amplitude distributions. The capability to dynamically change the phase of metasurfaces would allow for on-the-fly switching of output electromagnetic waves. Furthermore, polarisation reconfigurability is important to reduce polarisation mismatch in several applications. There are several methods of achieving reconfigurability in metasurfaces.

For example, the sheet conductivity of graphene is tunable via bias voltages. Thus, metasurfaces with graphene based unit cells have been sought after for their phase modulation properties (Liu *et al.*, 2016; Zhang *et al.*, 2015, 2017). Other materials that has been shown to provide tunability in terahertz metasurfaces aside from graphene are liquid crystals (Chikhi *et al.*, 2016; Wang *et al.*, 2017) and vanadium dioxide (Hashemi *et al.*, 2016; Urade *et al.*, 2016). The properties of these aforementioned materials can be tuned electrically, which allows for a varying phase response of each unit cell. It is worth mentioning that metallic resonators are more suitable for electrical reconfigurability than their dielectric counterparts. Dielectric material have minimal free carriers to provide the dynamic phase change required for tunability. Some alternatives that are investigated include semiconductors (Mitrofanov *et al.*, 2018; Sharma *et al.*, 2012; Emani *et al.*, 2017; Al-Naib *et al.*, 2013) with hopes to provide some dynamic tuning in dielectrics. With a varied phase response, the output beam can be reshaped as required. Nevertheless, these efforts do not provide highly efficient solutions. Therefore, we must search for new designs of metasurfaces with suitable materials that can accommodate electrical-reconfigurability while maintaining high efficiencies at terahertz frequencies.

Conversion efficiency: Dielectric-resonator metasurfaces have been shown to support overlapping electric and magnetic dipole resonances in transmission at optical frequencies (Decker *et al.*, 2015) and in reflection at terahertz frequencies (Ma *et al.*, 2016). With this overlap of resonances, a perfect Huygens' surface can be realised, hence a near-unity either transmission or reflection amplitude can be achieved. Apart from that, a 2π phase coverage is attainable from this overlapping of resonances at a discrete frequency. However, this concept is applicable for radially symmetric designs. Dielectric-resonators as birefringent elements are typically larger in one dimension than the other, in order to provide the required response. With a difference in length and width, dielectric resonators are susceptible to undesirable effects due to coupling issues in array configuration. Typically for polarisation converting metasurfaces, multilayer structures have been proposed to increase polarisation conversion efficiency (Luo *et al.*, 2014). Moreover, both electric and magnetic resonances have to be excited within the multilayer metasurface to minimise unwanted reflection. Thus, polarisation conversion efficiency and power efficiency can be increased with multiple layers.

Bandwidth: As the main aim of this doctoral thesis is to design metasurfaces with enhanced bandwidth and efficiency with designable birefringence, any effort to further increase the bandwidth is always necessary. Birefringence of electromagnetic waves provides the platform for multiple channels through polarisation-division multiplexing which in turn, increases the data rate of applications in terahertz communications. One method to improve bandwidth is to utilise near-field coupling of a secondary metasurface (Gao *et al.*, 2017). With the addition of this secondary metasurface, the number of resonances within the structure increases, which results in a larger overall bandwidth. Though this method enhances the overall bandwidth, it also increases the overall thickness of the metasurface. In a nutshell, the most evident method to enhance bandwidth in metasurfaces is to move towards multilayer designs. Apart from that, as multilayer structures increase fabrication complexity, it would be ideal to look into new methods of fabrication as well.

7.5 Concluding remarks

The work has been successful in achieving its main aim to design and validate metasurfaces as an approach towards creating engineered birefringence at terahertz frequencies. These metasurfaces overcome the limitations set by conventional bulk optics possessing large thickness, narrowband operation and low efficiencies. As demonstrated in the studies in this thesis, the designed metasurfaces are planar, have broadband capabilities and high efficiencies. With these demonstrated designs, integration into various terahertz systems can be accelerated. A myriad of applications in terahertz sensing, imaging and communications would benefit from the realisation of such high-efficiency devices. These advancements in technology would then support development in areas such as public health, security and defence.

Appendix A

Gaussian beam profile irregularities

The THz-TDS system utilises a Gaussian beam excitation, where the collimated beam profile is less than ideal. Figure A.1 shows the raster-scanned beam profile at different frequencies. From the data presented in this figure, the center portion of the input beam can be approximated by a Gaussian beam of radius 12 mm. From Figure A.1(a)-(g), we can see that the irregularities in the Gaussian beam profile is frequency-dependent. Due to these irregularities, the beam profile introduces asymmetry in the measured results. The alignment is then adjusted to reduce the effect of this asymmetry, to our best efforts.

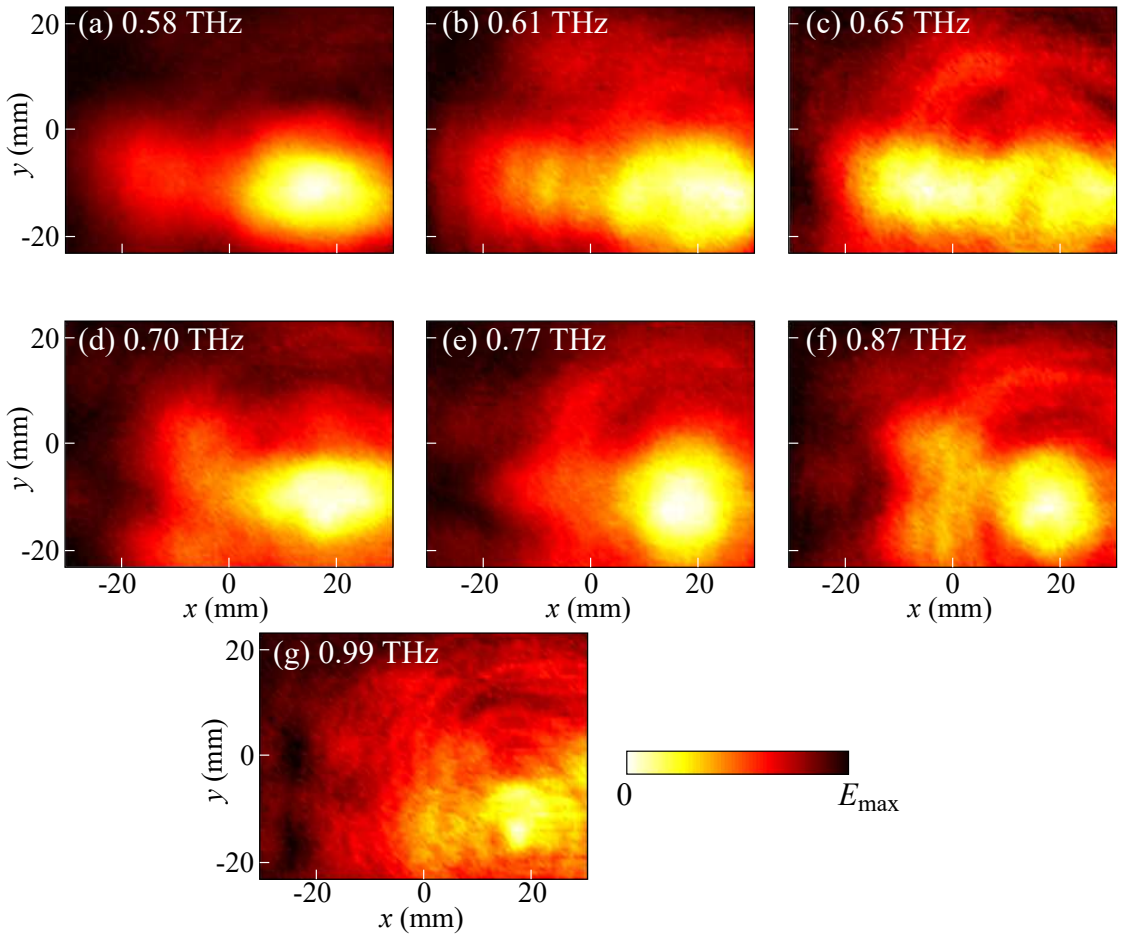

Figure A.1. Magnitude profiles of the Gaussian beam. Magnitude profiles of the collimated beam at corresponding frequencies as shown in (a-g). Adopted from (Headland, 2017)

Bibliography

ADAM-A. J. L. (2011). Review of near-field terahertz measurement methods and their applications, *Journal of Infrared, Millimeter, and Terahertz Waves*, **32**(8), art. no. 976.

AL-NAIB-I., AND WITHAYACHUMNANKUL-W. (2017). Recent progress in terahertz metasurfaces, *Journal of Infrared, Millimeter, and Terahertz Waves*, **38**(9), pp. 1067–1084.

AL-NAIB-I., SHARMA-G., DIGNAM-M. M., HAFEZ-H., IBRAHIM-A., COOKE-D. G., OZAKI-T., AND MORANDOTTI-R. (2013). Effect of local field enhancement on the nonlinear terahertz response of a silicon-based metamaterial, *Physical Review B*, **88**, art. no. 195203.

ARBABI-A., HORIE-Y., BALL-A. J., BAGHERI-M., AND FARAON-A. (2015). Subwavelength-thick lenses with high numerical apertures and large efficiency based on high-contrast transmitarrays, *Nature Communications*, **6**, art. no. 7069.

BALAKRISHNAN-J., FISCHER-B. M., AND ABBOTT-D. (2009). Sensing the hygroscopicity of polymer and copolymer materials using terahertz time-domain spectroscopy, *Applied Optics*, **48**(12), pp. 2262–2266.

BALANIS-C. (1982). *Antenna Theory: Analysis and Design*, Wiley.

BAYRAKTAR-O., CIVI-O. A., AND AKIN-T. (2012). Beam switching reflectarray monolithically integrated with RF MEMS switches, *IEEE Transactions on Antennas and Propagation*, **60**(2), pp. 854–862.

BECKERS-J. M. (1971). Achromatic linear retarders, *Applied Optics*, **10**(4), pp. 973–975.

BERRY-C. W., AND JARRAHI-M. (2012). Broadband terahertz polarizing beam splitter on a polymer substrate, *Journal of Infrared, Millimeter, and Terahertz Waves*, **33**(2), pp. 127–130.

BIRD-T. S., WEILY-A. R., AND HANHAM-S. M. (2008). Antennas for future very-high throughput wireless lans, *IEEE Antennas and Propagation Society International Symposium*, pp. 1–4.

BITZER-A., AND WALTHER-M. (2008). Terahertz near-field imaging of metallic subwavelength holes and hole arrays, *Applied Physics Letters*, **92**(23), art. no. 231101.

BITZER-A., MERBOLD-H., THOMAN-A., FEURER-T., HELM-H., AND WALTHER-M. (2009). Terahertz near-field imaging of electric and magnetic resonances of a planar metamaterial, *Optics Express*, **17**(5), pp. 3826–3834.

BITZER-A., ORTNER-A., AND WALTHER-M. (2010). Terahertz near-field microscopy with subwavelength spatial resolution based on photoconductive antennas, *Applied Optics*, **49**(19), pp. E1–E6.

BITZER-A., ORTNER-A., MERBOLD-H., FEURER-T., AND WALTHER-M. (2011). Terahertz near-field microscopy of complementary planar metamaterials: Babinet's principle, *Optics Express*, **19**(3), pp. 2537–2545.

BLANCHARD-F., DOI-A., TANAKA-T., HIRORI-H., TANAKA-H., KADOYA-Y., AND TANAKA-K. (2011). Real-time terahertz near-field microscope, *Optics Express*, **19**(9), pp. 8277–8284.

BORN-M., AND WOLF-E. (2013). *Principles of Optics: Electromagnetic Theory of Propagation, Interference and Diffraction of Light*, Elsevier.

BOULBRY-B., BOUSQUET-B., JEUNE-B. L., GUERN-Y., AND LOTRIAN-J. (2001). Polarization errors associated with zero-order achromatic quarter-wave plates in the whole visible spectral range, *Optics Express*, **9**(5), pp. 225–235.

BRUNNER-F. D. J., KWON-O.-P., KWON-S.-J., JAZBINŠEK-M., SCHNEIDER-A., AND GÜNTER-P. (2008). A hydrogen-bonded organic nonlinear optical crystal for high-efficiency terahertz generation and detection, *Optics Express*, **16**(21), pp. 16496–16508.

CARRASCO-E., AND PERRUISSEAU-CARRIER-J. (2013). Reflectarray antenna at terahertz using graphene, *IEEE Antennas and Wireless Propagation Letters*, **12**, pp. 253–256.

CHANG-C.-C., HEADLAND-D., ABBOTT-D., WITHAYACHUMNANKUL-W., AND CHEN-H.-T. (2017). Demonstration of a highly efficient terahertz flat lens employing tri-layer metasurfaces, *Optics Letters*, **42**(9), pp. 1867–1870.

CHENG-Y. Z., WITHAYACHUMNANKUL-W., UPADHYAY-A., HEADLAND-D., NIE-Y., GONG-R. Z., BHASKARAN-M., SRIRAM-S., AND ABBOTT-D. (2014). Ultrabroadband reflective polarization convertor for terahertz waves, *Applied Physics Letters*, **105**(18), art. no. 181111.

CHENG-Y. Z., WITHAYACHUMNANKUL-W., UPADHYAY-A., HEADLAND-D., NIE-Y., GONG-R. Z., BHASKARAN-M., SRIRAM-S., AND ABBOTT-D. (2015). Ultrabroadband plasmonic absorber for terahertz waves, *Advanced Optical Materials*, **3**(3), pp. 376–380.

CHEN-T., LI-S., AND SUN-H. (2012). Metamaterials application in sensing, *Sensors*, **12**(3), pp. 2742–2765.

CHEN-Z., GONG-Y., DONG-H., NOTAKE-T., AND MINAMIDE-H. (2013). Terahertz achromatic quarter wave plate: Design, fabrication, and characterization, *Optics Communications*, **311**, pp. 1–5.

CHIKHI-N., LISITSKIY-M., PAPARI-G., TKACHENKO-V., AND ANDREONE-A. (2016). A hybrid tunable thz metadevice using a high birefringence liquid crystal, *Scientific Reports*, **6**, art. no. 34536.

CHONG-K. E., STAUDE-I., JAMES-A., DOMINGUEZ-J., LIU-S., CAMPIONE-S., SUBRAMANIA-G. S., LUK-T. S., DECKER-M., NESHEV-D. N., BRENER-I., AND KIVSHAR-Y. S. (2015). Polarization-independent silicon metadevices for efficient optical wavefront control, *Nano Letters*, **15**(8), pp. 5369–5374.

CHONG-K. E., WANG-L., STAUDE-I., JAMES-A. R., DOMINGUEZ-J., LIU-S., SUBRAMANIA-G. S., DECKER-M., NESHEV-D. N., BRENER-I., AND KIVSHAR-Y. S. (2016). Efficient polarization-insensitive complex wavefront control using huygens metasurfaces based on dielectric resonant meta-atoms, *ACS Photonics*, **3**(4), pp. 514–519.

CONG-L., CAO-W., ZHANG-X., TIAN-Z., GU-J., SINGH-R., HAN-J., AND ZHANG-W. (2013). A perfect metamaterial polarization rotator, *Applied Physics Letters*, **103**(17), art. no. 171107.

CONG-L., XU-N., GU-J., SINGH-R., HAN-J., AND ZHANG-W. (2014). Highly flexible broadband terahertz metamaterial quarter-wave plate, *Laser & Photonics Reviews*, **8**(4), pp. 626–632.

DAI-J., ZHANG-J., ZHANG-W., AND GRISCHKOWSKY-D. (2004). Terahertz time-domain spectroscopy characterization of the far-infrared absorption and index of refraction of high-resistivity, float-zone silicon, *Journal of the Optical Society of America B*, **21**(7), pp. 1379–1386.

DEBUS-C., AND BOLIVAR-P. H. (2007). Frequency selective surfaces for high sensitivity terahertz sensing, *Applied Physics Letters*, **91**(18), art. no. 184102.

DECKER-M., STAUDE-I., FALKNER-M., DOMINGUEZ-J., NESHEV-D. N., BRENER-I., PERTSCH-T., AND KIVSHAR-Y. S. (2015). High-efficiency dielectric huygens surfaces, *Advanced Optical Materials*, **3**(6), pp. 813–820.

DESIATOV-B., MAZURSKI-N., FAINMAN-Y., AND LEVY-U. (2015). Polarization selective beam shaping using nanoscale dielectric metasurfaces, *Optics Express*, **23**(17), pp. 22611–22618.

DESTRIAU-G., AND PROUTEAU-J. (1949). Realisation dum quart donde quasi acromatique par juxtaposition de deux lames cristallines de meme nature, *Journal de Physique et le Radium*, **10**(2), pp. 53–55.

DREYHAUPT-A., WINNERL-S., DEKORSY-T., AND HELM-M. (2005). High-intensity terahertz radiation from a microstructured large-area photoconductor, *Applied Physics Letters*, **86**(12), art. no. 121114.

EBRAHIMI-A., NIRANTAR-S., WITHAYACHUMNANKUL-W., BHASKARAN-M., SRIRAM-S., AL-SARAWI-S. F., AND ABBOTT-D. (2015). Second-order terahertz bandpass frequency selective surface with miniaturized elements, *IEEE Transactions on Terahertz Science and Technology*, **5**(5), pp. 761–769.

EMANI-N. K., KHAIDAROV-E., PANIAGUA-DOMNGUEZ-R., FU-Y. H., VALUCKAS-V., LU-S., ZHANG-X., TAN-S. T., DEMIR-H. V., AND KUZNETSOV-A. I. (2017). High-efficiency and low-loss gallium nitride dielectric metasurfaces for nanophotonics at visible wavelengths, *Applied Physics Letters*, **111**(22), art. no. 221101.

FAN-S., SUH-W., AND JOANNOPOULOS-J. D. (2003). Temporal coupled-mode theory for the fano resonance in optical resonators, *Journal of the Optical Society of America A*, **20**(3), pp. 569–572.

FERGUSON-B., AND ZHANG-X.-C. (2002). Materials for terahertz science and technology, *Nature Materials*, **1**(1), pp. 26–33.

FISCHER-B., HOFFMANN-M., HELM-H., MODJESCH-G., AND JEPSEN-P. U. (2005a). Chemical recognition in terahertz time-domain spectroscopy and imaging, *Semiconductor Science and Technology*, **20**(7), art. no. S246.

FISCHER-B. M., HOFFMANN-M., HELM-H., WILK-R., RUTZ-F., KLEINE-OSTMANN-T., KOCH-M., AND JEPSEN-P. U. (2005b). Terahertz time-domain spectroscopy and imaging of artificial RNA, *Optics Express*, **13**(14), pp. 5205–5215.

GAO-X., SINGH-L., YANG-W., ZHENG-J., LI-H., AND ZHANG-W. (2017). Bandwidth broadening of a linear polarization converter by near-field metasurface coupling, *Scientific Reports*, **7**(1), art. no. 6817.

GEORGE-D., AND MARKELZ-A. (2012). *Terahertz Spectroscopy of Liquids and Biomolecules*, Springer.

GRADY-N. K., HEYES-J. E., CHOWDHURY-D. R., ZENG-Y., REITEN-M. T., AZAD-A. K., TAYLOR-A. J., DALVIT-D. A. R., AND CHEN-H.-T. (2013). Terahertz metamaterials for linear polarization conversion and anomalous refraction, *Science*, **340**(6138), pp. 1304–1307.

GRISCHKOWSKY-D., KEIDING-S., VAN EXTER-M., AND FATTINGER-C. (1990). Far-infrared time-domain spectroscopy with terahertz beams of dielectrics and semiconductors, *Journal of the Optical Society of America B*, **7**(10), pp. 2006–2015.

GUTRUF-P., ZOU-C., WITHAYACHUMNANKUL-W., BHASKARAN-M., SRIRAM-S., AND FUMEAUX-C. (2016). Mechanically tunable dielectric resonator metasurfaces at visible frequencies, *ACS Nano*, **10**(1), pp. 133–141.

HAN-Z., OHNO-S., TOKIZANE-Y., NAWATA-K., NOTAKE-T., TAKIDA-Y., AND MINAMIDE-H. (2017). Thin terahertz-wave phase shifter by flexible film metamaterial with high transmission, *Optics Express*, **25**(25), pp. 31186–31196.

HAO-J., YUAN-Y., RAN-L., JIANG-T., KONG-J. A., CHAN-C. T., AND ZHOU-L. (2007). Manipulating electromagnetic wave polarizations by anisotropic metamaterials, *Physical Review Letters*, **99**, art. no. 063908.

HARIHARAN-P. (1996). Achromatic and apochromatic halfwave and quarterwave retarders, *Optical Engineering*, **35**, art. no. 35.

HASHEMI-M. R. M., YANG-S.-H., WANG-T., SEPÚLVEDA-N., AND JARRAHI-M. (2016). Electronically-controlled beam-steering through vanadium dioxide metasurfaces, *Scientific Reports*, **6**, art. no. 35439.

HAUS-H. A. (1984). *Waves and Fields in Optoelectronics*, Prentice-Hall.

HEADLAND-D. (2017). *Efficient Terahertz-Range Beam Control Using Flat Optics*, PhD thesis, University of Adelaide.

HEADLAND-D., CARRASCO-E., NIRANTAR-S., WITHAYACHUMNANKUL-W., GUTRUF-P., SCHWARZ-J., ABBOTT-D., BHASKARAN-M., SRIRAM-S., PERRUISSEAU-CARRIER-J., AND FUMEAUX-C. (2016). Dielectric resonator reflectarray as high-efficiency nonuniform terahertz metasurface, *ACS Photonics*, **3**(6), pp. 1019–1026.

HEADLAND-D., NIRANTAR-S., WITHAYACHUMNANKUL-W., GUTRUF-P., ABBOTT-D., BHASKARAN-M., FUMEAUX-C., AND SRIRAM-S. (2015a). Terahertz magnetic mirror realized with dielectric resonator antennas, *Advanced Materials*, **27**(44), pp. 7137–7144.

HEADLAND-D., NIU-T., CARRASCO-E., ABBOTT-D., SRIRAM-S., BHASKARAN-M., FUMEAUX-C., AND WITHAYACHUMNANKUL-W. (2017). Terahertz reflectarrays and nonuniform metasurfaces, *IEEE Journal of Selected Topics in Quantum Electronics*, **23**(4), pp. 1–18.

HEADLAND-D., THURGOOD-P., STAVREVSKI-D., WITHAYACHUMNANKUL-W., ABBOTT-D., BHASKARAN-M., AND SRIRAM-S. (2015b). Doped polymer for low-loss dielectric material in the terahertz range, *Optical Materials Express*, **5**(6), pp. 1373–1380.

HEYES-J. E., WITHAYACHUMNANKUL-W., GRADY-N. K., CHOWDHURY-D. R., AZAD-A. K., AND CHEN-H.-T. (2014). Hybrid metasurface for ultra-broadband terahertz modulation, *Applied Physics Letters*, **105**(18), art. no. 181108.

HSIEH-C.-F., PAN-R.-P., TANG-T.-T., CHEN-H.-L., AND PAN-C.-L. (2006). Voltage-controlled liquid-crystal terahertz phase shifter and quarter-wave plate, *Optics Letters*, **31**(8), pp. 1112–1114.

HUANG-J., AND ENCINAR-J. A. (2008). *Reflectarray Antennas*, John Wiley and Sons.

HUANG-J., AND POGORZELSKI-R. J. (1998). A ka-band microstrip reflectarray with elements having variable rotation angles, *IEEE Transactions on Antennas and Propagation*, **46**(5), pp. 650–656.

HU-D., MORENO-G., WANG-X., HE-J., CHAHADIH-A., XIE-Z., WANG-B., AKALIN-T., AND ZHANG-Y. (2014). Dispersion characteristic of ultrathin terahertz planar lenses based on metasurface, *Optics Communications*, **322**, pp. 164 – 168.

HU-D., WANG-X., FENG-S., YE-J., SUN-W., KAN-Q., KLAR-P. J., AND ZHANG-Y. (2013). Ultrathin terahertz planar elements, *Advanced Optical Materials*, **1**(2), pp. 186–191.

HU-W., CAHILL-R., ENCINAR-J. A., DICKIE-R., GAMBLE-H., FUSCO-V., AND GRANT-N. (2008). Design and measurement of reconfigurable millimeter wave reflectarray cells with nematic liquid crystal, *IEEE Transactions on Antennas and Propagation*, **56**(10), pp. 3112–3117.

IMHOF-C., AND ZENGERLE-R. (2007). Strong birefringence in left-handed metallic metamaterials, *Optics Communications*, **280**(1), pp. 213–216.

JACOB-M., PRIEBE-S., KURNER-T., JASTROW-C., KLEINE-OSTMANN-T., AND SCHRADER-T. (2009). An overview of ongoing activities in the field of channel modeling, spectrum allocation and standardization for mm-wave and THz indoor communications, *IEEE Globecom Workshops*, pp. 1–6.

KANDA-N., KONISHI-K., NEMOTO-N., MIDORIKAWA-K., AND KUWATA-GONOKAMI-M. (2017). Real-time broadband terahertz spectroscopic imaging by using a high-sensitivity terahertz camera, *Scientific Reports*, **7**, art. no. 42540.

KANG-G., TAN-Q., WANG-X., AND JIN-G. (2010). Achromatic phase retarder applied to MWIR & LWIR dual-band, *Optics Express*, **18**(2), pp. 1695–1703.

KHORASANINEJAD-M., AMBROSIO-A., KANHAIYA-P., AND CAPASSO-F. (2016). Broadband and chiral binary dielectric meta-holograms, *Science Advances*, **2**, art. no. 5.

KHORASANINEJAD-M., AND CROZIER-K. B. (2014). Silicon nanofin grating as a miniature chirality-distinguishing beam-splitter, *Nature Communications*, **5**, art. no. 5386.

KHORASANINEJAD-M., CHEN-W. T., ZHU-A. Y., OH-J., DEVLIN-R. C., ROQUES-CARMES-C., MISHRA-I., AND CAPASSO-F. (2017). Visible wavelength planar metalenses based on titanium dioxide, *IEEE Journal of Selected Topics in Quantum Electronics*, **23**(3), pp. 1–16.

KHORASANINEJAD-M., ZHU-W., AND CROZIER-K. B. (2015). Efficient polarization beam splitter pixels based on a dielectric metasurface, *Optica*, **2**(4), pp. 376–382.

KHURGIN-J. B. (2015). How to deal with the loss in plasmonics and metamaterials, *Nature*, **10**(1), pp. 2–6.

KLEINE-OSTMANN-T., AND NAGATSUMA-T. (2011). A review on terahertz communications research, *Journal of Infrared, Millimeter, and Terahertz Waves*, **32**(2), pp. 143–171.

KNAB-J. R., ADAM-A. J. L., NAGEL-M., SHANER-E., SEO-M. A., KIM-D. S., AND PLANKEN-P. C. M. (2009). Terahertz near-field vectorial imaging of subwavelength apertures and aperture arrays, *Optics Express*, **17**(17), pp. 15072–15086.

KOENIG-S., LOPEZ-DIAZ-D., ANTES-J., BOES-F., HENNEBERGER-R., LEUTHER-A., TESSMANN-A., SCHMOGROW-R., HILLERKUSS-D., PALMER-R., ZWICK-T., KOOS-C., FREUDE-W., AMBACHER-O., LEUTHOLD-J., AND KALLFASS-I. (2013). Wireless sub-THz communication system with high data rate, *Nature Photonics*, **7**, art. no. 977.

LEE-W. S. L., BHASKARAN-M., SRIRAM-S., FUMEAUX-C., AND WITHAYACHUMNANKUL-W. (2018a). Metallic and dielectric resonators in broadband half-wave mirrors for terahertz frequencies, *3rd Australian Microwave Symposium (AMS)*.

LEE-W. S. L., KALTENECKER-K., NIRANTAR-S., WITHAYACHUMNANKUL-W., WALTHER-M., BHASKARAN-M., FISCHER-B. M., SRIRAM-S., AND FUMEAUX-C. (2017). Terahertz near-field imaging of dielectric resonators, *Optics Express*, **25**(4), pp. 3756–3764.

LEE-W. S. L., NIRANTAR-S., HEADLAND-D., BHASKARAN-M., SRIRAM-S., FUMEAUX-C., AND WITHAYACHUMNANKUL-W. (2018b). Broadband terahertz circular-polarization beam splitter, *Advanced Optical Materials*, **6**(3), art. no. 1870010.

LEVY-U., KIM-H.-C., TSAI-C.-H., AND FAINMAN-Y. (2005). Near-infrared demonstration of computer-generated holograms implemented by using subwavelength gratings with space-variant orientation, *Optics Letters*, **30**(16), pp. 2089–2091.

LI-J.-S., GANG XU-D., AND QUAN YAO-J. (2010). Compact terahertz wave polarizing beam splitter, *Applied Optics*, **49**(24), pp. 4494–4497.

LI-Q.-T., DONG-F., WANG-B., GAN-F., CHEN-J., SONG-Z., XU-L., CHU-W., XIAO-Y.-F., GONG-Q., AND LI-Y. (2016). Polarization-independent and high-efficiency dielectric metasurfaces for visible light, *Optics Express*, **24**(15), pp. 16309–16319.

LIU-L., ZARATE-Y., HATTORI-H. T., NESHEV-D. N., SHADRIVOV-I. V., AND POWELL-D. A. (2016). Terahertz focusing of multiple wavelengths by graphene metasurfaces, *Applied Physics Letters*, **108**(3), art. no. 031106.

LIU-S., SINCLAIR-M. B., MAHONY-T. S., JUN-Y. C., CAMPIONE-S., GINN-J., BENDER-D. A., WENDT-J. R., IHLEFELD-J. F., CLEM-P. G., WRIGHT-J. B., AND BRENER-I. (2014). Optical magnetic mirrors without metals, *Optica*, **1**(4), pp. 250–256.

LOPEZ-A. G., AND CRAIGHEAD-H. G. (1998). Wave-plate polarizing beam splitter based on a form-birefringent multilayer grating, *Optics Letters*, **23**(20), pp. 1627–1629.

LUO-J., YU-H., SONG-M., AND ZHANG-Z. (2014). Highly efficient wavefront manipulation in terahertz based on plasmonic gradient metasurfaces, *Optics Letters*, **39**(8), pp. 2229–2231.

MA-H. F., WANG-G. Z., KONG-G. S., AND CUI-T. J. (2014). Broadband circular and linear polarization conversions realized by thin birefringent reflective metasurfaces, *Optical Materials Express*, **4**(8), pp. 1717–1724.

MASSON-J.-B., AND GALLOT-G. (2006). Terahertz achromatic quarter-wave plate, *Optics Letters*, **31**(2), pp. 265–267.

MA-S., WANG-X., LUO-W., SUN-S., ZHANG-Y., HE-Q., AND ZHOU-L. (2017). Ultra-wide band reflective metamaterial wave plates for terahertz waves, *Europhysics Letters*, **117**(3), art. no. 37007.

MATSUMURA-T., HANANY-S., ADE-P., JOHNSON-B. R., JONES-T. J., JONNALAGADDA-P., AND SAVINI-G. (2009). Performance of three- and five-stack achromatic half-wave plates at millimeter wavelengths, *Applied Optics*, **48**(19), pp. 3614–3625.

MATSUURA-S., TANI-M., AND SAKAI-K. (1997). Generation of coherent terahertz radiation by photomixing in dipole photoconductive antennas, *Applied Physics Letters*, **70**(5), pp. 559–561.

MA-Z., HANHAM-S. M., ALBELLA-P., NG-B., LU-H. T., GONG-Y., MAIER-S. A., AND HONG-M. (2016). Terahertz all-dielectric magnetic mirror metasurfaces, *ACS Photonics*, **3**(6), pp. 1010–1018.

MENDIS-R., NAGAI-M., ZHANG-W., AND MITTLEMAN-D. M. (2017). Artificial dielectric polarizing-beamsplitter and isolator for the terahertz region, *Scientific Reports*, **7**(1), art. no. 5909.

MITROFANOV-O., DOMINEC-F., KUŽEL-P., RENO-J. L., BRENER-I., CHUNG-U.-C., ELISSALDE-C., MAGLIONE-M., AND MOUNAIX-P. (2014). Near-field probing of mie resonances in single tio2 microspheres at terahertz frequencies, *Optics Express*, **22**(19), pp. 23034–23042.

MITROFANOV-O., SIDAY-T., THOMPSON-R. J., LUK-T. S., BRENER-I., AND RENO-J. L. (2018). Efficient photoconductive terahertz detector with all-dielectric optical metasurface, *APL Photonics*, **3**(5), art. no. 051703.

MORIWAKI-A., OKANO-M., AND WATANABE-S. (2017). Internal triaxial strain imaging of visibly opaque black rubbers with terahertz polarization spectroscopy, *APL Photonics*, **2**(10), art. no. 106101.

MO-W., WEI-X., WANG-K., LI-Y., AND LIU-J. (2016). Ultrathin flexible terahertz polarization converter based on metasurfaces, *Optics Express*, **24**(12), pp. 13621–13627.

NAFTALY-M., AND MILES-R. E. (2007). Terahertz time-domain spectroscopy for material characterization, *Proceedings of the IEEE*, **95**(8), pp. 1658–1665.

NAGATSUMA-T., HORIGUCHI-S., MINAMIKATA-Y., YOSHIMIZU-Y., HISATAKE-S., KUWANO-S., YOSHIMOTO-N., TERADA-J., AND TAKAHASHI-H. (2013). Terahertz wireless communications based on photonics technologies, *Optics Express*, **21**(20), pp. 23736–23747.

NAKATA-Y., TAIRA-Y., NAKANISHI-T., AND MIYAMARU-F. (2017). Freestanding transparent terahertz half-wave plate using subwavelength cut-wire pairs, *Optics Express*, **25**(3), pp. 2107–2114.

NAYERI-P., LIANG-M., SABORY-GARCA-R. A., TUO-M., YANG-F., GEHM-M., XIN-H., AND ELSHERBENI-A. Z. (2014). 3D printed dielectric reflectarrays: Low-cost high-gain antennas at sub-millimeter waves, *IEEE Transactions on Antennas and Propagation*, **62**(4), pp. 2000–2008.

NIELSEN-K., RASMUSSEN-H. K., ADAM-A. J. L., PLANKEN-P. C. M., BANG-O., AND JEPSEN-P. U. (2009). Bendable, low-loss topas fibers for the terahertz frequency range, *Optics Express*, **17**(10), pp. 8592–8601.

NIU-T., UPADHYAY-A., WITHAYACHUMNANKUL-W., HEADLAND-D., ABBOTT-D., BHASKARAN-M., SRIRAM-S., AND FUMEAUX-C. (2015). Polarization-dependent

thin-film wire-grid reflectarray for terahertz waves, *Applied Physics Letters*, **107**(3), art. no. 031111.

NIU-T., WITHAYACHUMNANKUL-W., UNG-B. S.-Y., MENEKSE-H., BHASKARAN-M., SRIRAM-S., AND FUMEAUX-C. (2013). Experimental demonstration of reflectarray antennas at terahertz frequencies, *Optics Express*, **21**(3), pp. 2875–2889.

NIU-T., WITHAYACHUMNANKUL-W., UPADHYAY-A., GUTRUF-P., ABBOTT-D., BHASKARAN-M., SRIRAM-S., AND FUMEAUX-C. (2014). Terahertz reflectarray as a polarizing beam splitter, *Optics Express*, **22**(13), pp. 16148–16160.

NORDIN-G. P., AND DEGUZMAN-P. C. (1999). Broadband form birefringent quarter-wave plate for the mid-infrared wavelength region, *Optics Express*, **5**(8), pp. 163–168.

NOUMAN-M. T., HWANG-J. H., AND JANG-J.-H. (2016). Ultrathin terahertz quarter-wave plate based on split ring resonator and wire grating hybrid metasurface, *Scientific Reports*, **6**, art. no. 39062.

PAUL-O., REINHARD-B., KROLLA-B., BEIGANG-R., AND RAHM-M. (2010). Gradient index metamaterial based on slot elements, *Applied Physics Letters*, **96**(24), art. no. 241110.

PEIPONEN-K.-E., ZEITLER-A., AND KUWATA-GONOKAMI-M. (2012). *Terahertz Spectroscopy and Imaging*, Vol. 171, Springer.

PERALTA-X. G., SMIRNOVA-E. I., AZAD-A. K., CHEN-H.-T., TAYLOR-A. J., BRENER-I., AND O'HARA-J. F. (2009). Metamaterials for THz polarimetric devices, *Optics Express*, **17**(2), pp. 773–783.

PETOSA-A. (2007). *Dielectric Resonator Antenna Handbook*, Artech House Publishers.

PEYTAVIT-E., DONCHE-C., LEPILLIET-S., DUCOURNAU-G., AND LAMPIN-J. F. (2011). Thin-film transmission lines using cyclic olefin copolymer for millimetre-wave and terahertz integrated circuits, *Electronic Letters*, **47**(7), pp. 453–454.

PFEIFFER-C., AND GRBIC-A. (2013). Cascaded metasurfaces for complete phase and polarization control, *Applied Physics Letters*, **102**(23), art. no. 231116.

PFEIFFER-C., EMANI-N. K., SHALTOUT-A. M., BOLTASSEVA-A., SHALAEV-V. M., AND GRBIC-A. (2014). Efficient light bending with isotropic metamaterial huygens surfaces, *Nano Letters*, **14**(5), pp. 2491–2497.

PLUM-E., AND ZHELUDEV-N. I. (2015). Chiral mirrors, *Applied Physics Letters*, **106**(22), art. no. 221901.

PORS-A., AND BOZHEVOLNYI-S. I. (2013). Plasmonic metasurfaces for efficient phase control in reflection, *Optics Express*, **21**(22), pp. 27438–27451.

POZAR-D. M., TARGONSKI-S. D., AND SYRIGOS-H. D. (1997). Design of millimeter wave microstrip reflectarrays, *IEEE Transactions on Antennas and Propagation*, **45**(2), pp. 287–296.

QU-C., MA-S., HAO-J., QIU-M., LI-X., XIAO-S., MIAO-Z., DAI-N., HE-Q., SUN-S., AND ZHOU-L. (2015). Tailor the functionalities of metasurfaces based on a complete phase diagram, *Physical Reviews Letters*, **115**, art. no. 235503.

REID-C. B., REESE-G., GIBSON-A. P., AND WALLACE-V. P. (2013). Terahertz time-domain spectroscopy of human blood, *IEEE Journal of Biomedical and Health Informatics*, **17**(4), pp. 774–778.

REID-M., AND FEDOSEJEVS-R. (2006). Terahertz birefringence and attenuation properties of wood and paper, *Applied Optics*, **45**(12), pp. 2766–2772.

RYAN-C. G., CHAHARMIR-M. R., SHAKER-J., BRAY-J. R., ANTAR-Y. M., AND ITTIPIBOON-A. (2010). A wideband transmitarray using dual-resonant double square rings, *IEEE Transactions on Antennas and Propagation*, **58**(5), pp. 1486–1493.

SAHA-A., BHATTACHARYA-K., AND CHAKRABORTY-A. K. (2012). Achromatic quarter-wave plate using crystalline quartz, *Applied Optics*, **51**(12), pp. 1976–1980.

SAUTTER-J., STAUDE-I., DECKER-M., RUSAK-E., NESHEV-D. N., BRENER-I., AND KIVSHAR-Y. S. (2015). Active tuning of all-dielectric metasurfaces, *ACS Nano*, **9**(4), pp. 4308–4315.

SCHELLER-M., JÖRDENS-C., AND KOCH-M. (2010). Terahertz form birefringence, *Optics Express*, **18**(10), pp. 10137–10142.

SCHERGER-B., SCHELLER-M., VIEWEG-N., CUNDIFF-S. T., AND KOCH-M. (2011). Paper terahertz wave plates, *Optics Express*, **19**(25), pp. 24884–24889.

SHALTOUT-A., LIU-J., SHALAEV-V. M., AND KILDISHEV-A. V. (2014). Optically active metasurface with non-chiral plasmonic nanoantennas, *Nano Letters*, **14**(8), pp. 4426–4431.

SHARMA-G., AL-NAIB-I., HAFEZ-H., MORANDOTTI-R., COOKE-D. G., AND OZAKI-T. (2012). Carrier density dependence of the nonlinear absorption of intense THz radiation in gaas, *Optics Express*, **20**(16), pp. 18016–18024.

SINGH-R., CAO-W., AL-NAIB-I., CONG-L., WITHAYACHUMNANKUL-W., AND ZHANG-W. (2014). Ultrasensitive terahertz sensing with high-Q fano resonances in metasurfaces, *Applied Physics Letters*, **105**(17), art. no. 171101.

SONG-Q. W., LEE-M. C., AND TALBOT-P. J. (1992). Polarization sensitivity of birefringent photorefractive holograms and its applications to binary switching, *Applied Optics*, **31**(29), pp. 6240–6246.

STAUDE-I., MIROSHNICHENKO-A. E., DECKER-M., FOFANG-N. T., LIU-S., GONZALES-E., DOMINGUEZ-J., LUK-T. S., NESHEV-D. N., BRENER-I., AND KIVSHAR-Y. (2013). Tailoring directional scattering through magnetic and electric resonances in subwavelength silicon nanodisks, *ACS Nano*, **7**(9), pp. 7824–7832.

STRIKWERDA-A. C., FAN-K., TAO-H., PILON-D. V., ZHANG-X., AND AVERITT-R. D. (2009). Comparison of birefringent electric split-ring resonator and meanderline structures as quarter-wave plates at terahertz frequencies, *Optics Express*, **17**(1), pp. 136–149.

SUH-W., WANG-Z., AND FAN-S. (2004). Temporal coupled-mode theory and the presence of non-orthogonal modes in lossless multimode cavities, *IEEE Journal of Quantum Electronics*, **40**(10), pp. 1511–1518.

SUZUKI-D., ODA-S., AND KAWANO-Y. (2016a). A flexible and wearable terahertz scanner, *Nature Photonics*, **10**, art. no. 809.

SUZUKI-T., NAGAI-M., AND KISHI-Y. (2016b). Extreme-sensitivity terahertz polarizer inspired by an anisotropic cut-through metamaterial, *Optics Letters*, **41**(2), pp. 325–328.

TYAN-R.-C., SUN-P.-C., SCHERER-A., AND FAINMAN-Y. (1996). Polarizing beam splitter based on the anisotropic spectral reflectivity characteristic of form-birefringent multilayer gratings, *Optics Letters*, **21**(10), pp. 761–763.

URADE-Y., NAKATA-Y., OKIMURA-K., NAKANISHI-T., MIYAMARU-F., TAKEDA-M. W., AND KITANO-M. (2016). Dynamically babinet-invertible metasurface: a capacitive-inductive reconfigurable filter for terahertz waves using vanadium-dioxide metal-insulator transition, *Optics Express*, **24**(5), pp. 4405–4410.

VATANSEVER-F., AND HAMBLIN-M. R. (2012). Far infrared radiation (FIR): Its biological effects and medical applications, *Photonics and Lasers in Medicine*, **4**, pp. 255–266.

WALIA-S., SHAH-C. M., GUTRUF-P., NILI-H., CHOWDHURY-D. R., WITHAYACHUMNANKUL-W., BHASKARAN-M., AND SRIRAM-S. (2015). Flexible metasurfaces and metamaterials: A review of materials and fabrication processes at micro- and nano-scales, *Applied Physics Reviews*, **2**(1), art. no. 011303.

WALLAUER-J., BITZER-A., WASELIKOWSKI-S., AND WALTHER-M. (2011). Near-field signature of electromagnetic coupling in metamaterial arrays: a terahertz microscopy study, *Optics Express*, **19**(18), pp. 17283–17292.

WALTHER-M., PLOCHOCKA-P., FISCHER-B., HELM-H., AND UHD JEPSEN-P. (2002). Collective vibrational modes in biological molecules investigated by terahertz time-domain spectroscopy, *Biopolymers*, **67**(4-5), pp. 310–313.

WANG-D., GU-Y., GONG-Y., QIU-C.-W., AND HONG-M. (2015a). An ultrathin terahertz quarter-wave plate using planar babinet-inverted metasurface, *Optics Express*, **23**(9), pp. 11114–11122.

WANG-F., WEI-Q.-H., AND HTOON-H. (2014). Generation of steep phase anisotropy with zero-backscattering by arrays of coupled dielectric nano-resonators, *Applied Physics Letters*, **105**(12), art. no. 121112.

WANG-L., GE-S., HU-W., NAKAJIMA-M., AND LU-Y. (2017). Graphene-assisted high-efficiency liquid crystal tunable terahertz metamaterial absorber, *Optics Express*, **25**(20), pp. 23873–23879.

WANG-Q., ZHANG-X., XU-Y., TIAN-Z., GU-J., YUE-W., ZHANG-S., HAN-J., AND ZHANG-W. (2015b). A broadband metasurface-based terahertz flat-lens array, *Advanced Optical Materials*, **3**(6), pp. 779–785.

WEI-M., XU-Q., WANG-Q., ZHANG-X., LI-Y., GU-J., TIAN-Z., ZHANG-X., HAN-J., AND ZHANG-W. (2017). Broadband non-polarizing terahertz beam splitters with variable split ratio, *Applied Physics Letters*, **111**(7), art. no. 071101.

WEIS-P., PAUL-O., IMHOF-C., BEIGANG-R., AND RAHM-M. (2009). Strongly birefringent metamaterials as negative index terahertz wave plates, *Applied Physics Letters*, **95**(17), art. no. 171104.

WEST-P. R., STEWART-J. L., KILDISHEV-A. V., SHALAEV-V. M., SHKUNOV-V. V., STROHKENDL-F., ZAKHARENKOV-Y. A., DODDS-R. K., AND BYREN-R. (2014). All-dielectric subwavelength metasurface focusing lens, *Optics Express*, **22**(21), pp. 26212–26221.

WILTSE-J. C. (1984). History of millimeter and submillimeter waves, *IEEE Transactions on Microwave Theory and Techniques*, **32**(9), pp. 1118–1127.

WITHAYACHUMNANKUL-W., AND ABBOTT-D. (2009). Metamaterials in the terahertz regime, *IEEE Photonics Journal*, **1**(2), pp. 99–118.

WITHAYACHUMNANKUL-W., FISCHER-B. M., AND ABBOTT-D. (2008). Numerical removal of water vapour effects from terahertz time-domain spectroscopy measurements, *Proceedings of the Royal Society of London A: Mathematical, Physical and Engineering Sciences*, **464**(2097), pp. 2435–2456.

WITHAYACHUMNANKUL-W., LIN-H., SERITA-K., SHAH-C. M., SRIRAM-S., BHASKARAN-M., TONOUCHI-M., FUMEAUX-C., AND ABBOTT-D. (2012). Sub-diffraction thin-film sensing with planar terahertz metamaterials, *Optics Express*, **20**(3), pp. 3345–3352.

WITHAYACHUMNANKUL-W., SHAH-C. M., FUMEAUX-C., UNG-B. S.-Y., PADILLA-W. J., BHASKARAN-M., ABBOTT-D., AND SRIRAM-S. (2014). Plasmonic resonance toward terahertz perfect absorbers, *ACS Photonics*, **1**(7), pp. 625–630.

WOLFF-L. B. (1994). Polarization camera for computer vision with a beam splitter, *Journal of the Optical Society of America A*, **11**(11), pp. 2935–2945.

XIA-R., JING-X., GUI-X., TIAN-Y., AND HONG-Z. (2017). Broadband terahertz half-wave plate based on anisotropic polarization conversion metamaterials, *Optical Materials Express*, **7**(3), pp. 977–988.

YAMADA-I., TAKANO-K., HANGYO-M., SAITO-M., AND WATANABE-W. (2009). Terahertz wire-grid polarizers with micrometer-pitch al gratings, *Optics Letters*, **34**(3), pp. 274–276.

YANG-Q., GU-J., WANG-D., ZHANG-X., TIAN-Z., OUYANG-C., SINGH-R., HAN-J., AND ZHANG-W. (2014). Efficient flat metasurface lens for terahertz imaging, *Optics Express*, **22**(21), pp. 25931–25939.

YUAN-Y., DING-X., ZHANG-K., AND WU-Q. (2017). Planar efficient metasurface for vortex beam generating and converging in microwave region, *IEEE Transactions on Magnetics*, **53**(6), pp. 1–4.

YUE-F., WEN-D., XIN-J., GERARDOT-B. D., LI-J., AND CHEN-X. (2016). Vector vortex beam generation with a single plasmonic metasurface, *ACS Photonics*, **3**(9), pp. 1558–1563.

YU-N., GENEVET-P., KATS-M. A., AIETA-F., TETIENNE-J.-P., CAPASSO-F., AND GABURRO-Z. (2011). Light propagation with phase discontinuities: generalized laws of reflection and refraction, *Science*, **334**(6054), pp. 333–337.

YU-W., MIZUTANI-A., KIKUTA-H., AND KONISHI-T. (2006). Reduced wavelength-dependent quarter-wave plate fabricated by a multilayered subwavelength structure, *Applied Optics*, **45**(12), pp. 2601–2606.

ZHANG-B., AND GONG-Y. (2015). Achromatic terahertz quarter waveplate based on silicon grating, *Optics Express*, **23**(11), pp. 14897–14902.

ZHANG-X., JIN-Y., AND MA-X. F. (1992). Coherent measurement of THz optical rectification from electro-optic crystals, *Applied Physics Letters*, **61**(23), pp. 2764–2766.

ZHANG-X., TIAN-Z., YUE-W., GU-J., ZHANG-S., HAN-J., AND ZHANG-W. (2013). Broadband terahertz wave deflection based on C-shape complex metamaterials with phase discontinuities, *Advanced Materials*, **25**(33), pp. 4567–4572.

ZHANG-Y., FENG-Y., ZHAO-J., JIANG-T., AND ZHU-B. (2017). Terahertz beam switching by electrical control of graphene-enabled tunable metasurface, *Scientific Reports*, **7**(1), art. no. 14147.

ZHANG-Y., FENG-Y., ZHU-B., ZHAO-J., AND JIANG-T. (2015). Switchable quarter-wave plate with graphene based metamaterial for broadband terahertz wave manipulation, *Optics Express*, **23**(21), pp. 27230–27239.

ZHELUDEV-N. I., AND KIVSHAR-Y. S. (2012). From metamaterials to metadevices, *Nature Materials*, **11**(11), pp. 917–924.

ZHU-W., AND NAHATA-A. (2007). Electric field vector characterization of terahertz surface plasmons, *Optics Express*, **15**(9), pp. 5616–5624.

ZI-J., XU-Q., WANG-Q., TIAN-C., LI-Y., ZHANG-X., HAN-J., AND ZHANG-W. (2018). Terahertz polarization converter based on all-dielectric high birefringence metamaterial with elliptical air holes, *Optics Commununications*, **416**, pp. 130 – 136.

ZOU-L., WITHAYACHUMNANKUL-W., SHAH-C. M., MITCHELL-A., BHASKARAN-M., SRIRAM-S., AND FUMEAUX-C. (2013). Dielectric resonator nanoantennas at visible frequencies, *Optics Express*, **21**(1), pp. 1344–1352.

ZOU-L., WITHAYACHUMNANKUL-W., SHAH-C. M., MITCHELL-A., KLEMM-M., BHASKARAN-M., SRIRAM-S., AND FUMEAUX-C. (2014). Efficiency and scalability of dielectric resonator antennas at optical frequencies, *IEEE Photonics Journal*, **6**(4), pp. 1–10.

Biography

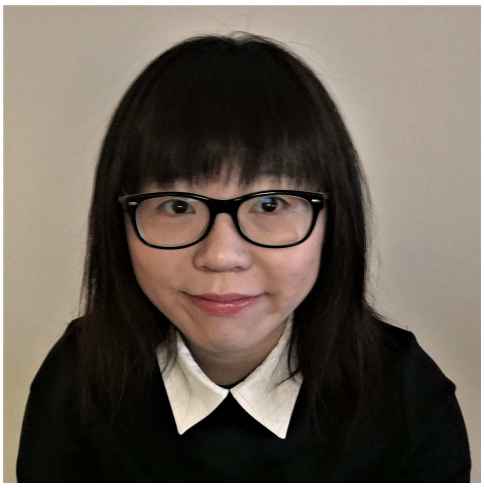

Wendy Suk Ling Lee was born in Melaka, Malaysia in 1990. She received her Bachelor of Engineering in the field of Electrical and Computer Systems Engineering with honours from Monash University in 2014. After obtaining her undergraduate degree, she immediately joined the School of Electrical and Electronic Engineering at the University of Adelaide in the area of applied electromagnetics under the supervision of Prof. Christophe Fumeaux and Dr. Withawat Withayachumnankul.

During her candidature, she received the IEEE SA Section Student Travel Award in 2016 to attend the 41st International Conference on Infrared, Millimeter and Terahertz Waves (IRMMW-THz) in Copenhagen, Denmark and a travel grant provided by an anonymous donor which supported her travels to Freiburg, Germany to conduct experiments with a near-field microscope. She was the recipient of the Student-led Teaching Award 2017 from the University of Adelaide for excellence in teaching and the University of Adelaide Completion Scholarship from 2017-2018. Her research interests revolve around metasurfaces in the terahertz and visible frequency regime.

Wendy S.L. Lee
wendylee14@me.com